ABSTRACT

Title of Dissertation:	THERMOPHYSICAL PROPERTIES OF NANOSTRUCTURED MATERIALS
	Zhi Yang, Doctor of Philosophy, 2018
Dissertation directed by:	Professor Bao Yang, Department of Mechanical Engineering

As electronic devices become smaller in size, thermal management challenge for various applications must be solved for enhanced system performance and reliability. Without appropriate thermal conductivity to dissipate excess heat, the system overall performance and reliability will be compromised. For high power electronic

applications, local heat flux can be on the order of kW/cm^2, highly thermally conductive materials are preferred to effectively dissipate heat generated inside system. On the other hand, materials with low thermal conductivity are desired to prevent thermal short-circuit, for example, in thermoelectric applications. This dissertation investigates thermal properties of nanostructured materials, in which the approach of using additives in the base material to tailor the effective thermal conductivity of composite material. For power systems, Wax-BN composite exhibits in-plane thermal conductivity of 3.14 W/mK, which is 12 time enhancement compared to that of pristine wax. Moreover, an improved 11.3-13.3 MV/m breakdown voltage of Wax-BN composite was achieved. For optoelectronic systems, a thermally conductive, electrically insulating and optically transparent nanopaper using a bilayer design structure with BN and cellulose nanofiber (CNF) was proposed. An optical transparency (70%) and in-plane thermal conductivity (0.76 W/m/K) were successfully achieved with BN-CNF nanopaper. For lithium ion battery energy storage system, BN-coated separator results in Coulombic efficiency stabilizing at 92% over 100 cycles compared to 18% for pristine separator under 0.5 mA/cm^2 current density condition. BN-coated separator reduced lithium dendrite by creating a more homogeneous thermal environment. In extreme high temperature applications, certain substrate for example glass suffers from poor thermal management properties, which greatly limits the system performance. With BN coated thin film glass push the maximum operating temperature to 1000 ºC compared to that of 700 ºC for normal glass, indicating enhanced thermal management capability of substrate. Bi_2Te_3 material properties modification with external magnetic field has also been explored. Inside magnetic field,

cross-plane thermal conductivity of Bi_2Te_3 is predicted to experience 3.3% drop. The TEC numerical simulation indicates Bi_2Te_3 exhibit 1.7 ºC enhancement inside magnetic field. Material thermal conductivity modification has been demonstrated as a promising approach to enhance thermal management capability in electronic systems.

THERMOPHYSICAL PROPERTIES OF NANOSTRUCTURED MATERIALS

By

Zhi Yang

Dissertation submitted to the Faculty of the Graduate School of the

University of Maryland, College Park, in partial fulfillment

of the requirements for the degree of

Doctor of Philosophy

2018

Advisory Committee:

Professor Bao Yang, Chair

Professor Yunho Hwang

Professor Min Ouyang

Professor Miao Yu

Professor Kenneth Yu (Dean's Representative)

Dedication

To my mom and dad for their unconditional love.

Acknowledgement

First of all, I would like to thank my advisor and dissertation chair, Prof. Bao Yang. Dr. Yang's friendly demeanor and endless knowledge convinced me to pursue my doctoral degree at University of Maryland. No matter how busy his schedule, he is always patient to help and give advice. His wisdom and tutelage have truly been wonderful and are much appreciated. I am extremely grateful for the guidance and scientific knowledge that he provided.

Secondly, many thanks to Prof. Yunho Hwang for serving on my dissertation advisory committee and for teaching me so much in the classroom. I would also like to thank Prof. Amir Riaz, Prof. Min Ouyang, Prof. Miao Yu and Prof. Kenneth Yu and for serving on my advisory committee and providing guidance through the final stages of my work.

Last but not least, I am grateful to my friends, colleagues, and lab mates for helping me over the last five years: Dr. Hanbing Lu, Dr. Liangbing Hu, Jiajun Xu, Fangyu Cao, Mike Manno, Mike Fish, Sevket Yuruker, Chang Liu, Qing Yang, Huilong Hou, Jan Muehlbauer, Yong Pei, Beihan Zhao, Rui Xu, Wei Luo, Kun Fu, An Wang, Guang Chen and Qian Jiang.

Thank you to my family for your unconditional love and support: Mom and Dad.

Table of Contents

List of Tables

List of Figures

Nomenclature

Abbreviations	
AAO	Anodic Aluminum Oxide
ABS	Acrylonitrile Butadiene Styrene
AFM	Atomic Force Microscopy
BNNSs	Boron Nitride Nanosheets
CNT	Carbon Nano Tube
CBD	Convective Boiling Domain
DC	Direct Current
DSC	Differential Scanning Calorimetry
PCM	Phase Change Material
PLA	Polylactic Acid
PS	Polystyrene Spheres
NBD	Nucleate Boiling Domain
NFC	Nano Fiber Cellulose
SEM	Scanning Electron Microscopy
TEC	Thermoelectric Cooler
TEM	Transmission Electron Microscopy
Symbols	
A	Total Area (m^2)
B	Magnetic Field Flux (milliGauss)
Bo	Boiling Number

c	Heat Capacity (J/K)
d	Diameter (mm)
E	Energy (J)
f	Friction Factor
F	Force (N)
h	Heat Transfer Coefficient (W/m^2K)
k	Thermal Conductivity (W/mK)
k_B	Boltzman Constant
L	Lorentz Number
l	Mean Free Path (m)
I	Current (A)
r	Radius (m)
m	Mass (kg)
R	Resistance (ohm)
Re	Reynolds Number
Nu	Nusselt Number
Pr	Prandtl Number
S	Seeback Coefficient (V/K)
T	Temperature (°C)
U	Velocity (m/s)
V	Voltage (V)
Q	Heat Transfer Rate (J/s)

Greek Letters	
ΔP	Pressure Drop (Pa)
ΔT	Temperature Difference (ºC or K)
ρ	Density (kg/m^3)
α	Thermal Diffusivity (m^2/s)
ν	Particle Velocity (m/s)
σ	Electrical Conductivity (S/m)
ω	Frequency (Hz)
χ	Quality
μ	Viscosity (Pa·s)
φ	Phase
ϕ	Angle (º)
τ	Relaxation Time (s)
Subscripts	
e	Electrons
g	Gas Molecules
l	Liquid
L	Lattice
o	Outlet
p	Positive
P	Pressure
n	Negative

s	Surface
v	Vapor
x	In x direction
vap	Evaporation

Chapter 1 Introduction

1.1 Motivation and Overview

With the rapid development of technology nowadays, more and more applications are associated with energy transport including kinetic energy, mechanical energy, chemical energy, magnetic energy, nuclear energy, thermal energy and so on. Among various energy transport forms, thermal energy has attracted increasing attention since most of energy conversion process involves either heat release or absorption. During the heat transfer process, the thermal conductivity of a material, in SI unit of W/mK, denotes material ability to conduct heat from high temperature side to low temperature side. Without an appropriate thermal conductivity material, system thermal design can be extremely challenging or the overall performance may be compromised [1].

During the past a few decades, researchers have extensively investigated the underlying thermal transport behavior and proposed many ways to tailor material thermal conductivity for enhanced overall performance. Those advances directly lead to major breakthroughs in multiple applications. In power electronic applications, for example, integrated circuit, Moore's law predicts the number of transistors per square inch will be doubled every two years, which can result in ~kW/cm^2 heat removal necessity from the chip[2]. In such high heat flux applications, the materials with higher thermal conductivity are preferred to effectively dissipate heat generated inside electronic component to maintain safe operating temperature and prolong the device lifetime. On the other side, in some applications, lower thermal conductivities are desired to avoid

component thermal failure. One example is the thermal insulation coating outside the space shuttle. When the space shuttle travels at very high speed through the atmosphere layer, the friction between its surface and gas molecules can produce significant amount of heat as shown in Figure 1-1 (b), which can exceed melting point of most materials. To protect the core components from the overheating issue, the thermal insulation layer is critical. In such thermal insulation material, the thermal conductivity needs to be minimized to prevent heat propagation into the inner structures of space shuttle. Another example is in the thermoelectric cooler (TEC) application, the Peltier effect on one side of the thermoelectric (TE) leg is used to cool the hot spot, while heat is dumped at the other side of TE leg. The parasitic back conduction through the thermoelectric leg needs to be minimized to achieve better cooling performance.

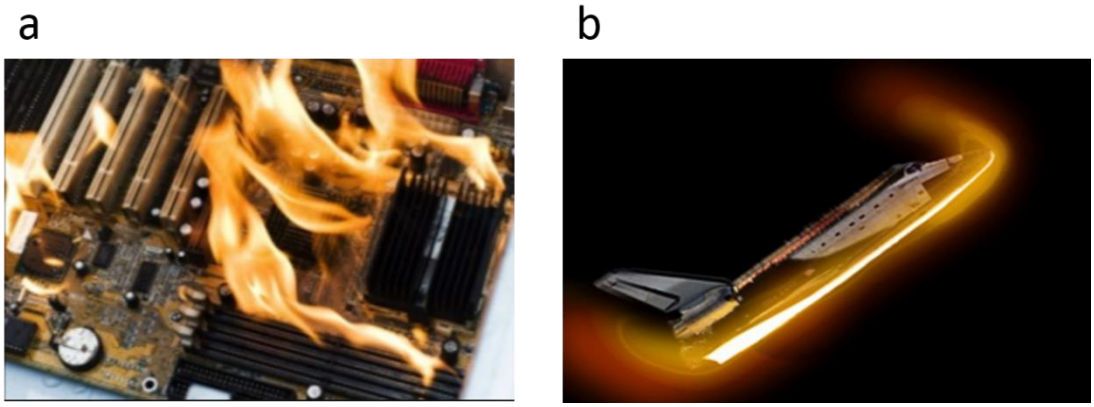

Figure 1-1 (a) Thermal Failure in Power Electronic System [3], (b) Thermal Issues in Space Shuttle at High Speed [4]

Table 1 lists the experimental thermal conductivity values of common materials in a wide range by Chung [5] and Vargaftik [6] at moderate temperatures. Thermal conductivity varies for different substances and depends on multiple factors, such as

structure, environment temperature and pressure *etc*. Usually, the material thermal conductivity values below 0.1 W/mK is considered low and can be used as thermal insulation material, such as foams and fibers. The thermal conductivity in the range of 1-10 W/mK, is considered to be moderate to high values. If the material thermal conductivity is over 100 W/mK, it is reckoned as very conductive material, which is used as thermal conductors for heat dissipation.

Table 1-1 Thermal Conductivity Values of Various Substances at Atmospheric Pressure at Moderate Temperature.

Material	Thermal Conductivity (W/mK)	Material	Thermal Conductivity (W/mK)
Metal		Liquid	
Aluminum	247	Acetone	0.161
Copper	398	Ethanol	0.169
Gold	315	Water	0.607
Lead	30	Toluene	0.134
Nonmetallic		Gas	
Diamond	2000	Helium	0.156
Silicon Carbide	270	Neon	0.048
Aluminum Nitride	320	Argon	0.0178

Not every property of a material is ideal for its applications, sometimes, to satisfy some primary system functional requirements, the material selection is limited to materials with inappropriate thermal properties. In order to modify thermal property of such materials to enhance their thermal performances, several techniques have been proposed over the past a few decades. Those experimental techniques to modify overall effective thermal conductivity of composite can be divided into a few categories: a. addition of special fillers into the base material; b. modification the material manufacture process to alter the intrinsic structure; c. alternation of the external environment to affect the heat transport process inside the material.

Lots of research efforts have been placed on additives into the base materials to form a composite. By incorporating highly thermal conductive fillers, such as metal nanoparticles [7, 8], carbon nanotubes (CNTs) [9, 10] and graphene flakes [11, 12], into the poor thermal conductivity base materials, for example polymers, have been proved to be an effective way to exhibit improved effective overall thermal conductivity of the composite. Another commonly used method is to modify material manufacture process to alter its structure or properties to achieve different thermal conductivity. Han *et al.* experimentally observed that holey graphene experienced in 3 times enhancement in thermal conductivity under different pressures at room temperature [13]. For the third method, different thermal conductivities of certain environmental-responsive specimen can be achieved by changing the external environment. The response of certain materials to external environment change yield different thermal conductivities. Das *et al.* [14] reported by using temperature

oscillation technique to affect Brownian like motion of the nanoparticles to achieve thermal conductivity enhancement of 2 to 4 times over a small temperature range between 21 to 51˚ C with Al_2O_3-water nanofluids. The increased stochastic motion of nanoparticles brings extra nano-effect of conducting behavior of the fluid. Table 2 summarizes the commonly used techniques to tailor thermal conductivity of materials in recent years [15-24].

Table 1-2 Summary of Various Approaches to Tailor Thermal Conductivity of Materials.

Researcher and Year	Classification	Materials	Observation	Note
Lee *et al.* 2005	Additives to base material	AlN/ Polyethylene	K increases from base 0.35 to 2.27 W/mK	75 vol. % loading ratio
Lee *et al.* 2008	Additives to base material	AlN/ Epoxy	K increases 15 times than pure epoxy	57 vol. % filler loading ratio

Yu *et al.* 2008	Additives to base material	Graphite Nanoplatelet/Epoxy	K increases 6 times	10 wt. % filler loading ratio
Li *et al.* 2010	Additives to base material	Boron Nitride/ Polyimide	K increases from 0.2 to 1.2 W/mK	30 wt. % filler loading ratio
Ekimov *et al.* 2008	External Pressure	Diamond/ copper composite	600 W/mK at 2GPa to 900 W/mK at 8 GPa	Sintered at 2100 K
Choi *et al.* 2003	External Magnetic Field	Carbon nanotube Polymer Composite	K increases 10%	Magnetic Field CNT Alignment Processing
Mintsa *et al.* 2008	External Temperature Field	Water/ Al_2O_3 nanofluid (9 vol. %)	15% increment in effective K	20-40 ºC

Yamashita *et al.* 2011	External Magnetic Field	$BaFe_2(As_{0.67}P_{0.33})_2$	K varies from 0.244 to 0.248 W/mK with 2T magnetic field at different orientations	Extreme low temperature 1K
Hone *et al.* 1998	External Temperature Field	Single wall Carbon nanotube bundle	K of SWNT is linear increasing with temperature	7-25K
Wright *et al.* 2008	External Magnetic Field (Magnet)	Ni coated CNT/Fe_2O_3 nanoparticle/Water	1.1 W/mK at 620 Oe 1.01 W/mK at 380 Oe	Magnetic Field Alignment

1.2 Heat Conduction Theory

1.2.1 Classic Fourier Theory

For a classical, isotropic material, steady state Fourier's law states the local heat flux is proportional to temperature gradient to negative temperature gradient [1, 25]:

$$q'' = \frac{Q}{A} = -k \cdot \nabla T \tag{1}$$

where q" is heat flux in SI unit of W/m^2, Q is total amount of heat transfer in SI unit of W, A is cross section area perpendicular to heat transfer direction with unit of m^2, k is the thermal conductivity in SI unit of W/mK, ∇T is the temperature gradient in SI unit of ˚C/m.

Usually, in the material, one type of energy carrier k dominates the heat conduction process. Nevertheless for materials with multiple carriers, such as thermoelectric materials and aerogels, the total thermal conductivities can be combined together:

$$k = k_L + k_e + k_g + ... \tag{2}$$

where k is overall thermal conductivity, k_L, k_e, k_g is the thermal conductivity contributed by lattice, electrons and gas molecules, respectively.

1.2.2 Kinetic Theory

To further understand the physical meaning of thermal conductivity k, kinetic theory can be applied to derive k. Kinetic energy is the amount of energy of an object or particle because of its movement. The substance can be solids, liquids or gases. For solids, very strong attraction forces between molecules holds the particle in relative

fixed, regular arrangement. The particles can only vibrate locally around their fixed positions. For liquid molecules, the attraction forces between molecules are weaker than that for solids, they have more energy than solid molecules and can move in low speed to form irregular arrangement. Lastly, for gas molecules, due to the negligible attraction forces between molecules, they can travel in random direction in relative high speed.

When solid substance is heated, the particles will gain more kinetic energy, which causes them to vibrate more rigorously. The extra kinetic energy is passed to neighboring particles, and eventually, the kinetic energy is passed through the solids. As a result, the temperature of the whole substance will rise.

Figure 1-2 Temperature Gradient across the Substrate

$$E_{total} = c\frac{\partial T}{\partial x} l_x \tag{3}$$

$$l_x = v_x \tau \tag{4}$$

where, E_{total} is the total energy, c is the heat capacity, $\frac{\partial T}{\partial x}$ is the temperature gradient along x direction, l_x is the mean free path, v_x is particle velocity in x direction, τ is relaxation time.

$$q''_{net} = (nv_x)c\frac{\partial T}{\partial x}v_x\tau \tag{5}$$

$$q''_{net} = C\frac{\partial T}{\partial x}v_x^2\tau \tag{6}$$

where nv_x is the net particle flux, C (C=nc) is the total heat capacity.

To generalize the equation in 3 dimensions, the average velocity can be expressed as:

$$v_x^2 = v_y^2 = v_z^2 = \frac{1}{3}v^2 \tag{7}$$

By substituting Equation (5) back to Equation (4), we get the following form:

$$q''_{net} = \frac{1}{3}Cv^2\tau\nabla T \tag{8}$$

Compared to the Fourier law, the Equation (6) can be expressed in thermal conductivity term k in the following form:

$$k = \frac{1}{3}Cvl \tag{9}$$

where k is the thermal conductivity of the substance, C is the total volumetric heat capacity in unit of J/m^3K, v is the average particle velocity in unit of m/s, and l is the mean free path in unit of m.

Normally, more than one source of scattering is present, such as impurities and lattice phonons. For multiple scattering mechanisms i can be combined using Matthiessen's rule [26]:

$$l^{-1} = \Sigma l_i^{-1} \tag{10}$$

1.2.3 Electrons in Metals and Semiconductors

In pure metals, the energy carrier is dominated by free electrons. However, in heavily doped semiconductors, the electron contribution k_e comes from dopant can be comparable to lattice contribution k_l to the overall thermal conductivity. In both cases, the electron conduction mechanism needs to be understood. Because the free electrons carry both charge and heat, there is a very important relationship between electrical conductivity σ and its contribution to thermal conductivity k_e known as Wiedemann-Franz Law:

$$\frac{k_e}{\sigma T} = L \tag{11}$$

where, k_e is thermal conductivity contributed by free electrons, σ is the electrical conductivity, T is the temperature in unit of K, L is the Lorentz number.

Wiedemann-Franz law indicates that for certain materials, the electrical conductivity is proportional to its thermal conductivity at given temperature. For a free electron with parabolic dispersion near Fermi energy, like most metals, with purely elastic scattering, which is caused by impurities and point defects at all temperatures. The Lorentz number has the following value:

$$L = \pi^2 k_B^2 \Big/ 3e^2 = 2.44e^{-8}\,\mathrm{W\Omega K^{-2}} \tag{12}$$

where k_B is Boltzman constant.

For semiconductors, the thermal conductivity is inherently linked to electrical conductivity through Wiedemann-Franz law. The thermal conductivity of the

semiconductors is composed of two components: electrons' contribution by free electrons and lattice vibration contribution by phonons. With known electrical conductivity and appropriate L of material, it is possible to estimate its thermal conductivity. For special cases where semiconductor is not heavily doped with other materials, L approaches to 1.5 x 10^{-8} $W/\Omega K^2$. If both n-and p- type carriers are present in the system, k_e has the following estimation form by considering ambipolar effect:

$$k_e = k_{e,p} + k_{e,n} + \frac{\sigma_p \sigma_n}{\sigma_p + \sigma_n}(S_p - S_n)^2 T \tag{13}$$

where, S_p and S_n are the n-type and p-type carrier Seebeck coefficient.

1.3 Magnetic Field

It is desirable to create magnetic fields with specific spatial distribution for many purposes in modern physics and technologies. There are a number of ways to generate magnetic fields. The easiest approach involves permanent magnetic materials. Permanent magnet usually suffers from low magnetic field strength, less than 0.5 Tesla. Another drawback for permanent magnet is that it cannot be shut down, which makes it not applicable for those applications require tuning or switch the magnetic field. Alternatively magnetic field can be generated through current-carrying elements. The latter method offers the flexibility to generate field with complicated spatial configuration and predetermined strength, which is a preferred choice in many applications.

Biot-Savart's law describes magnetic field generated by an electric current. It relates magnetic field *dB* at a point in space to a line element *dl* carrying steady current I:

$$dB = \frac{\mu_0 I dl \sin\theta}{4\pi r^2} \tag{14}$$

Here r is the distance from the point in the equation to current carrying element, and μ_0 is absolute permeability of air or vacuum and its value is 4π x 10^{-7} W_b/Am in SI unit system, dl is the infinitesimal length of conductor carrying electric current I. θ is the angle between r and I.

By arranging current-carrying elements into specific designed spatial patterns, magnetic field with desired spatial distributions can be created. The flexible design is accomplished by discretizing cylindrical surface into infinitesimal triangle sub-regions, and for each sub-region, the current flow stream function formulation is applied to generate magnetic field [27]. With electric current following through current-carrying element comes Ohmic/ Joule Heating Q:

$$Q = I^2 R_{elec} \tag{15}$$

Where, R_{elec} is he resistance of the current carrying element and *I* is the current.

Superconductive materials have R_{elec} approaching to zero, and thus Ohmic heating is no longer a major concern. However, up to date technology achieves superconductivity at very low temperature (typically 4K), which requires cryogenic device and low temperature technologies. In addition, the electric current inside superconductive wires cannot be readily changed. Thus superconductive materials have been mostly applied

to generate very strong magnetic field of constant magnitude (*i.e.* not variable over time), such as those used for particle acceleration and NMR. Conventional current-carrying wires, such as copper wires, are preferred as current-carrying element to generate magnetic field. Magnetic field is linearly proportional to electrical current I (Equation (15)), while Ohmic heating is proportional to I^2 (Equation (16)). In cases when current reaches a few hundred amperes, the resulting Ohmic heat can be tremendous, which poses thermal limitation for the overall performance of magnetic field.

To deal with excessive heating issues, researchers have to suppress Ohmic heating by either decreasing electrical resistances by increasing the electrical conductor diameter or lowering the pumped current. Alternatively, the overheating problems are remedied by introducing advanced cooling technology. Lemdiasov *et al.* proposed a design a 3 axis gradient coil magnetic field with AWG 20 wire at 100 Amp working condition [27]. Chornik *et al.* applied rectangular wire to maximize copper cross-section as current carrier to minimize the Ohmic heating. Their system was also equipped with 7 mm diameter copper tubing carrying forced water cooling at the flow rate of 5 L/min to work under 100 Amp condition [28]. Goodrich *et al.* constructed a small-bore insertable gradient coil for a 75 Amp DC current for continuous operation. From the temperature rise test, the average temperature increment for Z axis was 37 ˚C, where the maximum temperature was measured to be 51 ˚C [29].

Chapter 2 Thermal Properties Characterization Techniques

2.1 Introduction

While the classic steady state Fourier law for thermal conductivity measurement is straightforward, the accurate measurements are sometimes very challenging. During the past a few decades, numerous experimentalists have explored different approaches to perform accurate thermal conductivity measurement for various substances. The thermal conductivity value for different materials can vary between several orders of magnitude. For example, the thermal conductivity for aerogels is around 0.015 W/mK, however, the thermal conductivity for diamond can be as high as 2000 W/mK. In general, it is very challenging to accurately measure material thermal conductivity in a wide range using one specific method.

Based on specimen temperature-time profile, the thermal conductivity characterization techniques can be divided into two categories: transient method and steady state method. Steady state methods measure the thermal conductivity of a sample by monitoring temperature distribution that is independent on time. Most commonly used steady state methods includes guarded hot plate and radial heat flow method. On the other side, transient techniques measure time dependent temperature dissipation behavior within the sample, which includes hot wire method, laser/Xenon flash method, transient plane source method and 3-Omega method. The use of transient method is advantageous over steady state methods for rapid measurements. In order to measure the thermal conductivity with appropriate technique, several rules need to be

followed: (1) understand the measurement requirement for sample geometry and material preparation process; (2) be familiar with fundamentals of each measurement techniques, advantages and disadvantages; (3) understand the potential system error associated with each measurement technique [30].

2.2 State-of-the-art Measurement Technique

2.2.1 Radial Heat Flow Method

When dealing with thermal conductivity measurements at high temperature (temperature > 1000 K), the radial heat flow method has a schematic showing in the Figure 2-1. The sample is heated internally at the center axis by a wire heater and the heat is propagated radially through the sample in all directions. The thermocouples can be placed at specified locations and collect the temperature distribution data within the sample. The thermal conductivity of the sample is derived from Fourier's law in cylindrical coordinate:

$$k = \frac{Q \ln(r_2 / r_1)}{2\pi H \Delta T} \tag{16}$$

where, r_1 and r_2 are the radius where two thermocouples are located, H is sample height and ΔT is temperature difference between thermocouples, Q is input heat flow rate.

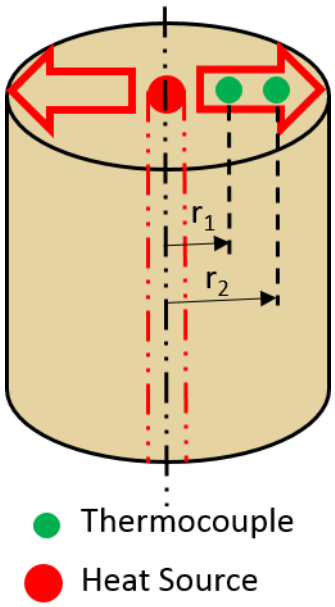

Figure 2-1 Schematic of radial heat flow method

2.2.2 Hot Wire Method

Hot wire method for thermal conductivity measurement is a transient technique that embeds an electrically heated wire (usually platinum) as heat source into a material. Due to the embedded heater requirement, the samples are generally limited to foams, fluids, oils and melted plastics, with easy approach to embed the heating element inside the material interior. Then the temperature rise at given location is monitored over a known time interval. During test the heating wire begins to spread the heat throughout the sample in every direction. Based on different material thermal conductivity, heat can be spread out at various rate. For higher thermal conductivity material, it is easy to conduct heat away from the heat source, while for the low thermal conductivity material, the heat is accumulated around the heating element. The thin wire can simultaneously work as a heat source and a temperature sensor. By measuring the

temperature of the wire versus the logarithm of time, the thermal conductivity can be obtained [31-33]. The advantage of using hot wire transient method is that for heating element, it is achievable to obtain high length to diameter ratio, which makes the heating element a perfect line source. However, the major disadvantage is by using resistance thermometer usually comes with an error in the input power. The material for heating element is generally platinum, the resistance of platinum will increase with higher temperature, thus results in non-constant input power during the measuring process. Schematic of such measurement system is shown in Figure 2-2 [32].

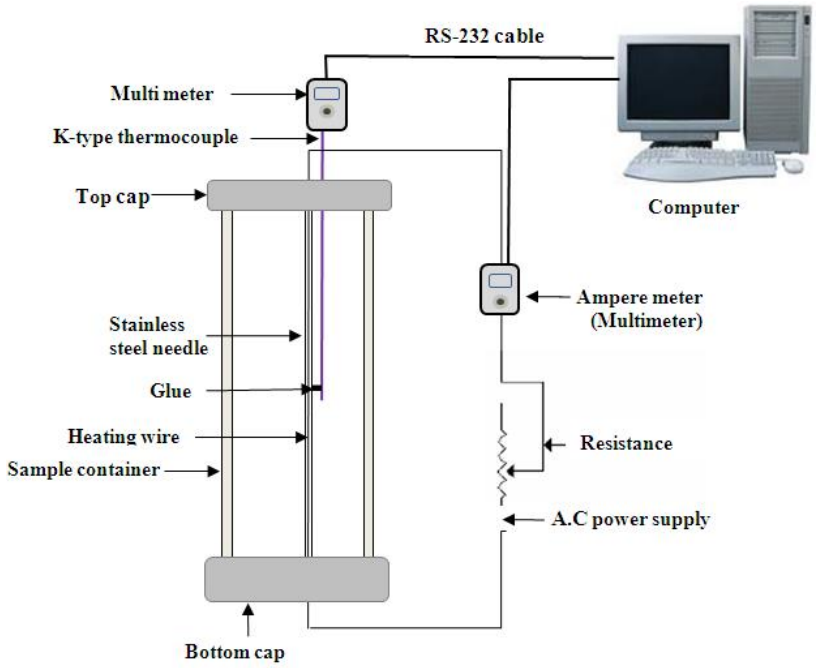

Figure 2-2 Schematic of Hot Wire Thermal Conductivity Measurement System [32]

2.2.3 Laser Flash Method

Contact thermal resistance poses a noticeable error for temperature measurement of thermal conductivity tests. The laser flash methods employ non-contact temperature

sensing technique to achieve high accuracy. An optical laser is usually used as heat source to heat one side of the sample, and the time dependent thermographic images on the other side of sample will be captured by Infrared (IR) camera as presented in Figure 2-3 for laser flash method schematic. The laser flash method does not directly measure the thermal conductivity of sample, instead, it measures the thermal diffusivity first, then according to the other properties such as density and heat capacity to back calculate the thermal conductivity based on the thermal diffusivity definition.

$$\alpha = \frac{k}{\rho c_p} \tag{17}$$

where α is thermal diffusivity, ρ is density and c_p is the heat capacity.

To accurately calculate total power input and measure the temperature contour of the sample, usually both sides of the sample are spray-coated with a thin layer of graphite coating with calibrated emissivity. With known density and heat capacity properties, the thermal conductivity can be calculated. Due to the possible error in temperature profile, density and heat capacity measurement, this technique usually suffers from relative low accuracy compared to steady state method. However, it is useful for comparing similar material or structure. The advantages for laser flash method include quick test and also it can be used to test thermal conductivity for small samples (5-12 mm in diameter) [34].

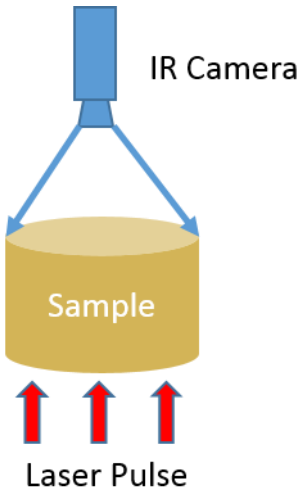

Figure 2-3 Schematic of Laser Flash Method for Thermal Conductivity Measurement System

2.2.4 3-Omega Method

Another commonly used technique to characterize thermal conductivity of material is 3-Omega (3ω) method. It is widely used for thermal conductivity measurement for both bulk and thin films materials. A metallic strip is deposited on top a substrate. Due to its thin feature, the metallic strip can be treated as infinitely long heat source in the mathematical model. It utilizes a very thin metal strip as both heater and thermometer on the samples or suspended in the material in liquid phase. The alternating current (AC) passing through the strip with frequency of ω will generate thermal wave at 2 ω frequency. Then the temperature increases at 2 ω frequency, which is directly related to the oscillating resistance at 2 ω frequency. Overall a voltage component of 3 ω is obtained during measurement. Since the 3 ω voltage signal is usually three orders of magnitude lower than amplitude of applied 1 ω voltage, a lock-in signal amplifier is required. The AC current is preferred in this 3 ω technique since it requires less

equilibration time and less vulnerable to radiation losses. The thermal conductivity of materials will be determined by analyzing the slope of 2 ω temperature rise of the metal wire with respect to the AC current frequency ω. Due to high aspect ratio between thin wire diameter and the specimen dimension, the heat affected region is confined in a very tiny region. Only regions near the metallic strip will be heated, and temperature oscillation decays exponentially in the surrounding areas. Compared to the hot wire method, the temperature rise can be controlled in a small range, (less than 5K), where material properties can be reckoned as constant. The test materials can be extended to dielectrics [35], porous materials [36], and carbon nanotubes [37] in the range of 30 to 1000 K. A commonly used 3 Omega thermal conductivity test setup schematic is shown in Figure 2-4.

$$I(t) = I_0 \cos(\omega t) \tag{18}$$

where I_0 is the current amplitude.

$$\Delta T(t) = \Delta T_0 \cos(2\omega t + \varphi) \tag{19}$$

where ΔT_0 is the temperature change amplitude, φ is phase.

$$\mathrm{R}_e(t) = \mathrm{R}_{e,0}(1 + \alpha_R \Delta T) = \mathrm{R}_{e,0}(1 + \alpha_R \Delta T_0 \cos(2\omega t + \varphi)) \tag{20}$$

where, α_R is the temperature coefficient of resistance of heater material. $R_{e,0}$ is the initial electrical resistance of heater.

$$V(t) = I(t)R(t) = R_{e,0} I_0 \cos(\omega t) + \frac{1}{2} R_{e,0} I_0 \alpha_R \Delta T_0 \cos(\omega t + \varphi) + \frac{1}{2} R_0 I_0 \alpha_R \Delta T_0 \cos(3\omega t + \varphi) \tag{21}$$

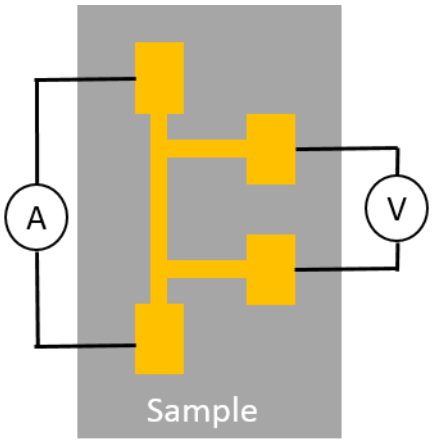

Figure 2-4 Schematic of 3-Omega Transient Thermal Conductivity Measurement System

A significant advantage of 3 omega method over conventional steady state method is the error due to the radiation loss is very small. Even at extremely high temperature, for example 1000 K, the radiation error is less than 2% [38]. However, the challenge involved with this method is microfabrication for metallic heater. Table 3 lists the comparison of various thermal conductivity characterization techniques [30].

Table 2-1 Comparison of Various Thermal Conductivity Characterization Techniques [30].

	Radial Heat Flow Technique	Laser Flash Technique	3 Omega Technique	Hot Wire Technique
Nature	Steady State	Transient	Transient	Transient
Temperature Range (ºC)	Up to 800	-120-2800	Up to 800	
Non-Destructive	Depends	No	No	Depends
Test Time	Hours	Seconds	Seconds	Minutes
Advantage	Reduce Radiation Heat Loss	Non-contact Temperature Sensing	Bulk and Thin Film Samples	Powdered/ liquid samples
Challenge	One Dimension Assumption	Other Physical Property Needed	Metallic Heater Microfabrication	Thin wire manufacture

2.3 Our Material Thermal Conductivity Characterization System

2.3.1 Electrical Heater-Thermocouple System for Thermal Conductivity Characterization

The thermal conductivity along the specimen can measured by applying hot plate steady-state method. The specimen with known dimensions is sandwiched between an

electrical heater and a heat sink. Two K type fine gage thermocouples were employed to measure the temperature difference ΔT across a distance L, as shown in Figure 2-5 [39]. To minimize heat loss, the sample is placed in a vacuum chamber with a heat shield. The temperature and electrical power data are recorded using a NI LabVIEW software. When steady-state is reached, the thermal conductivity of the sample is determined by applying Fourier's law:

$$K = \frac{Q_s L}{A\Delta T} \tag{22}$$

where Q_s is the power flowing through the sample, L is the distance between the thermocouple leads, A is the cross section area of the sample through which the power flows, and ΔT is the temperature difference measured across distance L.

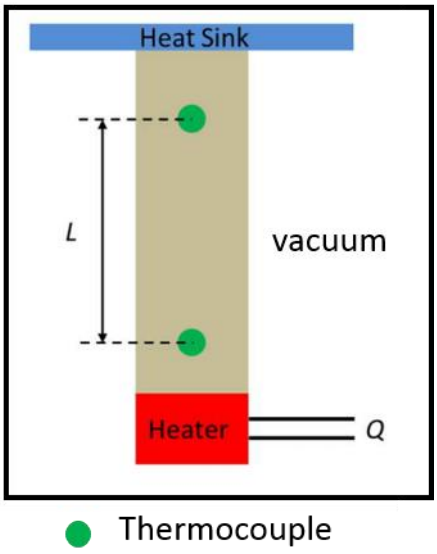

Figure 2-5 Schematic Illustration of Steady-state Electrical Heater- Thermocouple Thermal Conductivity Characterization [39]

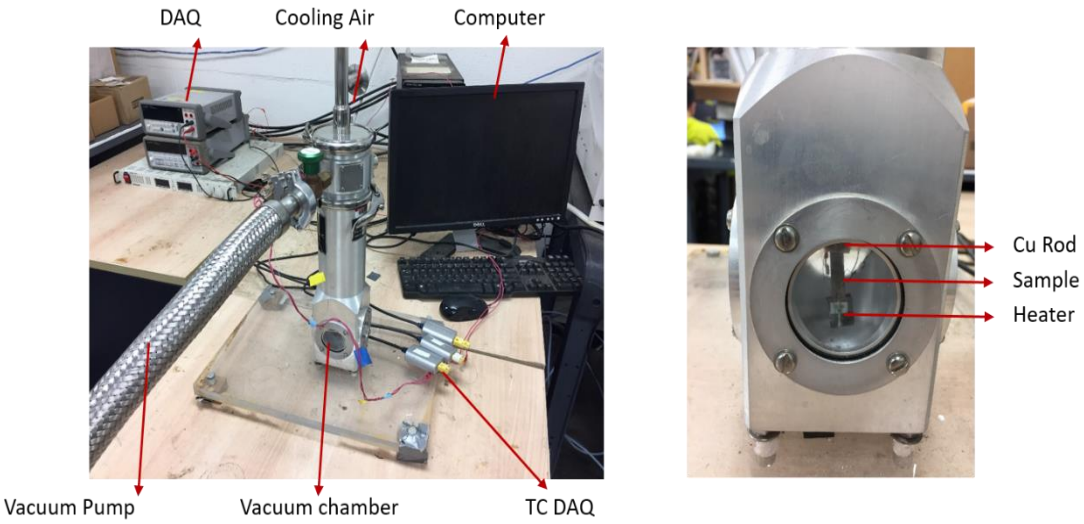

Figure 2-6 Electrical Heater-Thermocouple System for Thermal Conductivity Characterization

If there is no heat loss, all the power supplied to the heater flows through the sample and into the heat sink; therefore the heat flowing across any cross section would be constant. In actual measurements, heat loss is inevitable through radiation, convection and heat conduction through electrical wires connected to the heater, so the power flowing through the sample Q_s can be written as:

$$Q_s = Q_{in} - Q_{loss} \tag{23}$$

where Q_{loss} is the power lost by radiation, heat conduction through the connection leads and convection.

Calibration experiments were performed for stainless steel (K =16 W/mK), aluminum plate (K = 205 W/mK) and copper alloy 110 (K =380 W/mK). The uncertainty of the thermal conductivity measurement along the film samples is about 10%.

2.2.3 Laser-Infrared Camera System for Thermal Conductivity Characterization

In conventional hot plate steady state thermal conductivity measurement approaches, thermocouples and electrical heater as heat source are widely used. There are some inevitable system uncertainty/ errors induced by thermocouples, such as the size of thermocouple junction, type, the large thermal contact resistance between thermocouple junction and the specimen surfaces, location of junction *etc*. While electrical heater as heat source suffers from possible heat conduction losses through electrical wires connected the heater. Such system error induced by contact resistance of thermocouples and power loss through electrical wires from heat sources can be catastrophic to low thermal conductivity material characterization. Although high thermally conductive thermal paste and power loss correction formula for electrical heater can be applied to compensate those parasitic effects, the accuracy of results are still not satisfying. Thus a non-contact technique for temperature detection using infrared camera and laser incident heat source have attracted attention from many researchers.

Therefore, a Laser-Infrared camera steady state thermal conductivity measurement system is proposed with the schematic shown in Figure 2-7. The vacuum chamber is used to minimize the natural convection heat loss between specimen and ambient environment. With vacuum pressure less than 8E-5 kPa, there is negligible natural convection around specimen. Apart from natural convection heat loss, the radiation heat loss from specimen to ambient environment can be significant for low thermal conductivity materials since the radiation heat transfer resistance and conduction

thermal resistance may be at the similar order of magnitude. Without proper remediation of radiation heat loss will lead to higher thermal conductivity result for specimen. Therefore, a finite element model is built in ANSYS V 18.1 to mimic the actual thermal conductivity test condition with consideration of radiation heat transfer from specimen to ambient environment. The radiation function for the model is enabled and the thermal conductivity is fine tuned to match experimental temperature distribution results.

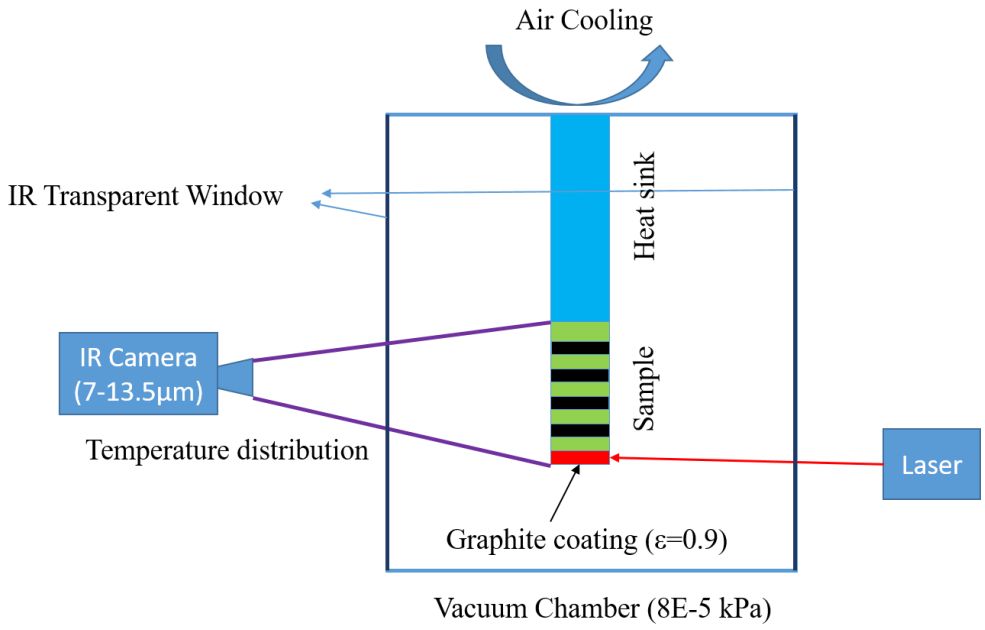

Figure 2-7 Schematic of Laser-IR Camera System for Thermal Conductivity Characterization

Laser with adjustable power is used to deliver variable heat flux as heat source for a wide range of thermal conductivity characterization. For specimen with low thermal conductivity, such as wood or telfon, low heat flux is required to prevent overheating

phenomena around hot spot, while for highly conductive materials, such as aluminum or copper, a relative high heat flux input is crucial to generate noticeable temperature distribution along the specimen. Although the overall system complexity is introduced due to the laser and supporting optical system, the adjustability of local hot spot size, location and input laser power provides wider application range for variety of specimens. Laser power calibration is performed by using ThorLabs 332 C power detector. 465 nm Blue DPSS laser with a beam size of 5 mm x 6 mm is used as heat source. The overall power fluctuation is less than 3% over 4 hours. The temperature profile is captured by FLIR T450Sc Infrared camera with microbolomer sensor resolution of 320 x 240 pixels. The internal uncooled mechanism enables the sensor to capture the irradiation within the wavelength between 7 and 13.5 μm. The overall accuracy of such IR camera is +/- 2 ºC or 2% of reading over temperature range of 0-650 ºC.

Due to the necessity of vacuum chamber to minimize natural convection effect, the windows on the vacuum chamber needs to be IR transparent for both IR camera and laser heat source. Based on different wavelengths, CaF_2 and KBr have been chosen as window material for high transmission properties (> 90% transmission rate with experimental validation) for laser heat source and IR camera, respectively. Those transmissivity of IR window will be taken into consideration of IR camera and input laser power calibration.

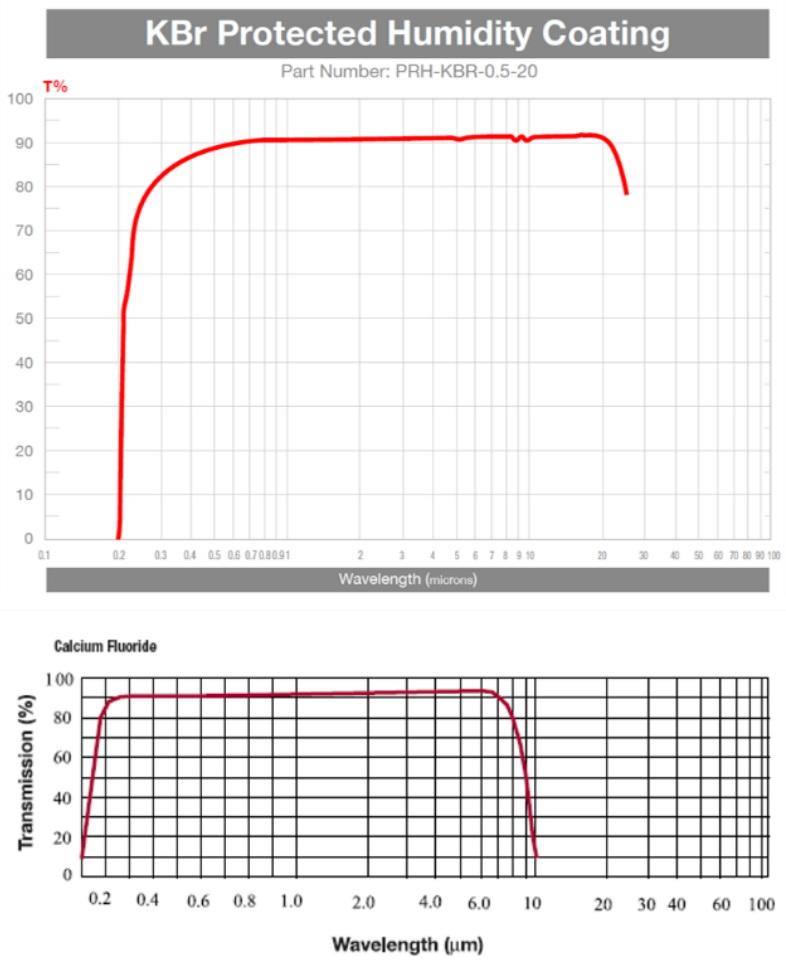

Figure 2-8 IR Transparent Window Materials Transmission Properties for Laser (CaF_2) [40] and IR Camera (KBr) [41] at Different Wavelength Ranges

Standard material stainless steel 316 was used to calibrate the accuracy of Laser-IR Thermal Conductivity Measurement System. From the experimental listed below, the thermal conductivity was fined tuned in ANSYS to match experimental temperature distribution. To fully capture the temperature distribution along the specimen by IR camera without introducing disturbance of heat transfer path, 5 thin graphite coating

strips (emissivity is 0.9) were applied perpendicular to heat transfer direction using graphite spray coating over a stencil with fixed spacing.

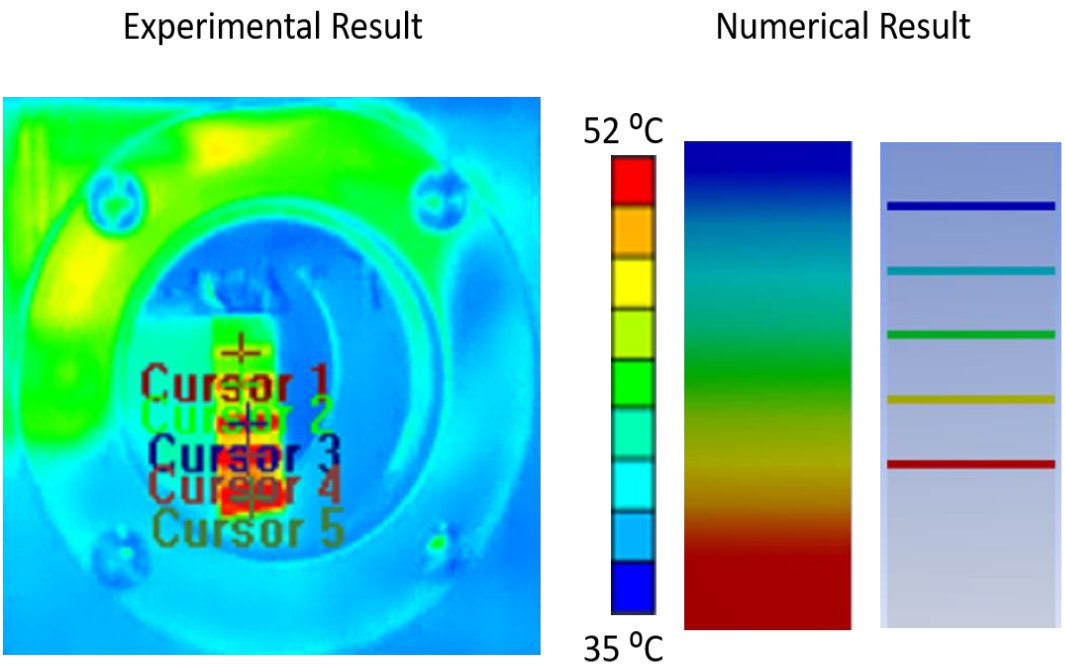

Figure 2-9 Laser-IR Thermal Conductivity In-Plane Measurement System Validation

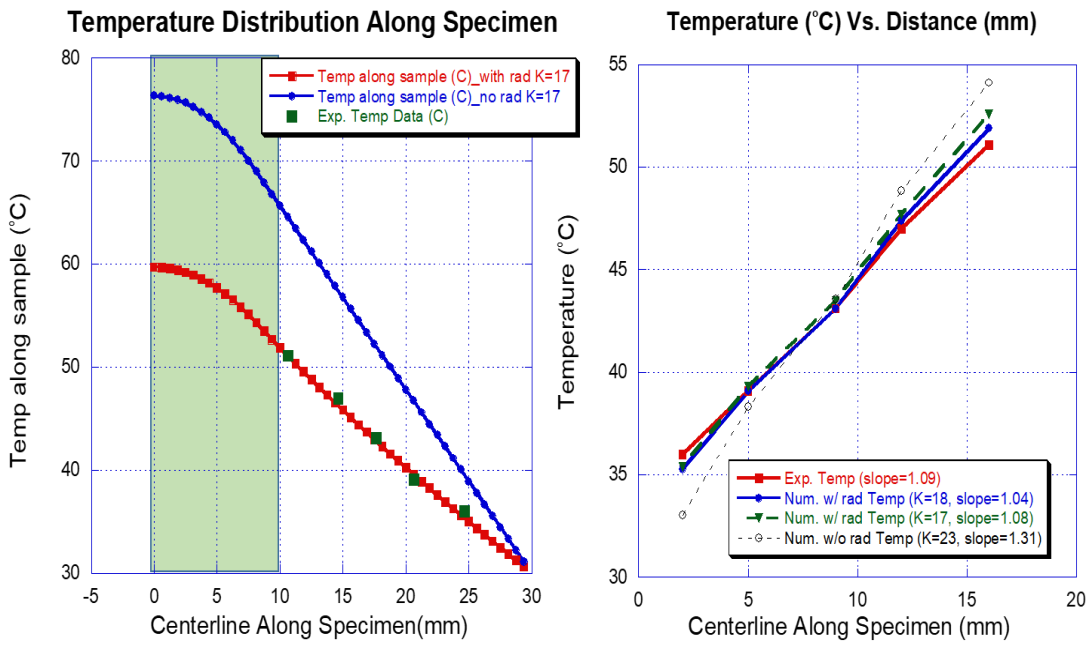

Figure 2-10 ANSYS Numerical and Experimental Data Comparison with and without Radiation Function

From Figure 2-10, it is easily seen that with radiation model, when the specimen thermal conductivity was fine tuned to 17 W/mK, it matched the experimental temperature distribution data very well. However, if the radiation effect was suppressed, the temperature distribution slope was much higher than experimental data. To match experimental result, the material thermal conductivity needs to be increased around 23 W/mK to flatten the temperature distribution slope. The green shaded box (laser power input and distributed region) marks the laser side graphite coating region, to ensure all the incident laser power is absorbed and evenly distributed along the specimen, a 10 mm region is coated at the laser side. As a result, the temperature distribution within this region is not used for thermal conductivity characterization.

The effect of radiation heat losses is further demonstrated in Figure 2-11. Since the numerical simulation temperature distribution result agrees with the experimental data well, some insights about effect of radiation heat losses can be further explored. In ANSYS, temperature distribution along specimen centerline are plotted in Figure 2-11 with and without consideration of radiation heat loss. For no radiation model, the temperature gradient after laser power input and distributed region shows constant temperature gradient slope and heat conduction total power, which is reasonable given that there is no additional heat losses other than heat conduction due to energy conservation law. However, once the radiation heat loss model is activated, the temperature distribution along specimen centerline shows a much different behavior compared to that of no radiation model. With radiation model, both temperature gradient and conduction power keeps decreasing due to the loss of power through radiation. Given the fact that the radiation model matches experimental very well, we have reasons to believe even under small temperature difference between specimen and ambient environment, the radiation heat loss is not negligible especially for poor thermal conductive materials. The underlying explanation can be verified with radiation and conduction thermal resistance comparison. For high thermally conductive materials such as aluminum (K=200 W/mK) and copper (K=400 W/mK), the difference between radiation model and non-radiation model is small.

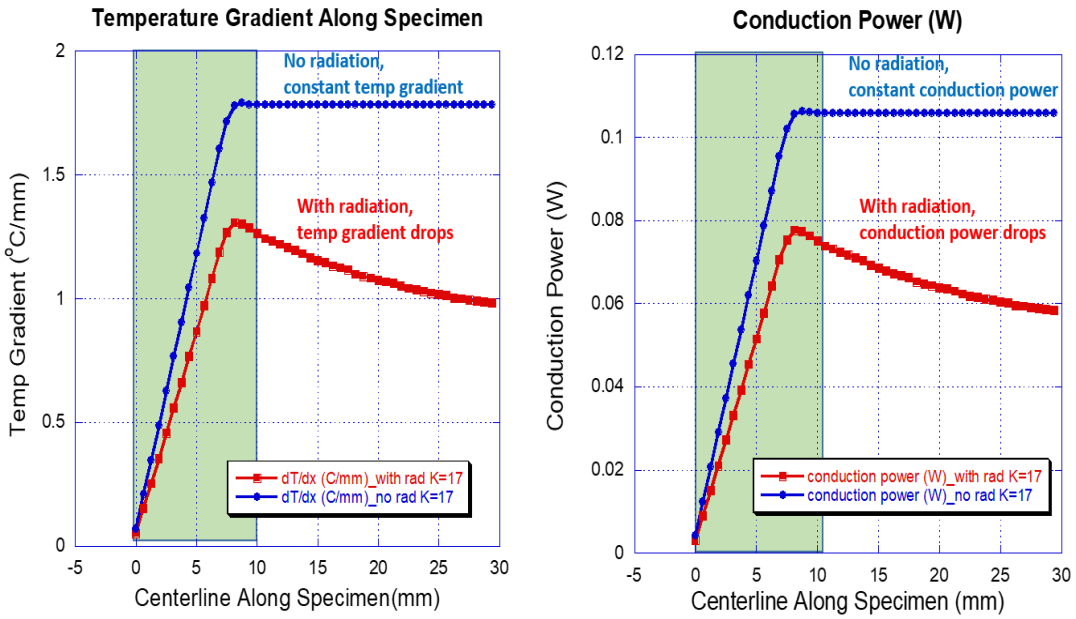

Figure 2-11 Effect of Radiation Heat Loss Demonstrated by Temperature Gradient and Heat Conduction Power

(blue line: no radiation model, red line: with radiation model)

In Table 4 below, several standard materials are tested to further validate the overall accuracy of the Laser-IR Camera Thermal Conductivity Measurement System.

Table 2-2 Laser-IR System Accuracy Validation on Standard Materials

Specimen Name	Literature Thermal Conductivity (W/mK)	Thermal Conductivity Data Obtained Using Laser-IR System (W/mK)
Wood	0.1 (radial direction) 0.2 -0.25 (longitudinal direction)	0.13 (radial direction) 0.3 -0.25 (longitudinal direction)
Teflon	0.25	0.24
Stainless Steel (316)	16-18	16.5
Aluminum	180-200	183
Copper	380-401	390

Chapter 3 Material Thermal Properties Modification with Nanostructured Materials

3.1 Introduction

Technology development experiences exponential boost trend because of the information explosion. As electronic devices becomes smaller and smaller in size, the resulting increased power density poses challenges for thermal management system used in electronic systems. In many cases, the local hotspot temperature rather than average temperature is the limiting factor of system's performance and reliability [42, 43]. Generally, the thermal management approaches incorporated in electronic systems are classified in two categories based on their external energy consumption status: active cooling and passive cooling. Circulating coolant by pump or fan involves consuming external energy, which is reckoned as active cooling method. Despite their exceptional cooling performance, active cooling approaches not only tend to make the entire system bulky and complex, but also consume extra energy. Moreover, the noise and vibration of active cooling approaches will compromise the reliability of the system. On the other hand, passive cooling mainly relies on thermal management material intrinsic properties rather than external power, which can overcome certain drawbacks for active cooling method. Therefore thermal management performance of passive cooling methods depend heavily on material properties, which has been an attractive research topic for both industry and academia.

Most of the electronics system incorporates substrates, such as plastics or polymers during fabrication or assembly processes. However those materials generally bare poor thermal properties, which makes them less ideal candidates for thermal management system. Due to their unique functional and irreplaceable properties of such substrates in the systems, much effort has been placed on improving their overall thermal properties by introducing other highly thermally conductive materials as filler. Carbon or metal particle based fillers including graphene and Al_2O_3 nanoparticles have been proven to improve overall thermal and electrical conductance of the base–filler composite at various loading ratio effectively. Unfortunately, the electrical conductance of such carbon or metal based filler in the composites significantly hampered their applications in electronic systems. Therefore, designing a thermally conductive composite with excellent electrical insulating properties is urgent for electronic system thermal regulation.

In comparison to thermally and electrically conductive graphene containing single type of carbon atoms, heteroatomic 2D nanomaterials hexagonal boron nitride (h-BN) also has superior thermally conductive but electrically insulating properties [44-46]. Shown in Figure 3-1, hexagonal boron nitride is comprised of alternating B and N atoms in a "honeycomb" lattice structure similar to graphite. In plane, sp^2 -hybridized B and N atoms are covalently bound, whereas neighboring cross planes are held together by van der Waals forces. However, the Van der Waals forces between adjacent BN layers are stronger than that of graphite due to the electronegativity difference between B and N atoms. Such thermally conductive, electrically insulating and chemical stability

properties of h-BN makes it a very promising thermal management candidate to be incorporated in electronic systems [47].

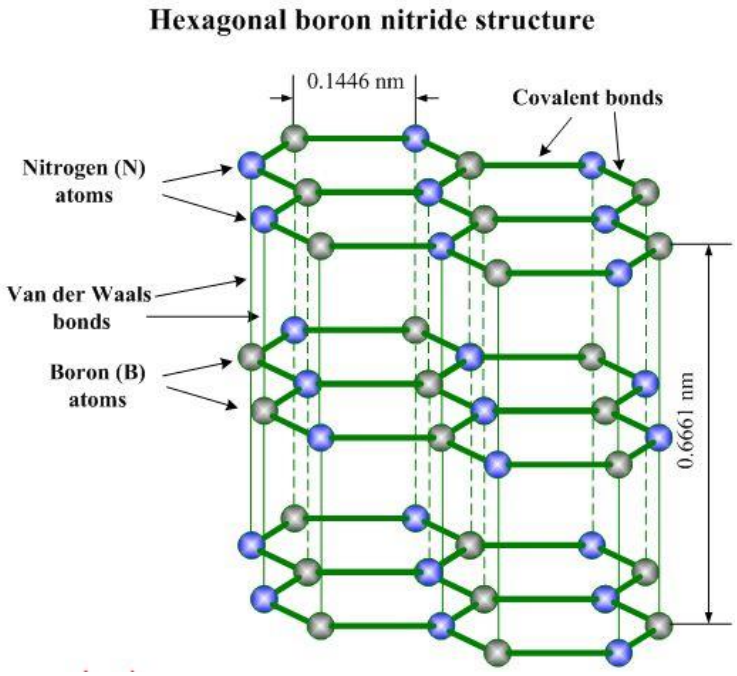

Figure 3-1 Schematic of Hexagonal Boron Nitride Structure [48]

3.2 BN- based Composite in Power System

In "Thermally Conductive, Dielectric PCM–boron Nitride Nanosheet Composites For Efficient Electronic System Thermal Management" paper published at Nanoscale 2016 [49]. W.L., L.Z, and J.W. contributed to BNNS synthesis and material preparation. J.W. and Y.Y helped with XRD material characterizations, Z.Y. and B.Y. performed thermal conductivity measurement, heat of fusion measurement and characterization of electrical properties of samples. J.D. contributed to 3D figures. Z.Y., W.L. and K.F. drafted the manuscript. K.F. and D.H. contributed to grammar check. X.H., B.Y. and

L.H. contributed the idea and experiments design. All authors contributed the manuscript and comments on the final paper.

3.2.1 Motivation

With the rapid development of technology, the demand for denser integrated circuits, and smaller sizes and faster speeds of electronic systems continuing to spike; the cooling requirements of power flux in a system are remarkably high. The potential risk associated with the inadequate heat dissipation of electronic systems poses a greater risk for thermal issues and failures. It is reported that the percentage of over-heating related failures in electronic systems exceeds 55%. For example, the performance of lithium-ion batteries in electric vehicles (EVs) and hybrid electric vehicles (HEVs) will be compromised above 65 °C working conditions. Therefore, an efficient thermal management system with adequate heat dissipation capacity is crucial for enhancing the performance and reliability of the system [49]. Figure 3-2 shows the fire in Tesla Model S batter pack after thermal failure, which costs not only economical loss, but also poses safety risk to human.

Figure 3-2 Thermal Failure in Tesla Model S Battery Pack [50]

Fast response, easy maintenance and cost effectiveness of passive cooling have drawn significant attention from academia and industry. It should be noted that the passive cooling performance heavily depends on material properties. Among the various passive cooling materials, phase change materials (PCMs) have been widely adopted, which absorb and release heat during phase transition between solid and liquid state. In addition, the thermal stability during thermal cycling processes and uniform temperature distribution within PCMs are also favorable.

PCMs benefit from the large latent heat absorbed or released during phase change transition processes with a wide range of phase change temperatures for thermal management. Compared to other sensible materials, the incorporation of PCMs can achieve the same or even better performances with a smaller volume. To meet the thermoregulation requirements for different applications, various PCMs can be

selected. Zhong *et al.* reported a thermal management system using a PCM with a 58 °C phase change temperature and a 144 kJ/kg heat of fusion. Kandasamy *et al*. experimentally and numerically validated paraffin wax which helped maintain the temperature of an electronic chip below 80 °C for 4 hours as a thermal management material. However the poor thermal conductive property of PCMs, (than 1 W/mK) limits their thermal regulating capacity due to the fact that heat cannot be effectively dissipated through PCMs. This will lead to inefficient PCM utilization during the phase transition process, which hinders the overall performance of PCMs to be used as a thermal management material. In order to enhance the thermal conductivity of PCMs, different approaches have been reported. Unfortunately, the electrical conductance of many PCM–filler composites significantly hampered their applications in electronic systems. Therefore, designing a thermally conductive PCM composite with excellent electrical insulating properties is urgent for electronic system thermal regulation.

Paraffin wax, as a typical PCM material with a large heat of fusion, has a wide range of phase change temperatures that can be used for broad applications. The continuous BNNS network not only effectively enhances thermal conductivity and electrical insulating properties, but also provides mechanical support as matrix. The BNNS network effectively conducts heat throughout the entire composite, and the presence of paraffin wax in the Wax–BNNS network provides an additional heat transfer mechanism by incorporating the heat of fusion of wax during phase change processes, as illustrated in Figure 3-3. Highly thermally conductive and electrically insulating Wax-BNNS composites are promising candidates for thermal management

applications to be used in electronic systems, for example battery systems (Figure 3-3 (c)). The application can also be further extended to other microelectronic packaging systems requiring passive cooling thermal management with enhanced thermally conductive properties.

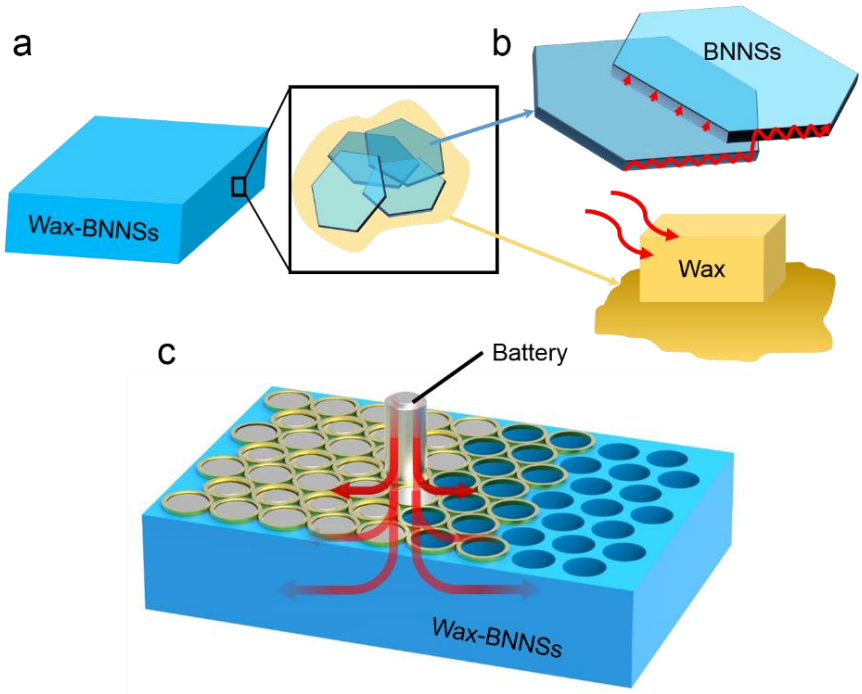

Figure 3-3 Schematic of Heat Transfer Mechanism in Wax-BNNSs Composite (a) Schematic of the Wax–BNNS Composite; (b) Heat Transfer Mechanism in the Composite: Wax Absorbs Heat from the Heat Source, (red line: heat dissipation path); BNNSs Conduct Heat within the Composite; (c) Potential Application of the Wax–BNNS Composite.

3.2.2 Wax-BNNSs Material Preparation

The Wax–BNNS composite was prepared by penetrating molten paraffin wax into the cavities left in a BNNS–NFC (Nanofibrillated Cellulose) freestanding film. Figure 3-4

(b) shows a transmission electron microscopy (TEM) image of the BNNS flakes, revealing their thin and transparent morphology. The lateral size of the majority of the BNNSs was concentrated between 200–500 nm. The large lateral size of BNNSs is desired to form continuous thermal networks with a small interfacial resistance to enhance heat transfer performance. To allow the penetration of molten wax, a porous freestanding membrane was prepared by using polystyrene spheres (PS) as sacrificial fillers mixed together with BNNSs and NFC to serve as a matrix for wax loading. The PS fillers had an average diameter of ~500 nm. After filtration process, the freestanding PS-BNNS-NFC film could be easily peeled off from the anodic aluminum oxide (AAO) membrane. Then the PS–BNNS–NFC film was immersed in a toluene solution to remove PS spheres embedded in the film. The BNNS–NFC film with cavities left by PS spheres was ready for molten paraffin wax penetration.

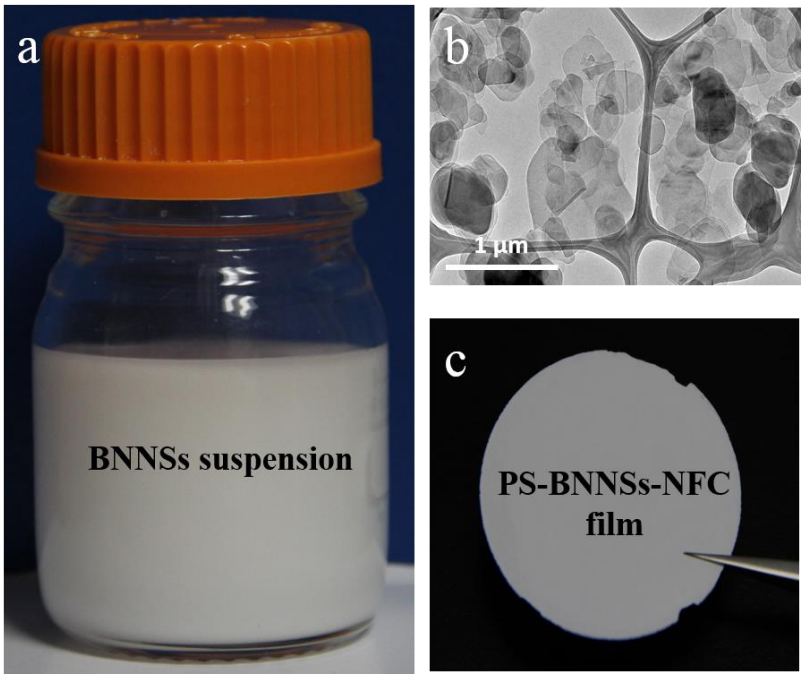

Figure 3-4 Preparation of PS-BNNS-NFC Film

(a) Digital Picture of the BNNS–NFC Suspension in IPA, (b) TEM Image of the BNNS Flakes, (c) Digital Picture of the Freestanding PS–BNNS–NFC Film.

Figure 3-5 shows the schematic and scanning electron microscopy (SEM) morphological characterization of key steps during the wax–BNNS composite fabrication process. Figure 3-5 (a) presents the schematic of the freestanding PS–BNNS–NFC film. The green and white regions shown in the schematic represent PS spheres and the BNNS–NFC network, respectively. The overlapping BNNS flakes form a continuous network to enhance the heat transfer performance within the composite. From the SEM image and the magnified SEM image of the PS– BNNS–NFC film in Figure 3-5(b) and (c), respectively, PS regions are circled with a green dotted line. The schematic of cavities in the BNNS–NFC film is shown in Figure 3-5(d). The white and black regions represent the BNNS network and cavities, respectively. The PS spheres as a sacrificial material were removed by immersing the PS–BNNS–NFC film in toluene solution to create a porous structure feature in the film. The SEM image and magnified SEM image of the BNNS–NFC film (Figure 3-5(e) and (f)) reveal that the BNNS–NFC film contains sufficient cavities left by PS. The random cavity size is due to PS spheres' agglomeration in the PS–BNNS–NFC film preparation process. Figure 3-5(g) shows the schematic of the Wax–BNNS composite, where the yellow and white regions represent paraffin wax and the BNNS–NFC network, respectively. The cavities previously occupied by PS spheres were successfully filled after wax penetration (Figure 3-5(h) and (i)). About 60 wt. % of paraffin wax in the wax–BNNS composite was obtained by measuring the mass change of the composite

before and after wax penetration. At this point, a freestanding Wax–BNNS composite was successfully synthesized. The wax in the composite provides large heat absorption capacity during its endothermic phase transition process, and the BNNS network enhances the thermal conductivity of the composite to effectively spread heat within the composite.

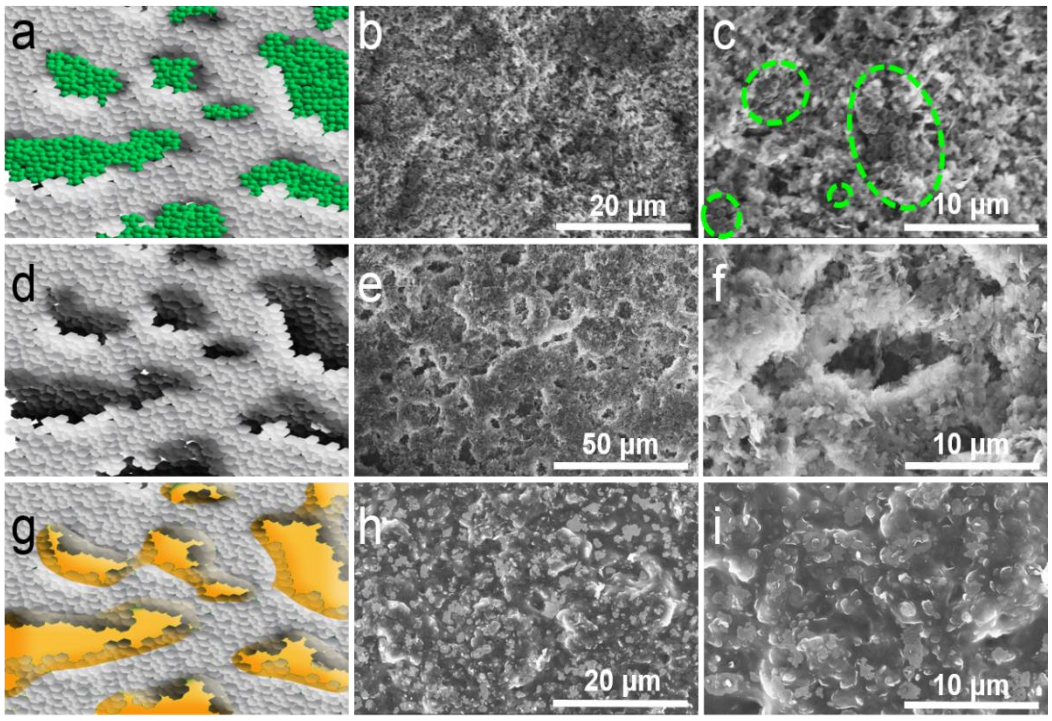

Figure 3-5 SEM Morphology Characterization

(a) Schematic of the PS–BNNS–NFC Film (green region: PS, white region: BNNS network). (b, c) SEM images of the PS–BNNS–NFC Film. (d) Schematic of BNNS–NFC after PS Removal (black region: cavity, white region: BNNS network). (e, f) SEM Images of BNNS–NFC after PS Removal. (g) Schematic of the Wax–BNNS Composite (yellow region: wax, white region: BNNS network). (h, i) SEM Image of the Wax–BNNS Composite

3.2.3 Wax-BNNSs Properties Characterization

To evaluate the application potential of the wax–BNNS composite, its thermal properties and electrical properties were characterized. Ideally, a high thermal conductivity and large heat of fusion are desired for materials to be used in thermal management system applications. Figure 3-6 illustrates the thermal and electric insulating properties of the Wax–BNNS composite. As shown in Figure 3-6 (a), the in-plane thermal conductivities of pristine paraffin wax, the Wax–BNNS film and the freestanding BNNS–NFC film (BNNS film for short) were measured to have value of 0.29, 3.47 and 30.6 W/mK, respectively, using a steady state method. By adding highly thermal conductivity BNNSs into pristine paraffin wax, the thermal conductivity of the Wax–BNNS composite increased 12 times than that of the pristine paraffin wax. The continuous BNNS network embedded in paraffin wax facilitates heat conduction throughout the network, which leads to a higher effective thermal conductivity of the Wax–BNNS composite, enabling an improved heat transfer performance of the composite for thermal management purposes. Apart from the superior thermal conductivity of the BNNS network, Figure 3-6 (b) characterizes the paraffin wax inside the Wax-BNNSs composite can provide large heat absorption capacity of 80.17 J/g during the endothermic process by differential calorimetry scanning (DSC) technique. The drop of ΔH_{fus} from wax to wax-BNNSs composite is attributed to wax mass reduction per unit volume. Liu and Chung reported a similar trend with the 20 wt % Al_2O_3–wax composite showing a decreased heat of fusion to 58 J/g compared to that

of pure paraffin wax. The excellent electrical insulating properties of BNNSs flakes further improves the breakdown voltage from 6.3-7.3 MV/m of pure wax to 11.3-13.3 MV/m in Figure 3-6 (c). The enhanced breakdown voltage of the wax–BNNS composite indicates that the wax–BNNS composite can tolerate a higher voltage difference threshold across the composite in electronic system.

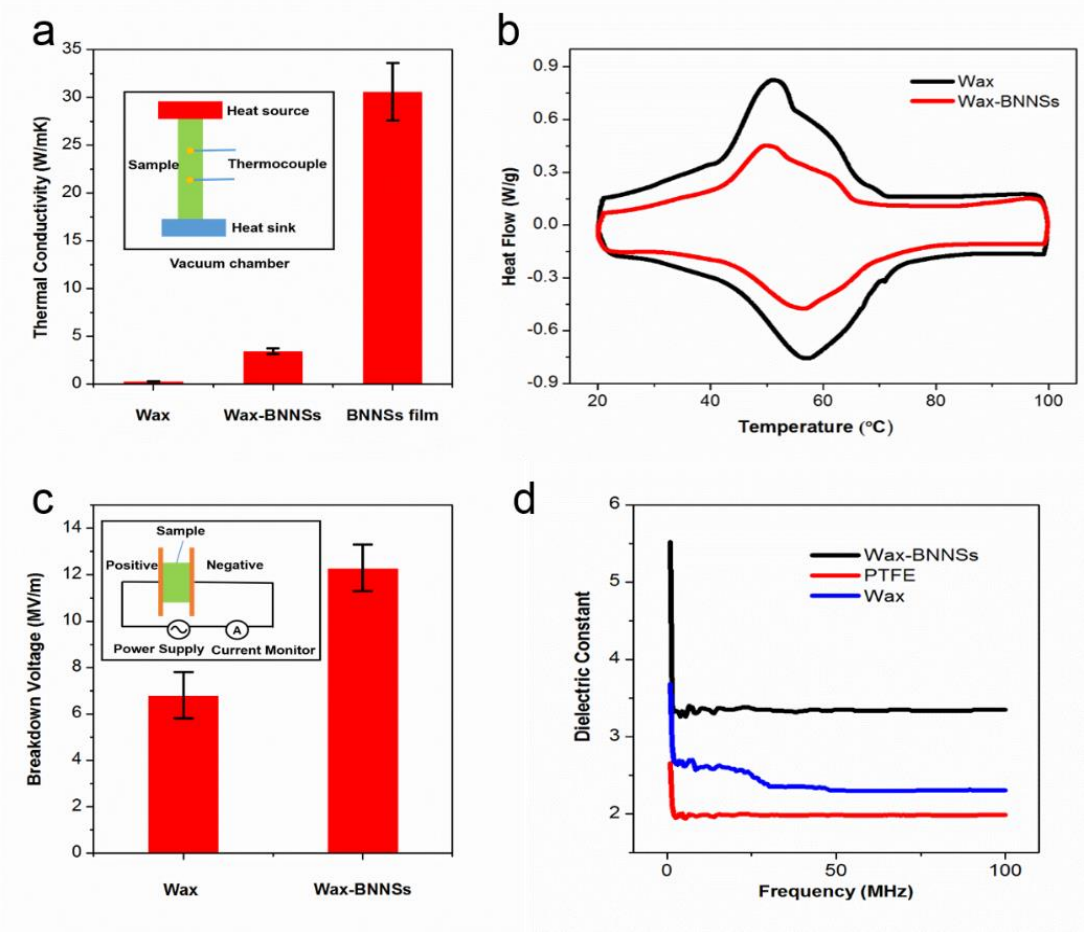

Figure 3-6 Thermal and Electrical Properties Characterization of Wax-BNNSs Composite

(a) Thermal Conductivity of Different Specimens. Inset is the Schematic of Sample Thermal Conductivity Measurement. (b) DSC Thermograph during the Phase Change

Process of Pristine Paraffin Wax and the Wax–BNNS Composite; (c) Breakdown Voltage of Different Specimens. Inset is the Schematic of Sample Breakdown Voltage Measurement. (d) Dielectric Constant of Different Samples

3.2.4 Experimental Section

Synthesis of the BNNS suspension

Pristine BN powder (Sigma-Aldrich Co., Ltd (US)) with particle sizes of ∼1 μm was used for BNNS exfoliation. To obtain a high concentration BNNS suspension, 1.5 g of pristine BN powder was added into 500 mL of isopropanol alcohol (IPA) at room temperature. The nanofibrillated cellulose (NFC) disintegrated from wood pulp was used as a dispersing agent based on the method of our previous studies. After 48 h of sonication, a white homogeneous "milky" BNNS–NFC suspension was obtained, indicating that the BNNS flakes were uniformly dispersed in solution. The measured concentration of BNNSs was 2.2 mg/ml. After being placed on a shelf under ambient conditions (22 °C, relative humidity 30%) for 24 h, the top 3/4th volume of the BNNS suspension was collected to exclude any possible precipitation near the bottom.

Preparation of the PS–BNNS–NFC film

214 mg of monodispersed polystyrene (PS) powder with diameter ~500 nm was added into 10 ml of IPA. The PS-IPA mixed solution was sonicated for 1 h in water bath to form a uniform solution. The concentration of the PS suspension was 21.5 mg/ml. The measured concentration of NFC solution was 1.0 mg/ml. The 4:5:1 mass ratio of PS: BNNSs: NFC was chosen based on our previous study to fabricate a stable and uniform

PS-BNNSs -NFC film. The mixed solution was prepared by first adding 300 mg of 1.0 wt. % NFC solution into 10 ml of deionized water under vigorous stirring at room temperature for 0.5 h. Then, 6.5 ml BNNSs suspension with concentration of 2.3 mg/ml and 560 mL of PS solution with concentration of 21.5 mg/ml PS were carefully dropped into the as-prepared solution. The PS-BNNSs-NFC mixed solution was stirred vigorously for 0.5 h, followed by water bath sonication at room temperature for 0.5 h to form a uniform suspension. Finally, the PS-BNNSs-NFC suspension was filtered with a Bucher funnel using anodic aluminum oxide (AAO) membrane. The as-prepared PS-BNNSs-NFC film left on the AAO membrane was dried at ambient conditions. The freestanding PS-BNNSs-NFC film could be easily peeled off from the AAO Synthesis of Wax-BNNSs Composite

The freestanding PS-BNNSs-NFC film peeled off from the AAO membrane was then immersed in toluene solution for 24 h to remove PS. PS was dissolved in the toluene solution while the BNNSs-NFC freestanding film remained intact. BNNSs-NFC freestanding film was then dried in a vacuum chamber at 80 °C for 24 h. The paraffin wax with a melting temperature of 42 °C was placed on top of the BNNSs-NFC film in the vacuum chamber for 24 h at 80 °C for wax penetration. At 80 °C, the molten wax penetrated into the cavities in the BNNSs-NFC film and covered the BNNSs network. The excess melted paraffin wax left on the Wax-BNNSs-NFC (Wax-BNNSs for short) composite surface was removed with filter paper before it solidified.

Thermal Conductivity of Wax-BNNSs composite Measurement

The in-plane thermal conductivity of Wax-BNNSs composite was determined by applying a steady state hot plate method using our electrical heater-thermocouple thermal conductivity characterization system. A 6 mm wide and 30 mm long Wax-BNNSs composite was placed between an electrical heater and a heat sink along the longitudinal direction. Two fine-gage K type thermocouples were placed on the samples to capture the temperature difference, ΔT, across a distance L. To minimize heat loss, the samples were placed in a vacuum chamber with a heat shield. The temperature and heater power data were recorded using a LabVIEW program from national instruments. The steady state Fourier conduction theory was used to determine the effective thermal conductivity of the Wax-BNNSs composite with the consideration of heat loss. Calibration tests for the thermal conductivity measurement system were performed with glass (K=1 W/mK), stainless steel (K =16 W/mK), and an aluminum plate (K = 205 W/mK). The uncertainty of the thermal conductivity measurement along the film longitudinal direction is about 10%.

Heat of Fusion of the Wax-BNNSs Composite

To further characterize the thermal properties of the Wax-BNNSs composite during the phase transition process, differential scanning calorimetry (DSC) was conducted on a DSC-Q100 provided by TA instruments, USA to characterize the samples thermal properties during the phase change process. For the DSC test, a 4.325 mg Wax-BNNSs composite sample was placed in a hermetic aluminum pan and sealed by an aluminum lid. The aluminum pan was placed in the DSC chamber with a heating and cooling rate at 5 °C/min from 20 to 100 °C at a 50 ml/min nitrogen gas purge rate. An 8.428 mg

pristine paraffin wax sample was tested under same test condition for comparison. Two cycles were tested for each sample to validate the result.

Electrical Properties of Wax-BNNSs Composite Characterization

For the breakdown voltage test, pristine paraffin wax and Wax-BNNSs composite samples were sandwiched between two electrodes in an electrical circuit. While increasing the voltage difference across the sample, the current in the circuit was monitored and recorded. The dramatic current spike due to short-circuit within the samples were monitored once the voltage difference across the samples reached the breakdown voltage threshold. The dielectric constant property was characterized with an Agilent E4991A RF Impedance/ Material Analyzer at the CALCE center, University of Maryland. With material dimensions and measured capacitance of the sample, the dielectric constant can be determined at various frequencies and test conditions. The pristine paraffin wax and the Wax-BNNSs composite were cut to a round shape with diameter of 15 mm and thickness of 0.3 mm. Each sample was sandwiched in 16453A dielectric material test fixture; dielectric constant of samples was tested at a frequency range from 1-100 MHz. The accuracy of the dielectric constant measurement is ±1%. The calibration test was performed on a standard PTFE material (theoretical dielectric constant is 1.99.

3.2.5 Conclusion

In this work, a Wax-BNNSs composite with improved thermal conductive and electrical insulating properties was fabricated and experimentally validated. The approach is scalable, low cost and ecofriendly. The 12 times enhancement in thermal conductivity makes the localized heat spread out through the composite more easily, which proves to be a promising candidate for PCM thermal management systems. In addition, 80.15 J/g latent heat of the composite can provide another heat absorption path during phase transition. When it comes to powering system application, the electrical insulating properties like breakdown voltage becomes significant important. The 11.3-13.3 MV/m breakdown voltage of the wax–BNNS composite exhibits a higher voltage difference threshold compared to that of paraffin wax (6.3–7.3 MV/m) in powering system applications. The application of this high thermal conductivity, large heat absorption capacity and excellent electrically insulating properties of the Wax-BNNS composite can be further extended beyond battery powering systems to microelectronic packaging systems, revealing its remarkable significance for thermal management.

3.3 BN- based Composite in Optoelectronics System

In “Thermally Conductive, Electrical Insulating, Optically Transparent Bi-Layer Nanopaper” paper published at ACS Applied Materials and Interfaces 2016 [51]. W.L., L.Z, and X.H. contributed to BNNS synthesis and material preparation. L.Z. and S.J.

helped with SEM and TEM material characterizations, Z.Y. and B.Y. performed thermal conductivity measurement and temperature distribution measurement. J.D. contributed to 3D figures. Z.Y., W.L. and L.Z. drafted the manuscript. S.J. contributed to grammar check. B.Y. and L.H. contributed the idea and experiments design. All authors contributed the manuscript and comments on the final paper.

3.3.1 Motivation

Flexible optoelectronics are emerging type of electronic technologies due to their great potential to enable a range of new applications such as skin electronics, wearable devices (Figure 3-7), and conformal systems. Ubiquitously, optoelectronics are typically built on a certain type of substrate. Plastic substrate such as cellulose nanofibers (CNF) [51], polyethylene terephthalate (PET) [52], polycarbonate (PC) [53], and polyimide (PI) [54], due to their light weight, flexibility and low cost. Transparent nanopaper made of CNF could potentially be used as innovative substrate to replace some plastics due to its excellent mechanical strength, biodegradability and optical transparency properties, which is extremely attractive for green electronics toward a more sustainable future. Recently, a range of flexible electronics have been demonstrated on transparent paper, including thin film transistors [55], organic solar cells [56], light-emitting diodes, and sensors [57].

Figure 3-7 Wearable Flexible Optoelectronics [58]

However, the poor thermal conductivity of CNF nanopaper will result in local heat concentration as large amount of heat generated in the system, which may lead to thermal failure of the device. Here a bilayer structure of aligned boron nitride nanosheets (BNNSs) coating on transparent CNF-nanopaper was designed. The thin BN layer with high thermal conductivity facilitates in-plane heat dissipation on pure CNF-nanopaper to alleviate heat concentration issue, while still maintains high transparency as compound as shown in Figure 3-8. Compared to mixed design, the bilayer structure leads to heat dissipation mostly at the surface in BN layer. Herein, a thermally conductive, electrically insulating and optically transparent nanopaper was fabricated and experimentally characterized for its application potential [51].

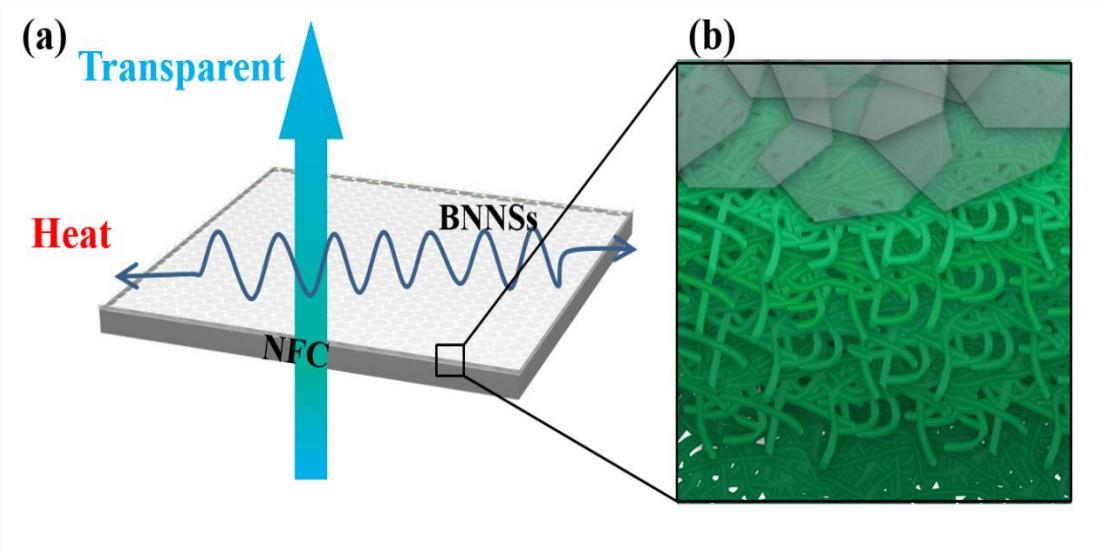

Figure 3-8 Schematic of BN-CNF Nanopaper

(a) Schematic to Illustrate the Transparent Bilayer Nanopaper Conducts Heat along the In-plane Direction. (b) A Detailed Structure of Bilayer Nanopaper

3.3.2 Bilayer BN-CNF Transparent Paper Preparation

The BNNSs suspension was prepared by liquid-exfoliation of the bulk BN in solvent, which makes it possible for scalable production with remarkably stable chemical and thermal properties. The bulk BN in the ethanol/H_2O (9:1 vol. %) in Figure 3-9 (a) could not be well dispersed prior to sonication. As shown in Figure 3-9 (b), BN is comprised of alternating B and N atoms in a "honeycomb" lattice structure, where the in-plane B and N atoms are covalently bounded, but for neighboring cross plane, the BN layers are held via Van der Waals forces. An optimized ethanol/H_2O ratio allows the solvent to penetrate into the interlayer of BN to form favorable interactions with BN molecules. According to previous reports, ethanol/H_2O with 9:1 volume ratio was selected in this work. [59] Also, the solvent effect can weaken the Van der Waals forces between

adjacent BN layers and slowly expands the interlayer spacing, which assists the exfoliation of BN powder and form BNNSs. After 48 h of sonication in the mixed solvent, a white "milky" BNNSs suspension can be obtained (Figure 3-9 (e)), indicating that BNNSs were successfully peeled off (Figure 3-9 (f)). The highly stable suspension showed little precipitation after being stored for 3 weeks under ambient conditions (22 °C, RH 30%).

In order to investigate the morphology and dispersion state of BNNSs, SEM and TEM are introduced. As displayed in Figure 3-9 (c), the bulk BN powder is consisted of flakes with uniform thicknesses and shapes. The lateral sizes of BN flakes ranges from hundreds of nanometer to 1 μm with smooth surfaces (Figure 3-9 (d)). After exfoliation, the lateral sizes of the majority of the BNNSs in the dispersion varied from 200 to 500 nm (Figure 3-9 (g)). However, the thickness decreased significantly that some single BN nanosheets appears extremely thin and transparent (Figure 3-9 (h)).

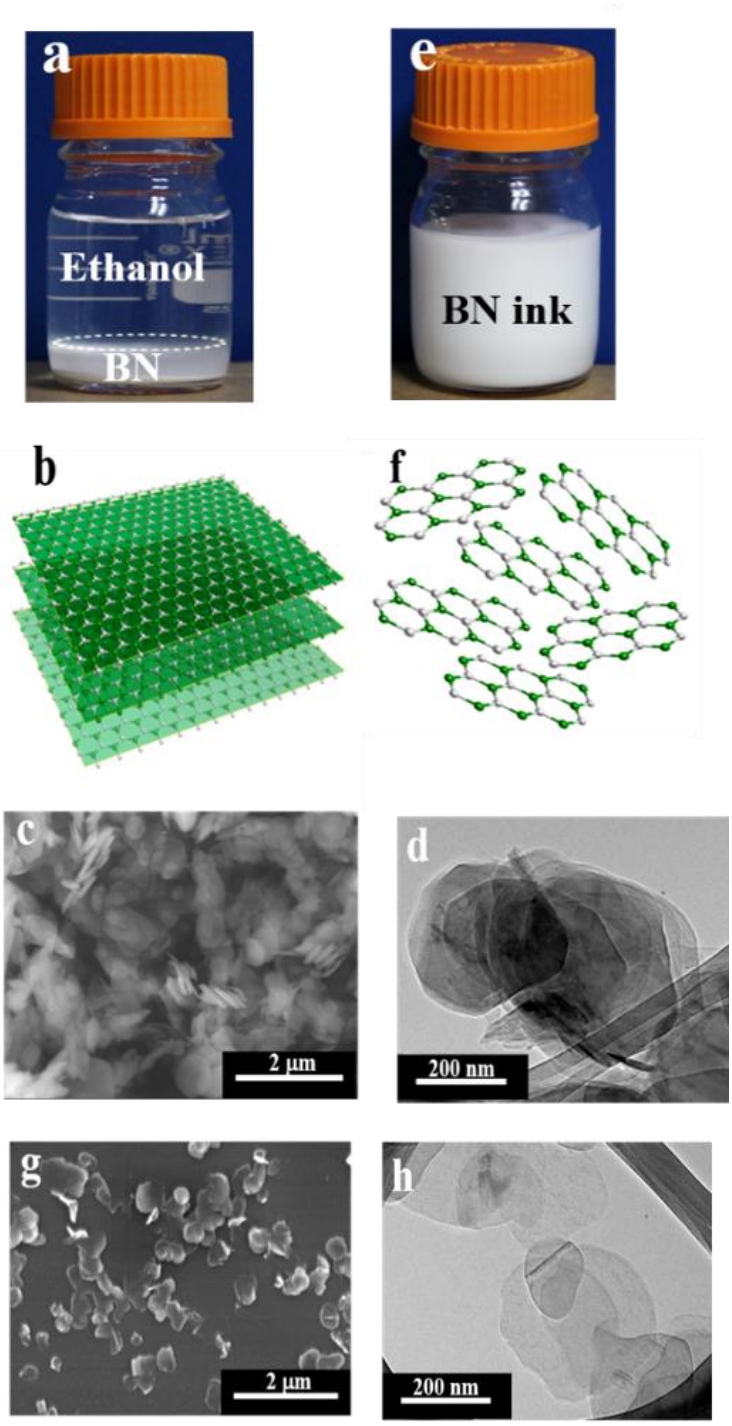

Figure 3-9 SEM Morphology Characterization

(a) Photograph of Pristine BN Powder in Ethanol-H_2O (9:1 vol.%) Mixed Solvent before Sonication, (b) Schematic of Layer Bulk BN, (c) SEM and (d) TEM Images of

Pristine BN Powder before Sonication, (e)BN Ink after 48h of Sonication in Ethanol-H_2O (9:1 vol.%) Mixed Solvent, (f) Schematic of BNNSs Dispersed in Ethanol-H_2O (9:1 vol.%) Mixed Solvent, (g) SEM and (h) TEM Images of BN Nanosheets.

Bilayer nanopaper can be fabricated using the BNNSs solution and CNF solution. Pure nanopaper made from CNF solution was used as a control. Figure 3-10 (a), (b) show SEM images of the cross-section of pure CNF-nanopaper made from cellulose nanofibers with a diameter of 10−20 nm. The cellulose nanofibers tend to self-assemble and form a layered structure with layer-by-layer stacking, which provides CNF nanopaper with good flexibility and transparency. Figure 3-10 (c) shows the cross-section images of the bilayer nanopaper with 2.5 wt. % of BN, where the thickness of BNNSs layer is about 1 μm. When the BN layer is enlarged, BNNSs can be clearly observed (Figure 3-10 (d)). Furthermore, the surface observations by SEM (Figure 3-10 (e), (f)) confirmed that BNNSs are successfully coated onto the surface of CNF-nanopaper.

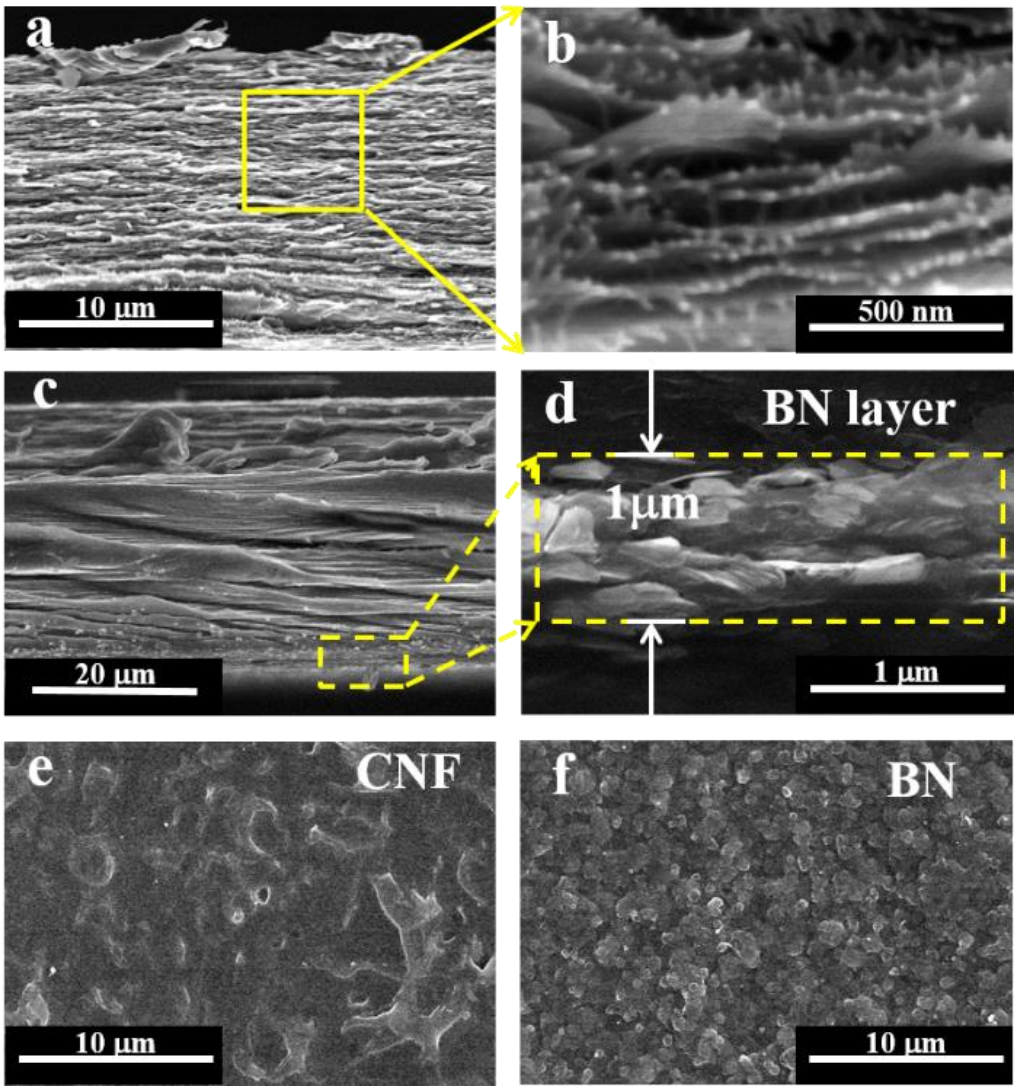

Figure 3-10 SEM Morphology Characterization Before and After BN Coating SEM Images of (a, b) Pure CNF-nanopaper and (c, d) Bilayer Nanopaper. SEM Images of (e) CNF Surface and (f) BN Surface of the Bilayer Nanopaper

3.3.3 Bilayer BN-CNF Transparent Paper Properties Characterization

As discussed above, the most critical properties for BN-CNF nanopaper are transparency and thermal properties. In this section, those properties were experimentally tested and analyzed. The transmittance of CNF and bilayer nanopaper

was analyzed with a Lambda 35 UV− Vis Spectrometer (PerkInElmer, U.S.A.). The bilayer nanopaper with 2.5 wt. % of BN is relatively optical transparent, as shown in Figure 3-11 (a). Optical measurement (Figure 3-11 (b)) of the bilayer nanopaper exhibits 70% transmittance at 550 nm wavelength, which is comparable to that of pure CNF-nanopaper (~94%). The slightly decrease in transparency is due to the thin layer of BN coating on the CNF-nanopaper surface.

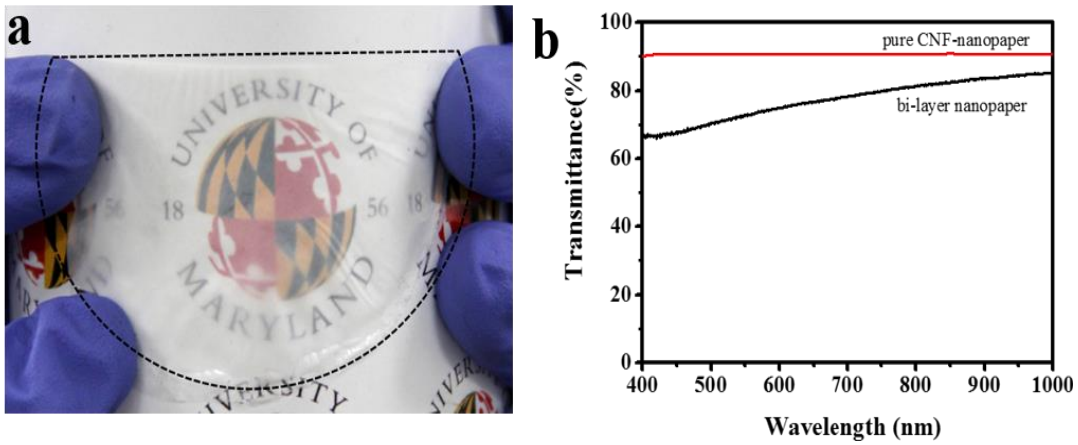

Figure 3-11 Optical Properties Characterization of BN-CNF Nanopaper

(a) Photograph of Bilayer Nanopaper 2.5 wt. % of BN. (b) Transmittance of Pure CNF-nanopaper and Bilayer Nanopaper with 2.5 wt. % of BN

The in-plane thermal conductivity of the pure CNF nanopaper and the bilayer nanopaper were further investigated using a steady-state method. The pure CNF-nanopaper shows a poor thermal conductivity of 0.04 W/mK, which is typical for cellulose-based paper (Figure 3-12 (a)). After covering it with a 1 μm thickness of BNNSs layer, the thermal conductivity of whole bilayer nanopaper increased to 0.76 W/mK, which is about 19 times higher than that of pure CNF-nanopaper. When the

content of BNNSs increased, the in-plane thermal conductivity increased sharply, following a percolation-like behavior. For example, the in-plane thermal conductivity of bilayer nanopaper with 90 wt. % of BN was 30.0 W/mK.

To further investigate the heat transfer performance of the bilayer nanopaper, thermographs were captured by an infrared thermal camera using a laser as the heat source. A Coherent Highlight FAP 1000 laser system has been used as heating source for the specimens to be tested with a wavelength of 810 nm. The resulting temperature distribution along the side surfaces was captured by FLIR Merlin MID Infrared (IR) camera with a resolution of 320 x 256 pixels. The non-uniform temperature distribution revealed poor in-plane thermal conductivity of pure CNF-nanopaper since the heat created by a laser hot spot could not spread out easily, which resulted in a relatively high temperature at the center of the laser hot spot (Figure 3-12 (c)). In contrast, a more uniform temperature distribution can be observed on the bilayer nanopaper (Figure 3-12 (d)). Figure 3-12 (b) shows the temperature distribution of the two samples with respect to the location of the laser pointer. For pure CNF-nanopaper, the temperature starts around 21 °C while it starts around 23 °C for bilayer nanopaper with 2.5 wt % of BN. However, the temperature distribution profile of pure CNF-nanopaper is narrower than that of the bilayer nanopaper, which indicates heat was not distributed well along the pure CNF-nanopaper as compared to that of bilayer nanopaper. The better thermal distribution of the bilayer nanopaper can be contributed to the higher in-plane thermal spreading due to the introduction of highly conductive BNNSs layer.

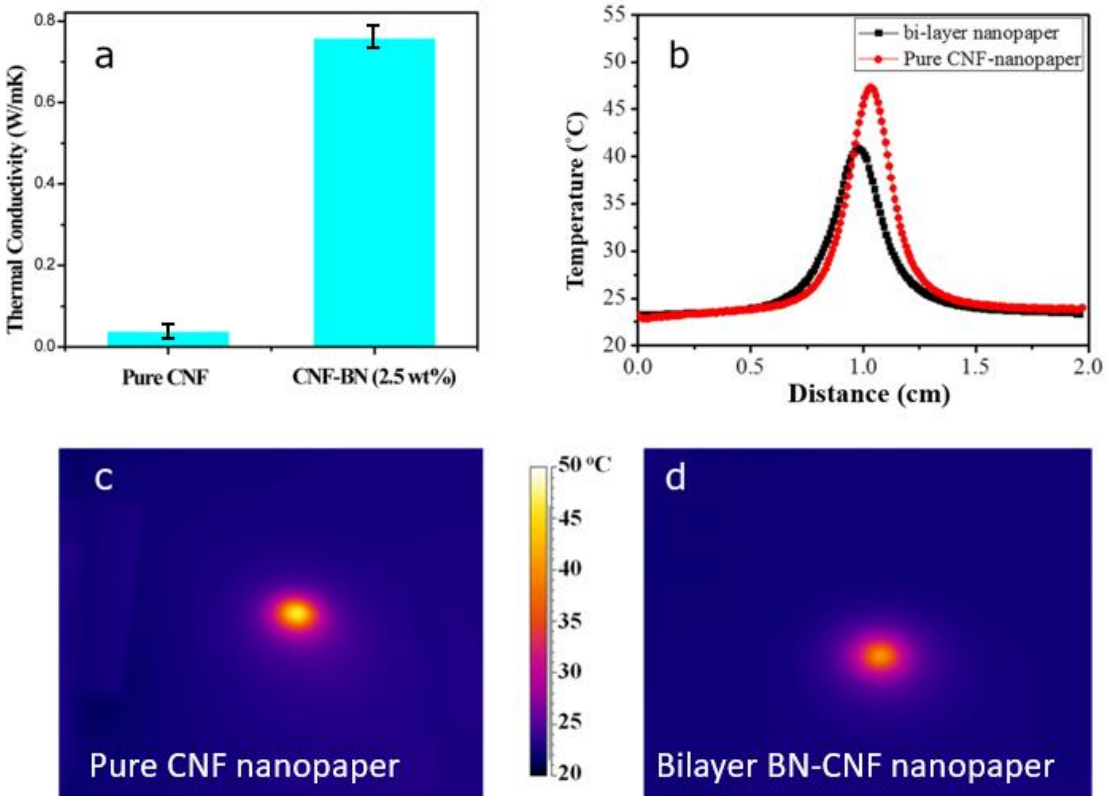

Figure 3-12 Thermal Properties Characterization of BN-CNF Nanopaper (a) Thermal Conductivity of Bilayer Nanopaper with Different Total BN Contents of 0, 2.5 wt. %, respectively. (b) Temperature Distribution of Pure CNF-Nanopaper and Bilayer Nanopaper with 2.5 wt. % of BNNSs. Thermograph of (c) Pure CNF Nanopaper and (d) Bilayer Nanopaper with 2.5 wt. % of BNNSs

3.3.4 Experimental Section

Preparation of BNNSs

BN powder was purchased from Sigma-Aldrich Co., Ltd. (U.S.A.) (particle size: ~1 μm). To prepare a large volume of BNNSs dispersion with good quality, 1.5 g of pristine BN powder was added into 500 mL of ethanol/H_2O mixed solvent (v/v = 9:1 vol. %). The mixed solution was sonicated for 48 h in a water bath (FS 110D, Fisher

Scientific, U.S.A.), and then settled at room temperature for 24 h. Then the top 3/4 of the supernatant was collected, and the concentration of the BNNSs dispersion was measured to be 1.9 mg/mL.

Fabrication of Bilayer Nanopaper with 2.5 wt. % of BN

The CNF was disintegrated from wood pulp based on the method proposed in our previous work. In order to fabricate the bilayer nanopaper, solution A was first prepared by pouring 58.3 g of 1.0 wt. % CNF solution into 400 mL of deionized water under vigorous stirring at room temperature for 30 min. Similarly, solution B was prepared by pouring 1.7 g of 1.0 wt. % CNF solution into 150 mL of deionized water. Second, 8.2 mL BNNSs suspension (1.9 mg/mL) was dropped into solution B during the stirring, which was labeled as solution C. The solution C was continuously stirred for 30 min, followed by sonicating in a water bath for another 30 min to form a uniform BNNSs/CNF suspension. Finally, solution A was filtered with a Bucher funnel using a filter membrane (A DVPP/Cellulose acetate filter membrane of 9 cm in diameter, 0.65 μm pore size, Milipore, U.S.A.). After solution A was drained, the solution C was added carefully to the filter. The as-prepared wet paper was placed between filter papers and followed by heating at 30 °C under mechanical pressing for 2 days, after which the free-standing bilayer nanopaper could easily be peeled from the filter membrane. The total content of BN in the whole free-standing film is about 2.5 wt. %.

Materials Characterization

Scanning electron microscopy (SEM) images were taken on a Hitachi SU-70 Schottky field emission gun scanning electron microscope, while transmission electron microscope (TEM) images were taken from a JEOL 2100 TEM at 200 kV. X-ray diffraction (XRD) patterns were collected with a Bruker D8 Advance using Cu Kα radiation (λ = 1.5406 Å). The transmittance of CNF and bilayer nanopaper was analyzed with a Lambda 35 UV–vis Spectrometer (PerkInElmer, U.S.A.). The thermal conductivity along the BN nanosheets layer on the bilayer nanopaper is measured by applying steady-state method outlined in our previous studies.

3.3.5 Conclusion

In summary, we reported a bilayer transparent paper with aligned BN nanosheets coated on the surface of CNF-nanopaper. The perfect in-plane alignment of the BNNSs on the nanopaper increase the thermal conductivity of nanopaper from 0.04 W/mK to 0.76 W/mK when the BN content increases from 0 wt. % to 2.5 wt. %, while maintaining relative high optical transparency (up to 70%). Higher BN content will dramatically decrease the overall transparency of the compound. The CNF-BN compound with 2.5 wt. % of BNNS content has been experimentally proved to possess significantly improved thermal properties, while still maintain acceptable overall transparency in visible light range. In contrast to well-developed thermally conductive coating with graphene and carbon nanotube, the electrically insulating of BNNS coating is essential for system integrations on transparent and flexible substrates in electronic systems.

3.4 BN- based Composite in Energy Storage System

In “A Thermally Conductive Separator for Stable Li Metal Anodes” paper published at Nano Letters 2015 [60]. W.L, L.Z, K.F designed BN specimen preparation and fabrication, J.W. and Y.Y helped with XRD material characterizations, Z.Y. and M.M. performed thermal conductivity measurement and temperature distribution measurement, H.Z. B.Y. and L.H. contributed the idea and experiments design. W.L. and L.Z. contributed to electrochemical measurement. All authors contributed the manuscript and comments on the final paper.

3.4.1 Motivation

Lithium-ion batteries (LIBs) have been critical for powering portable electronics since their commercialization in early 1990s. To meet the ever-increasing demands of new electric vehicles and electrical energy storage for renewable energy resources, LIBs with high energy density are required. Unfortunately, graphite-based anode employed in current LIB system exhibits a low specific capacity, significantly limiting the energy density of LIBs. Therefore, significant effort has been focused on developing anodes with high specific capacity, such as Si and Li metal. However, issues associated with Li metal anodes, including uncontrollable dendritic Li growth and low Coulombic efficiency upon electrochemical cycling, have impeded their use in practical application. With the urgent demand of high-energy-density batteries, developing safe and stable Li metal anodes has become very pivotal but remains a significant challenge to research scientists [60].

In order to address the issues found in Li metal anodes, many approaches have been explored. To inhibit the dendritic Li growth, some researchers exploited a uniform and stable solid electrolyte interphase (SEI) layer on Li metal surface, which is used to adjust the components and additives of liquid electrolyte. For example, Xu and Zhang reported that $CsPF_6$ additive can effectively enhance the stability of SEI and thus suppress the dendritic Li growth. An alternative approach using solid or gel electrolyte to improve mechanical strength and operational lifetime has also been studied. In addition to the work on electrolyte additives, solid-state electrolytes, and interfacial materials, modifying the separator has also been studied as a method to achieve stable Li metal anodes. In previous research, different ceramic and organic materials were used to coat a commercial separator. Hexagonal boron nitride, also known as "white graphene", is one of the most studied 2D materials due to its chemical stability, electrical insulation, and very high thermal conductivity. In this study, we propose a novel boron nitride (BN) nanosheets coated on commercially available separator (shown in Figure 3-13(a)) for stable Li metal anodes. As shown in Figure 3-13 (b), we hypothesize that a thermally conductive BN coating can result in a uniform deposition/striping of Li due to the smaller total surface area of the initial deposited Li wires and a more homogeneous thermal distribution, decreasing the risk of dendritic Li growth and improving cycling performance.

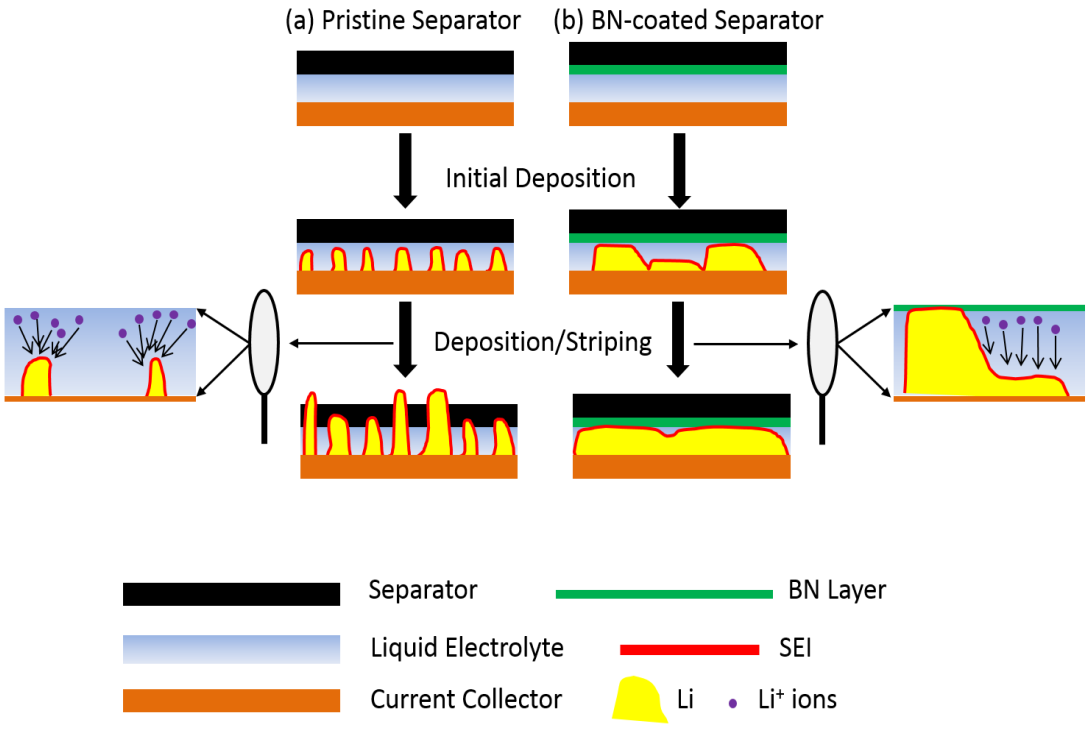

Figure 3-13 Schematic of BN-coated Separator

Schematic of (a) Pristine Separator and (b) BN-coated Separator

3.4.2 BN-coated Separator Material Preparation

BN bulk powder, purchased from Sigma-Aldrich, exhibits a typical hexagonal phase and flake morphology with a size of ~500 nm. BN powder is exfoliated by a sonication procedure using N-methyl pyrrolidone (NMP) as the solvent. After sonication, BN nanosheets are prepared. The typical thickness of BN nanosheets is ~9.0 nm, as determined by AFM. The as prepared BN/PVDF/NMP suspension (Figure 3-14 (a)) is coated onto one side of a commercial separator (Celgard 2325) by vacuum filtration followed by drying in a vacuum oven at 60 °C overnight. As marked by the green circle

in Figure 3-14 (b), the surface of the separator becomes white and less specular after BN coating. As shown in Figure 3-14 (c), a large number of pores are observed in the surface of the pristine separator, and after coating, these pores are covered by BN nanosheets with a particle size of ~500 nm (Figure 3-14 (d)). The thickness of the BN layer is about 1-2 μm with a mass loading of ~0.2 mg/cm^2 (Figure 3-14 (e)), where the electrolyte uptake is slightly increased to 245% for BN-coated separator compared to pristine separator (180%).

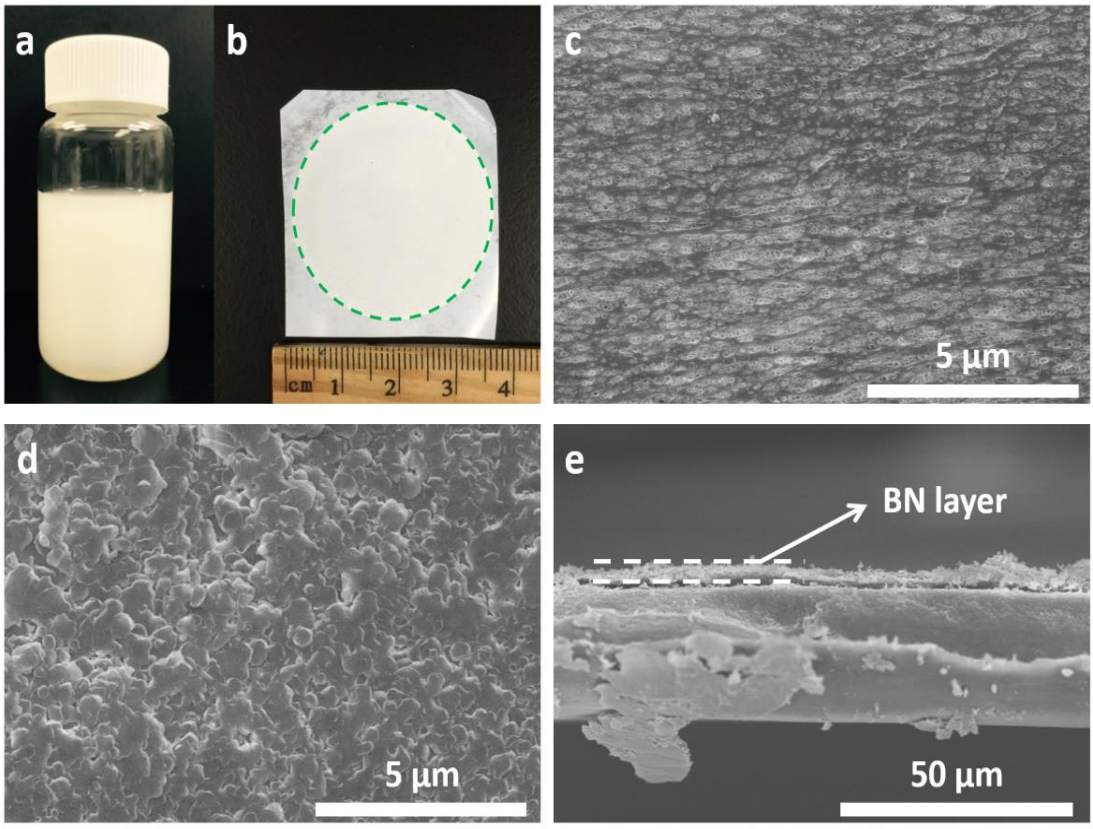

Figure 3-14 Preparation of BN-coated Separator and SEM Morphology Characterization

(a) Digital Images of BN/PVDF/NMP Suspension and (b) BN-coated Separator (BN layer is marked with green dot line). (c) SEM Images of Pristine Separator. (d) Top View and (e) Cross-section View of BN-coated Separator.

3.4.3 BN-coated Separator Properties Characterization

To investigate the electrochemical performance, pristine and BN-coated separator are employed in Li/Cu cells, where Cu foil is used as the working electrode, Li foil as the counter/reference electrode, and 1.0 M $LiPF_6$ in ethylene carbonate/ diethyl carbonate (EC:DEC = 1:1 by volume) solution as the electrolyte. Li deposition/striping cycles between Cu working electrode and Li counter/reference electrode are performed at various current densities. It is known that the morphology of the electrochemical Li deposition plays a critical role in Coulombic efficiency. Coulombic efficiency drops to 85% after 50 cycles and 18% after 100 cycles in the cell with pristine separator. In comparison, a stable Coulombic efficiency of ~92% after 100 cycles can be maintained with BN-coated separator (Figure 3-15 (b)), and a similar result is also observed when the current density is further increased to 1.0 mA/cm^2. The cell with a BN-coated separator shows Coulombic efficiency maintains at 88% after 100 cycles, while the control experiment shows sharp decay trend in Coulombic efficiency. The above observations demonstrate that the cycling performance of the Li metal anode at high current densities is significantly improved by using the BN-coated separator.

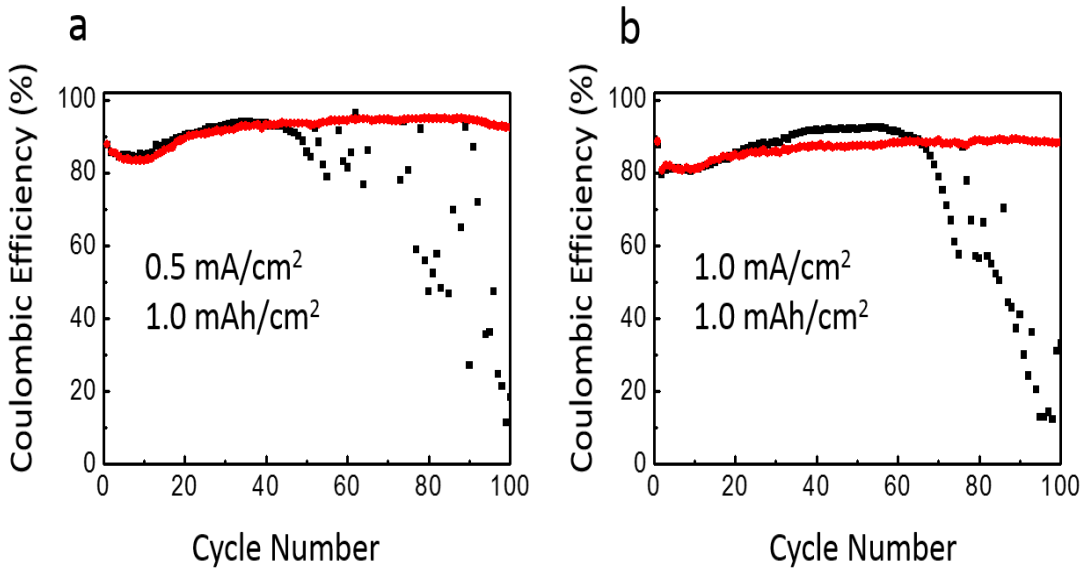

Figure 3-15 Electrochemical Performance Characterization of Li/Cu Cells

Electrochemical Performance of Li/Cu Cells with Pristine Separator (black) and BN-coated Separator (red) at Various Current Densities with a Deposition Capacity of 1.0 mAh/cm^2: (a) 0.5 mA/cm^2 and (b) 1.0 mA/cm^2

To investigate the thermal properties enhancement with BN coating, an infrared camera is used to map the temperature distribution when a hotspot is created on the separators by a focused laser beam. As shown in Figure 3-16 (a), the temperature distribution of the separators was characterized by heating separator center with a laser and measuring the resulting temperature distribution with an infrared camera. The separators were transparent in the IR spectrum, so a graphite coating was applied in order to make IR measurements possible. The graphite coating was applied to the side of the sample with no BN coating and the sample is placed with graphite coating oriented down on the experimental apparatus. The experimental apparatus was made of a low thermal

conductivity polymer to minimize any heat spreading in the fixture. The laser heating was focused down to a 1 mm diameter spot at the center of the separators, resulting in a temperature gradient with the highest temperature at the center and lower temperatures at the periphery. Higher thermal conductivity material allows localized heating to spread more readily; thus, for a given laser power BN-coated separator shows a smaller temperature rise than that of the pristine separator. The temperature spike is about 50 °C at the hotspot in the pristine separator as shown in Figure 3-16 (c). In comparison, the temperature spike is reduced to 34 °C (Figure 3-16 (d)) due to the enhanced heat spreading with the BN nanosheets coating. It can be seen that the BN-coated separator can create a more uniform thermal distribution during Li deposition/striping cycling, which would lead to a more uniform growth/dissolution of Li and thus a better Coulombic efficiency and cycling performance.

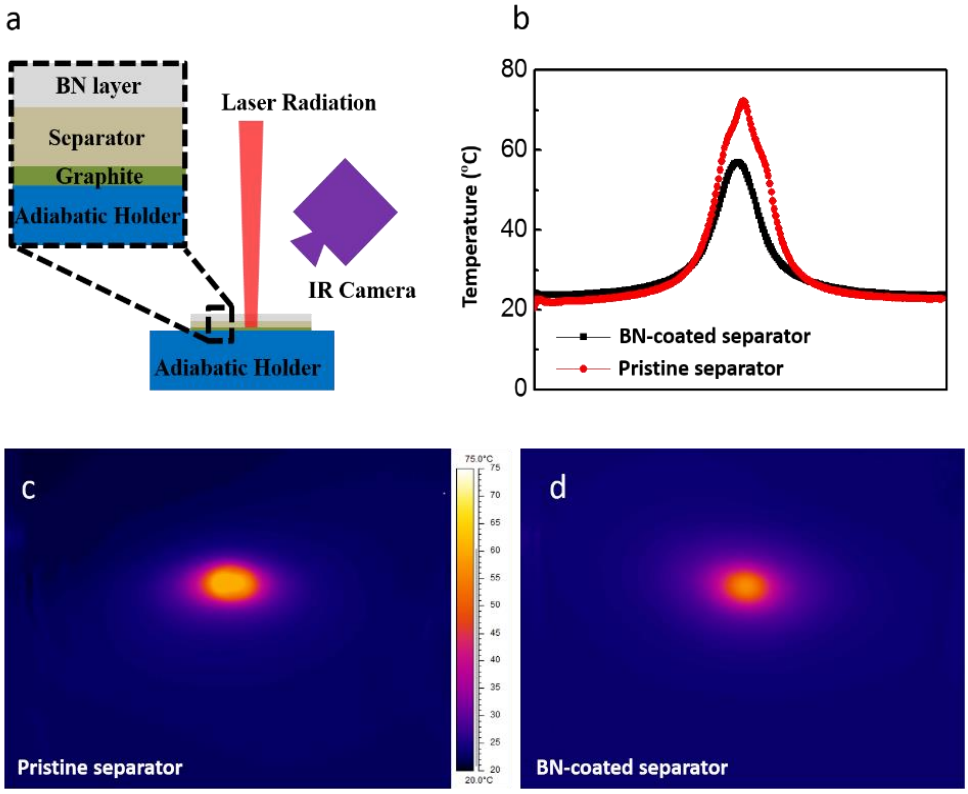

Figure 3-16 Thermal Properties Characterization of BN-coated Separator (a) Schematic Illustration of Mapping the Temperature Distribution when a Hotspot is Created on the Separators by a Focused Laser Beam; (b) Corresponding Temperature Lines on Pristine Separator and BN-coated Separator. (c) and (d) Temperature Distribution Images of Pristine Separator and BN-coated Separator

3.4.4 Experimental Section

Preparation of BN/NMP suspension

BN bulk powder is purchased from Sigma-Aldrich and BN suspension is prepared according to our previous work. First, BN is dispersed in NMP solvent with a concentration of 5.0 mg/mL. Then, the suspension is sonicated for 48 h using a sonic bath (FS 110D, Fisher Scientific), after which, the suspension is centrifuged at 500 rpm

for 10 minutes to remove the bulk powder and give BN nanosheets/NMP suspension with a concentration of ~1.0 mg/mL.

BN-coated separator preparation

PVDF/NMP solution is added into the above BN nanosheet/NMP suspension (mass ratio of BN/PVDF is 9/1) under sonication. The BN/PVDF/NMP suspension is then used to coat one side of a commercial separator (Celgard 2325) with a Bucher funnel and is dried in a vacuum oven at 60 ºC overnight.

Material characterizations

XRD pattern is collected by the D8 Advanced (Bruker AXS, WI, USA) using a Cu Kα radiation source. The morphology is studied via SEM and TEM using Hitachi SU-70 field emission scanning electron microscopy and a JEOL JEM 2100 TEM, respectively. To determine the thickness, BN nanosheets are spin-coated on Si wafers for AFM measurement. AFM data are taken and analyzed by Veeco Multimode AFM with a Nanoscope III controller, 180×180 micron scanner, Nanoscope and Gwyddion software.

Thermal conductivity measurement

The BN coated separator is cut to a small piece that is 6 mm wide and 30 mm long. A heat sink and an electric heater are attached to opposite ends of the BN coated separator and two fine-gage, K-type thermocouples are employed to measure the temperature difference, ΔT across a distance, L, as shown in Scheme S1. To minimize heat loss, the

sample is placed in a vacuum chamber with a heat shield. The temperature and electrical power data are recorded using a NI LabVIEW software. When steady-state is reached, the thermal conductivity of the sample is determined by applying Fourier's law.

Temperature distribution measurement

The temperature distribution of the separators is characterized by heating the center with a laser and measuring the resulting temperature distribution with an infrared camera. A Coherent Highlight FAP 100 laser system, with a central wavelength of 810nm, is used to provide the heating and a FLIR Merlin MID IR camera is used to measure the temperature distribution. The IR camera detects IR radiation at wavelengths from 1 to 5.4 μm, has a sensor resolution of 320 x 256 pixels, and is connected to a computer via ThermaCAM Researcher software. The separators are transparent in the IR spectrum, so a graphite coating is applied in order to make IR measurements possible. The graphite coating is applied to the side of the sample with no BN coating and the sample is placed with graphite coating oriented down on the experimental apparatus. The experimental apparatus is made of a low thermal conductivity polymer to minimize any heat spreading in the fixture. The laser heating is focused down to a 1 mm diameter spot at the center of the separators, resulting in a temperature gradient with the highest temperature at the center and lower temperatures at the periphery. Higher thermal conductivity material allows localized heating to spread more readily; thus, for a given laser power BN-coated separator shows a smaller temperature rise than that of the pristine separator.

Electrochemical measurements

Repeating Li deposition/striping cycles are conducted on an Arbin BT2000 system using 2032-type coin cells with Cu foil as the working electrode and Li metal as the counter/reference electrode.3, 4 LiPF6, ethylene carbonate (EC) and diethyl carbonate (DEC) in battery grade were purchased from BASF Battery Materials. 1.0 M LiPF6 in EC/DEC (volume ratio 1:1) solution is employed as the electrolyte without any additives. The Li deposition capacity is set to be 1.0 mAh/cm^2 and the cut-off potential for striping process is set to be 1.0 V. For morphology observation, after the initial Li deposition, the Cu electrodes were washed with EC/DEC and dried in the antechamber of the glove box prior to SEM characterization.

3.4.5 Conclusion

As demonstrated by Xu and Zhang, a homogeneous electrical atmosphere is very important for uniform Li deposition/ striping. By incorporating BN coating on commercially available separator with poor thermal conductivity (usually less than 0.2 W/mK), a homogeneous thermal atmosphere will be created for uniform Li deposition/striping [61, 62].

An effective approach for improving the cycling stability of Li metal anode via a facile coating of commercial separator with a thermally conductive BN nanosheets was presented. When a deposition capacity of 1.0 mAh/cm^2 is applied in Li/Cu systems

with common organic carbonate electrolyte ($LiPF_6$ in EC-DEC), the Coulombic efficiency can be maintained at 92% after 100 cycles at 0.5 mA/cm^2 and 88% after 100 cycles at 1.0 mA/cm^2 using BN-coated separator, while the Coulombic efficiency decays rapidly using a pristine separator at the same conditions. Considering that Li metal anodes are very promising for high-energy-density batteries, the concept of using a thermally conductive separator can shed light on further research.

3.5 BN- based Composite in Extreme High Temperature System

In "High Temperature Thermal Management with Boron Nitride Nanosheets" paper published at Nanoscale 2017 [63]. L. H. and Y. W. designed the experiments; Y. W., L.X., H.X., Z.Y., W.L., and Y.Y. performed the experiments, P.J. and R.Y. performed thermal conductivity measurement; Y.W., L.X., Z.Y., P.J., and L.H. analyzed the data; Y.W., P.J., J.D., and L.H. prepared the manuscript draft while all authors contributed to editing the manuscript. Y.W., L.X. and Z.Y. contributed equally to this work.

The rapid development of high power density devices leads to extreme high temperature devices, which require more efficient heat dissipation as well as performance reliability under such high temperature working conditions. Recently, two-dimensional layered materials have attracted significant interest due to their superior thermal conductivity, ease of production and chemical stability. Among them, hexagonal boron nitride (h-BN) is electrically insulating, making it a promising thermal management material to be used in next-generation electronics, where extreme high

temperature cannot be avoided. In this work, we demonstrated that an h-BN thin film composed of layer-by-layer laminated h-BN nanosheets can effectively enhance the lateral heat dissipation on the substrate. We found that by using the BN-coated glass instead of bare glass as the substrate, the highest operating temperature of a reduced graphene oxide (RGO) based device could increase from 700 to 1000 ºC. At the same input power, the operating temperature of the RGO device with BN-glass substrate is effectively decreased, prolonging the life-span of such devices. The remarkable performance improvement using the BN coating originates from its anisotropic thermal conductivity: a high in-plane thermal conductivity of 14 W/mK for spreading and a low cross-plane thermal conductivity of 0.4 W/mK to avoid a hot spot right underneath the device. Our results provide an effective approach to improve the heat dissipation in extreme high temperature devices.

3.5.1 Motivation

With the scaling down of device dimensions of integrated circuits and high power electronics, extreme high temperature device has become one of the most critical challenges in device performance and reliability even with small power input at the magnitude of ~ W. If the temperature exceeds the normal operating range, the performance of the device will be degraded and the device may even fail. Therefore, heat spreading ability of the substrate hosting the devices becomes critical. The heat spreading capability of a material directly depends on its thermal conductivity. At room temperature the thermal conductivities of materials most commonly used in high temperature electronics ranges from 0.2 W/mK for polymers to ~2000 W/mK for

synthetic diamond. Recently, two-dimensional materials, such as graphene and hexagonal boron nitride (h-BN) have attracted significant attention due to their remarkable thermal conductivity, making them promising as thermal management materials. The in-plane thermal conductivity of single-layer graphene at room temperature is in a range of 2000-5000 W/mK, which is the highest among the known materials. Even under various engineering configurations, the thermal conductivity of few-layer graphene is still much better than the commonly used materials, such as copper and silicon, which have thus attracted a lot of interests. However, graphene is electrically conductive, and it cannot be used as the thermal management material directly beneath the devices.

Although h-BN has a hexagonal honeycomb lattice structure similar to graphene, it is electrically insulating with a large band gap of 5.8 eV. The calculated in-plane thermal conductivity for h-BN can reach 2000 W/mK. The bulk h-BN is reported to have an in-plane thermal conductivity of as high as 390 W/mK at room temperature, which is close to that of copper. The in-plane thermal conductivity of few-layer h-BN nanosheets is in a range of 100-360 W/mK at room temperature approaching that reported for bulk h-BN. In contrast, the room temperature cross-plane thermal conductivity of bulk h-BN is around 5.2 W/mK, indicating the highly anisotropic thermal conductivity properties of h-BN. The reason underlying such low cross plane thermal conductivity may due to phonon scattering induced by numerous layer interfaces within the bulk h-BN. Furthermore, h-BN has many additional advantages such as high thermal stability (1000□ºC in air, and 1400 ºC in vacuum) and chemical and oxidation resistance. These

desired features make the h-BN one of the most promising thermal management materials for next-generation extreme high temperature electronics applications. However, the industrially relevant application of mass produced h-BN nanosheets, as well as the thermal conductivity of laminated h-BN thin films, have been rarely explored.

In this work, we demonstrate that an h-BN thin film that is composed of layer-by-layer laminated h-BN nanosheets can significantly enhance the lateral heat spreading of the substrate and increase the operating temperature of a device on the substrate for extreme high temperature applications. Mass production of h-BN nanosheets was achieved by sonication-assisted liquid-phase exfoliation of h-BN bulk flakes. The h-BN thin film was coated on a cover glass by the spray-coating technique using a well-dispersed ink of h-BN nanosheets. Two identical electronic devices based on the reduced graphene oxide (RGO) were fabricated, one on bare cover glass (Glass) and another on an h-BN thin film coated cover glass (BN/Glass), for comparison. A current was passed through the RGO device, generating heat that was dissipated into the substrate. For the RGO device on Glass, the highest operating temperature was 700 ºC followed by the melting/cracking of the glass. For the RGO device on BN/Glass, no obvious damage was observed at the operating temperature of 700 ºC, and the highest operating temperature reached 1000 ºC followed by the melting of the glass. At the same operating temperature, the temperature distribution profile of BN/Glass is wider than that of Glass; at equal input power to the devices, the maximum local temperature of the RGO device on BN/Glass is lower than that of the RGO device on Glass. The

unique features of the high in-plane thermal conductivity of 14 W/mK for spreading and low cross-plane thermal conductivity of 0.4 W/mK to avoid local heat accumulation of h-BN thin film enable the improved thermal management performance and overall reliability of BN/Glass.

3.5.2 Preparation and Characterization of h-BN Thin Film

When manufacturing integrated circuits and high power devices, a substrate is needed not only to host the devices but also to spread the heat generated by the devices, which is vital for the thermal management of electronic devices. In general, heat can spread laterally along the surface of the substrate and vertically into the substrate, as shown in Figure 3-17 (a). When the substrate has a low thermal conductivity (such as glass), hot spots where the local temperature is much higher than that of the surrounding area, are produced, causing performance degradation and even failure of the devices.

The h-BN is thermally conductive and electrically insulating, making it an ideal substrate. However, large-scale preparation of single crystal h-BN is difficult and expensive, and the formed h-BN substrate is incompatible with industrial fabrication. An h-BN thin film coated on a substrate, as shown in Figure 30b, could greatly enhance the lateral heat spreading and reduce the occurrence of hot spots on the substrate. Figure 30c shows a schematic of the h-BN thin film comprising thousands of layer-by-layer laminated h-BN nanosheets. The h-BN thin film is expected to have a high in-plane thermal conductivity because of the intrinsically high in-plane thermal conductivity of the h-BN nanosheets; meanwhile, the h-BN thin film is also expected to have a low

cross-plane thermal conductivity because of the layered structure of the h-BN nanosheets bonded by weak van der Waals force. The low cross-plane thermal conductivity of the h-BN thin film can further prevent local overheating of the substrate directly underneath the device.

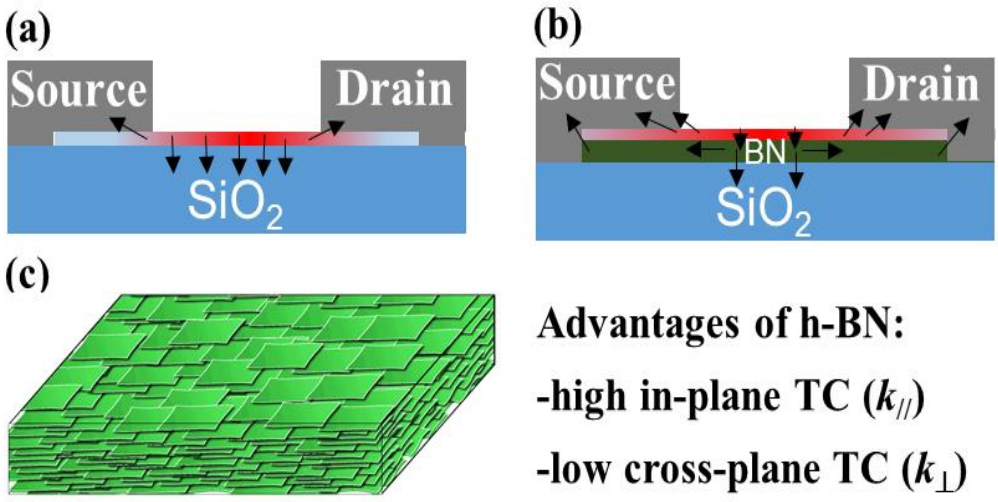

Figure 3-17 Schematic of BN-coated Glass

Schematic Demonstrating the Working Principle of an h-BN Thin Film as an Effective Thermal Management Material. Schematic of a Heat Generating Device on (a) A Bare Glass Substrate and on (b) An h-BN Thin Film Coated Glass Substrate. (c) Schematic of an h-BN Thin Film Comprising Layer-by-layer Laminated h-BN Nanosheets

The h-BN nanosheets were produced by sonication-assisted liquid-phase exfoliation of bulk h-BN flakes in powder (left panel in Figure 3-18 (a)). Excess h-BN powder flakes at an initial concentration of 3 mg/mL were put in isopropyl alcohol (IPA) and sonicated for 10 hours, and then a centrifugation procedure (3000 rpm, 15min) was

performed, yielding a white, dilute, and saturated suspension (h-BN ink) dispersed with h-BN nanosheets (right panel in Figure 3-18 (a)). Figure 3-18 (b) shows a scanning electron microscopy (SEM) image of individual h-BN powder flakes, which have an average lateral dimension of 50 μm and thickness of 5 μm. During sonication, the bulk h-BN flakes are exfoliated into small pieces and becoming h-BN nanosheets. Figure 31c shows a transmission electron microscopy (TEM) image of a single h-BN nanosheet. The h-BN nanosheets have an average lateral dimension of 1 μm and thickness of 20 nm. The h-BN thin film was produced by the spray-coating technique 45 using an ink of dispersed h-BN nanosheets. Figure 3-18 (d) shows a schematic of the spray-coating setup. The h-BN ink was vaporized by a spray gun using N_2 as a carrier gas. After the IPA vapor containing h-BN nanosheets reached the pre-heated cover glass, the IPA had evaporated and the h-BN nanosheets adhered to the cover glass to form the coated h-BN thin film. The thickness of the h-BN thin film can be controlled by adjusting the spray-coating time and/or the concentration of the h-BN ink. Figure 3-18 (e) shows an optical image of the cover glass partially coated with the h-BN thin film (~300 nm thickness). The h-BN thin film is white, and the region of the cover glass covered by the h-BN thin film becomes less transparent. Figure 3-18 (f) shows a top-view SEM image of the h-BN thin film, where the h-BN nanosheets are randomly oriented in the plane and stacked together to form a laminated layer-by-layer structure.

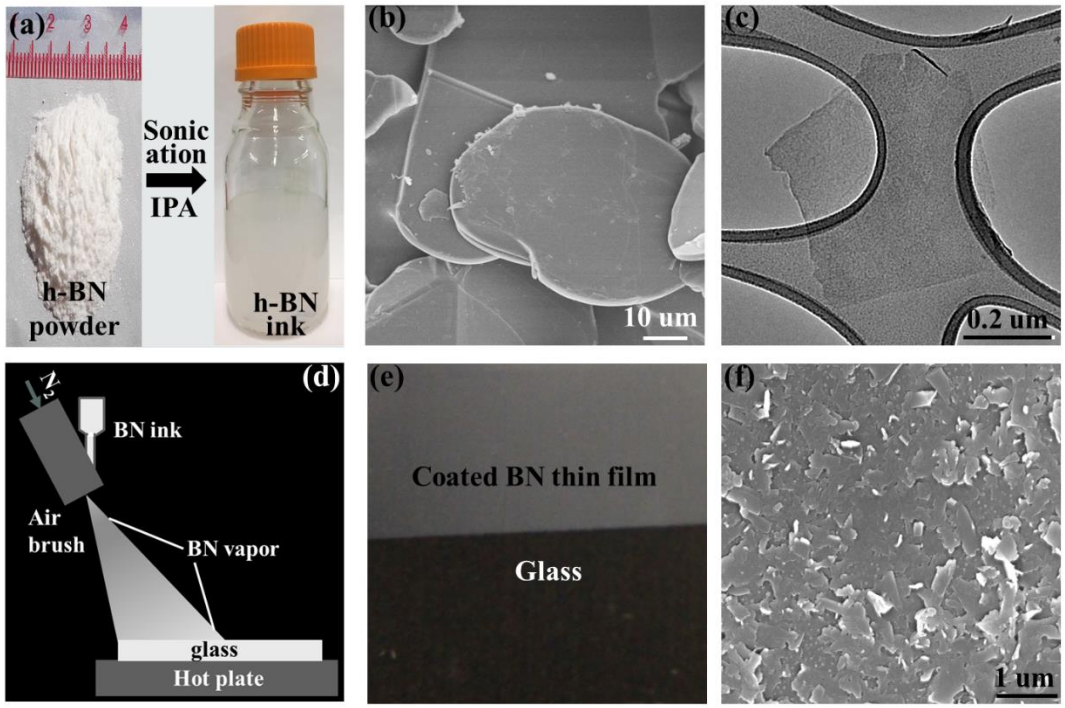

Figure 3-18 Preparation of BN-coated Glass and Morphology Characterization

The Preparation and Characterization of h-BN Nanosheets and h-BN Thin Film. (a) Sonication-assisted Liquid-phase Exfoliation of Bulk h-BN Powder Flakes to Produce h-BN Nanosheets, Yielding a White, Dilute Saturated Suspension (h-BN ink). (b) SEM Image of the Individual h-BN Powder Flakes. (c) TEM Image of a Single h-BN Nanosheet. The h-BN Nanosheets Have an Average Lateral Dimension of 1 μm and Thickness of 20 nm. (d) Schematic of a Spray-coating Setup to produce the h-BN Thin Film on the Cover Glass. (e) Optical Image of the Cover Glass Partially Covered with the h-BN Thin Film (~300 nm). (f) Top-view SEM Image of the Surface of the h-BN Thin Film. The h-BN Nanosheets Are Randomly Oriented in the Plane and Stacked Together to Form the Laminated Layer-by-layer Structure

3.5.3 Improved Thermal Management with h-BN Thin Film Coated Substrate

To demonstrate the thermal management capabilities of the h-BN thin film, two identical devices based on a reduced graphene oxide (RGO) thin film were fabricated, one on Glass and another on BN/Glass, for comparison. Figure 3-19 (a) shows an optical image of the electronic device, where source and drain electrodes are made of silver paste. First, a graphene oxide (GO) thin film (50 nm) was prepared on each substrate by using the same spray-coating technique with a GO dispersion prepared by an improved Hummer's method. The insulating GO thin film was then thermally reduced at 300 ºC in vacuum to remove the oxygen-containing functional groups, leading to a conductive reduced graphene oxide (RGO) thin film. The RGO device is used herein as an example of high power devices due to its high operating temperature. When the RGO device is in operation, current passes through the RGO thin film. According to the Joule's law, heat generated by a conductor at given current and time can be expressed as: Figure 3-19 (b) shows an optical image of the RGO device at an operating temperature of ~650 ºC, where the RGO device shines red light at such a high temperature. The RGO device on Glass suddenly fails at an operating temperature of ~700 ºC. Figure 32c shows an optical image of the failed RGO device on Glass, where the RGO device is broken. The Glass underneath the RGO thin film melted and cracked near the RGO thin film. This is consistent with the fact that glass usually melts at a temperature of >600 ºC. The occurrence of cracks in Glass indicates the existence of hot spots in the regions of Glass underneath the RGO device. Because of the breakdown of the Glass substrate, the RGO device failed at ~700 ºC.

The power was applied to the RGO device using a Keithley 2400 SourceMeter at a constant current mode. The operating temperature of the RGO device was measured by a fiber-coupled spectrometer (Ocean Optics. Inc), which records the emission spectrum. The spectrum was fitted to Planck's law of black-body radiation: $I_\lambda(\lambda,T)=\frac{2hc^2}{\lambda^5}\frac{1}{e^{\frac{hc}{\lambda k_B T}}-1}$ where I(ν,T) is the measured intensity; h, c, k_B, λ and T are the Planck constant, speed of light in a vacuum, Boltzmann constant, wavelength, and absolute temperature, respectively. The measured spectrum fits well with the Planck's law.

The RGO device on BN/Glass was tested in the same way. Figure 3-19 (d) shows an optical image of the RGO device on BN/Glass after testing at ~700 ºC and holding for 30 minutes, where no obvious damage was observed. These results indicate that the BN/Glass substrate can support the power device stably, with normal operation at ~700 ºC. As the input power continuously increases, the RGO device on BN/Glass reaches an operating temperature as high as 1000 ºC before it fails. Figure 3-19 (e) shows an optical image of the failed RGO device on BN/Glass, where the glass underneath the h-BN thin film melted. The melted region extends out farther than that of Glass shown in Figure 3-19 (c), indicating the effect of the high in-plane thermal conductivity of the h-BN thin film. Figure 3-19 (f) shows that the highest operating temperature of the RGO device on BN/Glass increases by 300 ºC compared to that of the RGO device on Glass. The improved performance is attributed to the high in-plane and low cross-plane thermal conductivities of the h-BN thin film. The high in-plane thermal conductivity is

helpful for spreading the heat away from the device, while the low cross-plane thermal conductivity reduces the heat loading to the glass substrate underneath the RGO device, together preventing the crack and melting of the glass.

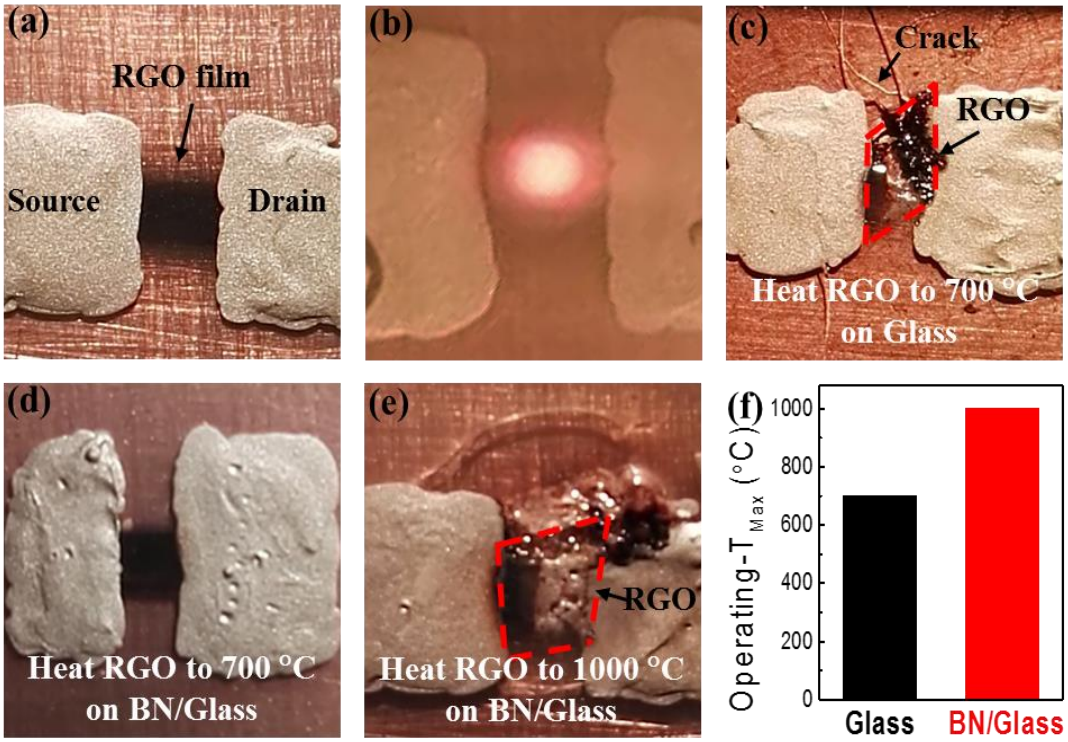

Figure 3-19 Thermal Properties Characterization of BN-coated Glass Comparison of the Thermal Management Performances of Glass and BN/Glass using an RGO Thin Film Based Device. (a) An Optical Image of the RGO Device on Glass. (b) An Optical Image of the RGO Device Heated to ~650 ºC. (c) An Optical Image of the Failed RGO Device on Glass after Heating to ~700 ºC. The Glass Substrate underneath the RGO Device Is Melt and Cracked. (d) An Optical Image of the RGO Device on BN/Glass after Heating to ~700 ºC and Holding for 30 minutes. (e) An Optical Image of the RGO Device on BN/Glass after Heating to 1000 ºC. The

underneath Glass Is Melted and the Melting Region Extends to a Greater Area than the Glass Sample. (f) Comparison of the Highest Operating Temperatures for RGO Devices on Glass and BN/Glass

To directly compare the heat dissipation performance of the Glass and the BN/Glass substrates, thermographs were captured by FLIR T450sc infrared camera. For the temperature distribution profile measurement using an infrared camera, both the RGO devices and the infrared camera were placed in an Argon gas glove box to avoid infrared absorption of glass if the infrared camera is placed outside the glove box. The RGO devices on Glass and BN/Glass are used as local heat sources. Figure 33a shows the temperature distributions on Glass and BN/Glass while keeping a maximum temperature of ~450 ºC at the center for both devices. The temperature distribution profile of Glass is narrower than that of the BN/Glass, indicating more effective heat spreading in BN/Glass. Furthermore, the local temperatures of the RGO devices on Glass and BN/Glass at the equal input power were also measured by the infrared camera, as shown in Figure 3-20 (b). With lower input power, no obvious maximum temperature difference was observed for the RGO devices on Glass and BN/Glass; both of them exhibit local maximum temperature lower than 350 ºC. As the input power to the RGO devices increases, the maximum local temperature of the RGO device on BN/Glass is always lower than that of the RGO device on Glass. For example, with an input power of 2.5 W to the RGO devices, the maximum local temperatures of the RGO devices on Glass and BN/Glass are 649.3 ºC and 574 ºC, respectively, indicating the

heat dispassion performance of the substrate could be effectively improved by coating an h-BN thin film.

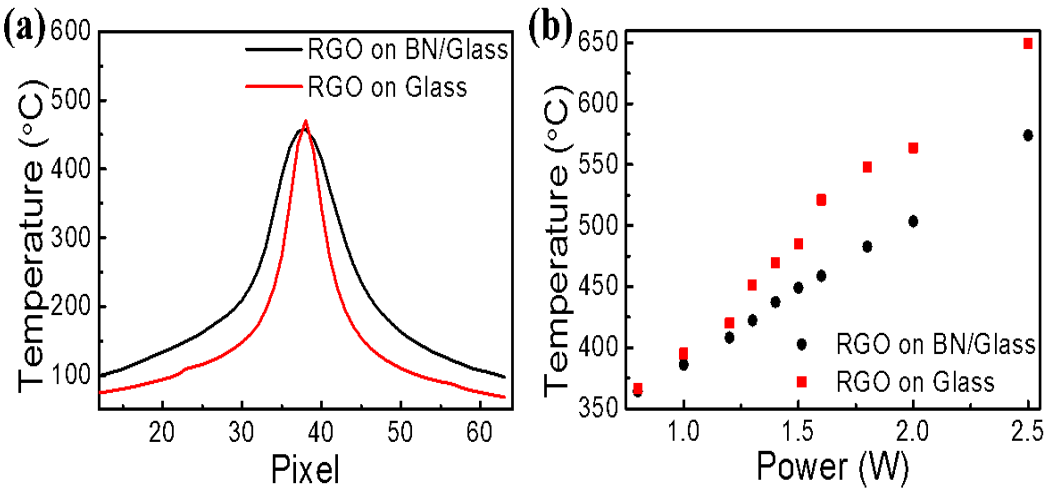

Figure 3-20 Temperature Contour Comparison between Pure Glass and BN-coated Glass

Comparison of Temperature Gradient Distribution and Power Dependent Temperature for the RGO Devices on Glass and BN/Glass. a) Temperature Gradient Distribution Profiles of the RGO Devices on Glass and BN/Glass While Keeping A Maximum Local Temperature of ~450 ºC. The Temperature Gradient of BN/Glass Is Wider Compared to That of Glass. b) Relationship between Input Power and Maximum Local Temperatures of the RGO Devices on Glass and BN/Glass. At the Same Input Power, the Maximum Local Temperature of the RGO Device on BN/Glass Is Lower Than That of the RGO Device on Glass

3.5.4 In-Plane and Cross-Plane Thermal Conductivities of h-BN Thin Film

The improved thermal performance of the BN/Glass benefits from high in-plane thermal conductivity and low cross-plane thermal conductivity of the h-BN thin film. A time-domain thermoreflectance (TDTR) with a variable laser spot size approach was used to measure both the in-plane and the cross-plane thermal conductivities of the h-BN thin film. A schematic of our TDTR setup is shown in Figure 3-22 (a). The thermal conductivity of the h-BN film was measured by time-domain thermoreflectance (TDTR) at room temperature. In this method, a Ti:sapphire laser generates a train of femtosecond laser pulses at a repetition rate of 81 MHz with a wavelength centered at 785 nm. The laser output is split into a high-energy pump beam and a low-energy probe beam using a polarized beam splitter. The pump beam is further modulated at a frequency between 0.5 to 10 MHz using an electro-optic modulator (EOM) and then directed onto the sample to induce a small heating event. The probe beam is delayed temporally with respect to the pump via a 600-mm-long mechanical delay stage and then directed onto the sample to interrogate the surface temperature change as a function of the delay time. The measured data were compared to a thermal model calculation, from which we extracted the unknown thermal conductivities of the substrate.

To prepare the samples for TDTR measurements, we first deposited a 100-nm-thick Al film on a smooth glass slide, followed by a ~ 5-μm-thick h-BN film spray coated on the Al film. We then performed the pump-probe experiments from the glass side. The 5-μm-thick h-BN film could be considered as bulk in our TDTR measurements, as the

thermal penetration depth in h-BN in the cross-plane direction, which is defined as $d_p = \sqrt{k_\perp / \pi f C}$, with f the modulation frequency and C the volumetric heat capacity, is only in the range of 90 – 400 nm in our experiments, much shorter than the film thickness. The 100-nm-thick Al film serves as a transducer for the TDTR experiments. By depositing the transducer film on a smooth glass slide instead of directly on the rough h-BN film, we can achieve a smooth surface for the transducer that enables specular reflection of the probe beam, which is critical for TDTR measurements. The TDTR signal is predominantly sensitive to the cross-plane thermal conductivity when using a large laser spot size for the measurement, where the heat flow is mainly one-dimensional along the cross-plane direction. On the other hand, the TDTR signal is sensitive to both the cross-plane and the in-plane thermal conductivities when using a tightly focused laser spot for the measurement, where the heat flow becomes three-dimensional. Thus, both the cross-plane and the in-plane thermal conductivities of the h-BN thin film can be determined by conducting two sets of measurements using different laser spot sizes (Figure 3-22 (b)). As shown in Figure 3-22 (c), the in-plane and cross-plane thermal conductivities of the h-BN thin film are fitted to be $k_{//} = 14 \pm 5$ W/mK and $k_\perp = 0.4 \pm 0.15$ W/mK, respectively. The in-plane thermal conductivity of the h-BN thin film is much higher compared to the thermal conductivity of bare glass, which is $k = 1.3 \pm 0.2$ W/mK, while the cross-plane thermal conductivity of the h-BN thin film is lower than bare glass. The in-plane thermal conductivity of h-BN film is much smaller than that of single piece of few layer h-BN nanosheets, and can be further improved by increasing the lateral size of h-BN nanosheets laminated in the h-BN film.

The thicker h-BN film thickness better benefits the thermal management performance, as evidenced by a simulation shown in Figure 3-21.

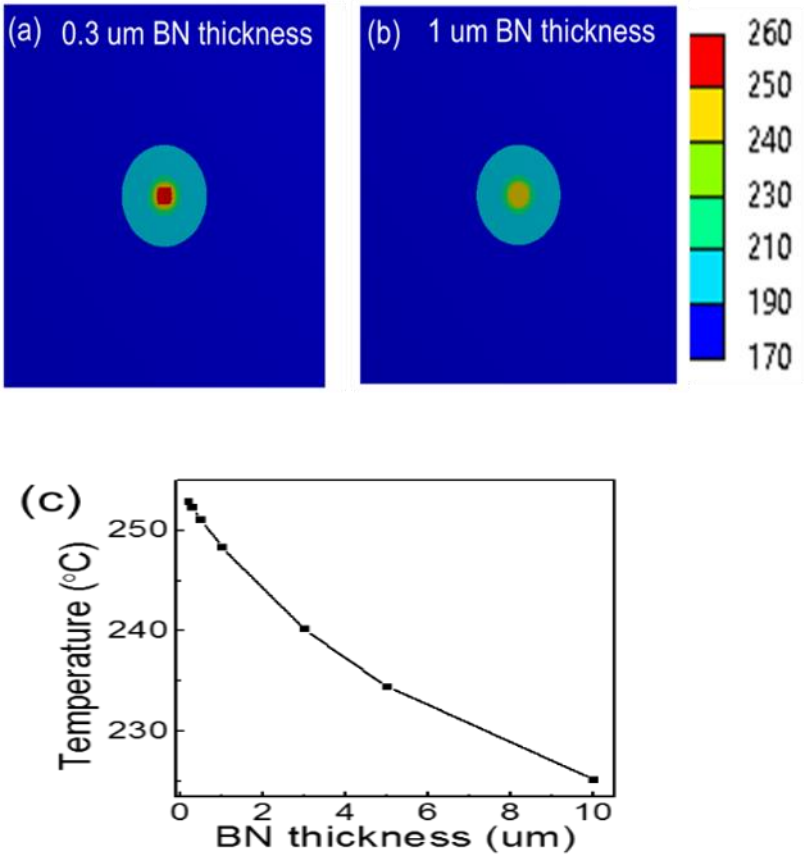

Figure 3-21 Effect of BN Coating Thickness on Maximum Temperature on Substrate (a-b) Temperature Distribution on A BN/glass Composite under the Same Local Heat Source for (a) 0.3 μm BN Thickness and (b) 1μm BN Thickness. (c) The Maximum Temperature of the Glass Substrate underneath the Same Local Heat As A Function of the BN Thickness

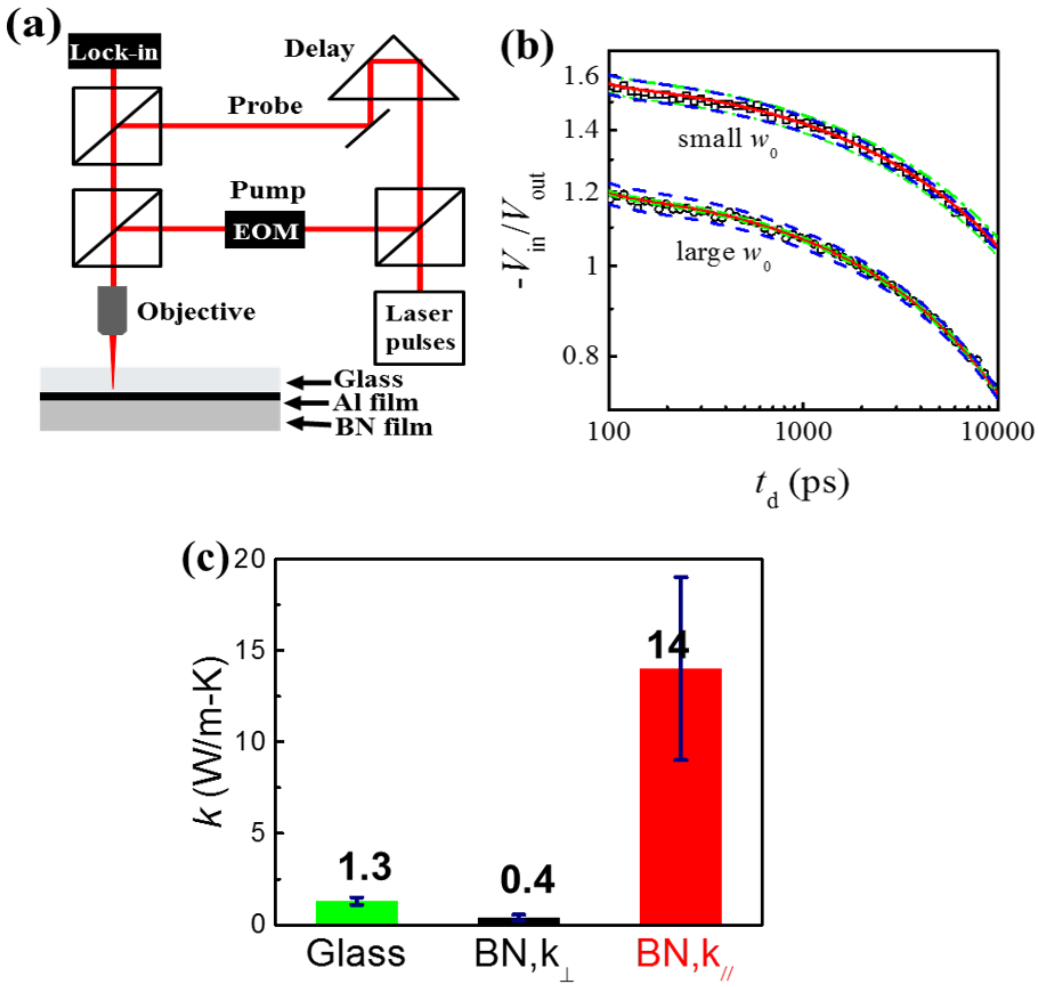

Figure 3-22 BN Optical and Thermal Properties Characterization

Anisotropic Thermal Conductivity of the h-BN Thin Film. (a) A Schematic of the Experimental Setup (TDTR) and the Sample Geometry for Thermal Conductivity Measurements of the h-BN Thin Film. (b) TDTR Experimental Data on the h-BN Thin Film (symbols) along with the Fittings from A Thermal Model (solid, red lines) and 30% Bounds on the Fitted Values of the Cross-plane (dash, blue lines) and the In-plane (dash-dot, green lines) Thermal Conductivities, Measured Using Different

Laser Spot Sizes. (c) Comparison of the In-plane and Cross-plane Thermal Conductivities of the h-BN Thin Film and That of the Glass.

3.5.5 Experimental Section

Operation of the RGO device on Glass and BN/Glass

The power was applied to the RGO device using a Keithley 2400 SourceMeter at a constant current mode. The operating temperature of the RGO device was measured by a fiber-coupled spectrometer (Ocean Optics. Inc.), which records the emission spectrum. The spectrum was fitted to Planck's law of black-body radiation (Equation 24), where I(ν, T) is the measured intensity; h, c, kB, λ and T are the Planck constant, speed of light in a vacuum, Boltzmann constant, wavelength, and absolute temperature, respectively. The measured spectrum fits well with the Planck's law.

$$I_{\lambda}(\lambda,T)=\frac{2hc^{2}}{\lambda^{5}}\frac{1}{e^{\frac{hc}{\lambda k_{B}T}}-1} \tag{24}$$

Temperature Distribution Measurement by the Infrared Camera

For the temperature distribution profile measurement using an infrared camera, both the RGO devices and the infrared camera were placed in an Ar glove box to avoid infrared absorption of glass if the infrared camera is placed outside the glove box. The FLIR T450sc infrared camera has a spectral range between 7.5–13 μm with a resolution of 320 × 240 pixels.

Thermal Conductivity Measurements

The thermal conductivity of the h-BN film was measured by time-domain thermoreflectance (TDTR) at room temperature. In this method, a Ti:sapphire laser generates a train of femtosecond laser pulses at a repetition rate of 81 MHz with a wavelength centered at 785 nm. The laser output is split into a high-energy pump beam and a low-energy probe beam using a polarized beam splitter. The pump beam is further modulated at a frequency between 0.5 to 10 MHz using an electro-optic modulator (EOM) and then directed onto the sample to induce a small heating event. The probe beam is delayed temporally with respect to the pump via a 600 mm-long mechanical delay stage and then directed onto the sample to interrogate the surface temperature change as a function of the delay time. The measured data were compared to a thermal model calculation, from which we extracted the unknown thermal conductivities of the substrate.

To prepare the samples for TDTR measurements, we first deposited a 100 nm-thick Al film on a smooth glass slide, followed by a ~5-μm-thick h-BN film spray coated on the Al film. We then performed the pump–probe experiments from the glass side. The 5 μm-thick h-BN film could be considered as bulk in our TDTR measurements, as the thermal penetration depth in h-BN in the cross-plane direction, which is defined in Equation 25, with f the modulation frequency and C the volumetric heat capacity, is only in the range of 90–400 nm in our experiments, much shorter than the film thickness. The 100 nm-thick Al film serves as a transducer for the TDTR experiments. By depositing the transducer film on a smooth glass slide instead of directly on the

rough h-BN film, we can achieve a smooth surface for the transducer that enables specular reflection of the probe beam, which is critical for TDTR measurements.

$$d_p = \sqrt{k_\perp / \pi f C} \tag{25}$$

3.5.6 Conclusion

We demonstrated that a coated BN thin film effectively improves the thermal management capability of the substrate. Comparing the operation of RGO devices on BN/Glass and Glass, the operating temperature of the RGO device on BN/Glass is much lower than that of the RGO device on Glass at the same input power, and the maximum operating temperature of the RGO device on BN/Glass is increased from 700 ºC (for RGO device on Glass) to 1000 ºC. The improved performance of the BN/Glass is due to the high in-plane ($k_{\parallel} = 14 \pm 5$ W/mK) and the low cross-plane ($k_\perp = 0.4 \pm 0.15$ W/mK) thermal conductivities of the BN thin film, which leads to fast heat dispassion along the BN surface and helps to block the heat transfer to the substrate directly underneath the device. This work not only provides an effective approach to resolving heat dispassion issues in integrated circuits and high power density devices, but is also helpful for other thermal management applications.

3.6 Summary

In this chapter, the hexagonal boron nitride nanosheets are introduced as highly thermally conductive filler into different base materials to enhance the composite overall effective thermal performance for electronic systems. The BNNSs large lateral

flakes inside the composite can form a continuous network for better heat dissipation from the local hot spot. Compared to other thermally conductive materials, such as graphene, CNTs, unique electrical insulating properties of BNNSs prove their promising potential to be used in electronic systems as thermal management material.

The thermal conductivity measurement, DSC and IR tests of BN based materials are performed for material thermal properties characterization. Several different electronic system applications that incorporating BNNSs are discussed, which are experimentally validated the benefits of BNNSs in improving the system's overall performance and reliability by alleviating overheating thermal issues. The sharp contrast between BN incorporated materials and pristine base material further indicates the crucial role of BN in the thermal management system in electronics. By applying additives has been proved to be an effective way to tail material properties based on different application requirements.

Chapter 4 Material Properties Modification with External Magnetic Field

4.1 Introduction

In previous chapter, we have engineered material properties using nanostructured material boron nitride to enhance overall device/ system level performance and reliability. Here another commonly used approach to modify material properties by introducing external magnetic field, will be discussed.

Magnetic field applications are very common in daily life, such as magnetic field generated by electrical current inside transformers, hard disk read/ write function using giant magnetoresistive (GMR) material, hospital magnetic resonance image (MRI), super-conducting magnetic field in particle accelerator applications [64-66]. For some systems, certain active components need to be isolated/ shielded from magnetic field for better performance, higher reliability and data integrity. For instances, certain measuring sensors needs to be isolated from magnetic field to ensure reliable readings, computer hard disk requires minimum exposure to strong magnetic field to protect data integrity from magnetic irreversible damage *etc*.[67]. However, on the other side, for certain magnetic responsive materials, such as magnetoresistance materials and magnetocaloric materials, the existence of external magnetic field is the foundation for their desired properties, offering new application potentials. Therefore, how the magnetic field will affect material properties, how to apply magnetic field in favor of better performance, higher reliability and how to understand the underlying working

principles still remains to be further unveiled. In this section, the detailed design/ optimization of magnetic field distribution, thermal management performance evaluation, construction of magnetic field wire housing assembly and effect of magnetic field on material properties will be discussed.

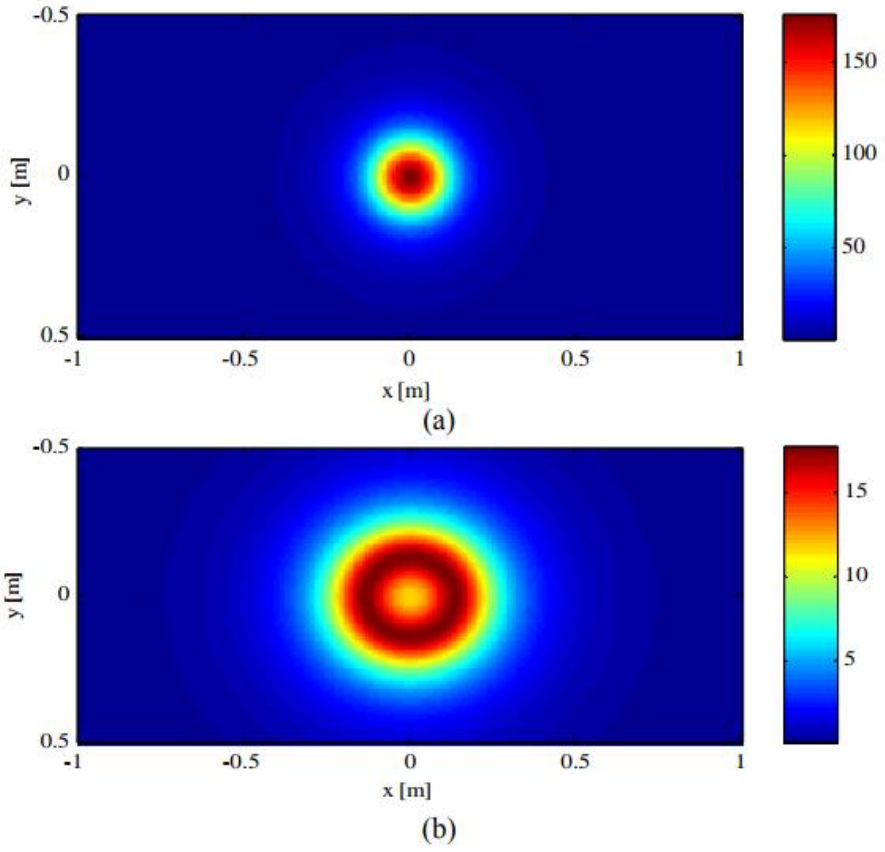

Figure 4-1 Magnetic Field Shielding

B-map [μT] at Distance of 0.1 m from Secondary Coil. (a) Without Shielding. (b) With Magnetic Shielding [67]

4.2 Magnetic Field Distribution Design and Optimization

To investigate the effect of magnetic field on material properties, a magnetic field needs to be numerically optimized for desired distribution and experimentally constructed for distribution characterization. Apart from magnetic field generated by superconducting material at extremely low temperatures (generally below 100 K) and permanent magnet, numerous researchers have been focusing on optimizing the current-carrying pattern of magnetic field due to its versatility and ease manufacturability. The most commonly used approach is to embed current-carry element followed by designed pattern on a straight cylinder tube surface. Based on theoretical mathematic calculation for a desired magnetic field distribution using target field approach, the current-carrying pattern can be obtained. Recently emerging technique using boundary element method (BEM) allows to design current-carrying pattern on complex surfaces [68]. While *et al* presented an analytic inverse method for theoretical design for gradient coil system by precisely locate current-carrying coil windings on predetermined straight cylinder surface [69]. Vaughan *et al.* reported a high magnetic field benchmark of 9.4 T using a 65 cm diameter bore magnet with an asymmetric gradient coil and shim set. In their approach, a 45 cm diameter hollow cylindrical tube was used as the housing for current-carrying element [70].

With the concept of the slanted surface incorporation to cylindrical shape, 3D model of the magnetic field wire housing was built in Solidworks 2016. The maximum dimension of X layer is 54 cm in diameter including slanted surface. And the total X layer height is around 39 cm as shown in Figure 4-2. The copper wire will be embedded

into outer surface of the magnetic field wire housing part followed by precisely calculated pattern. Similar to X layer pattern design, Y layer pattern is shown below as well. Current-carrying element of Z layer follows the solenoid pattern.

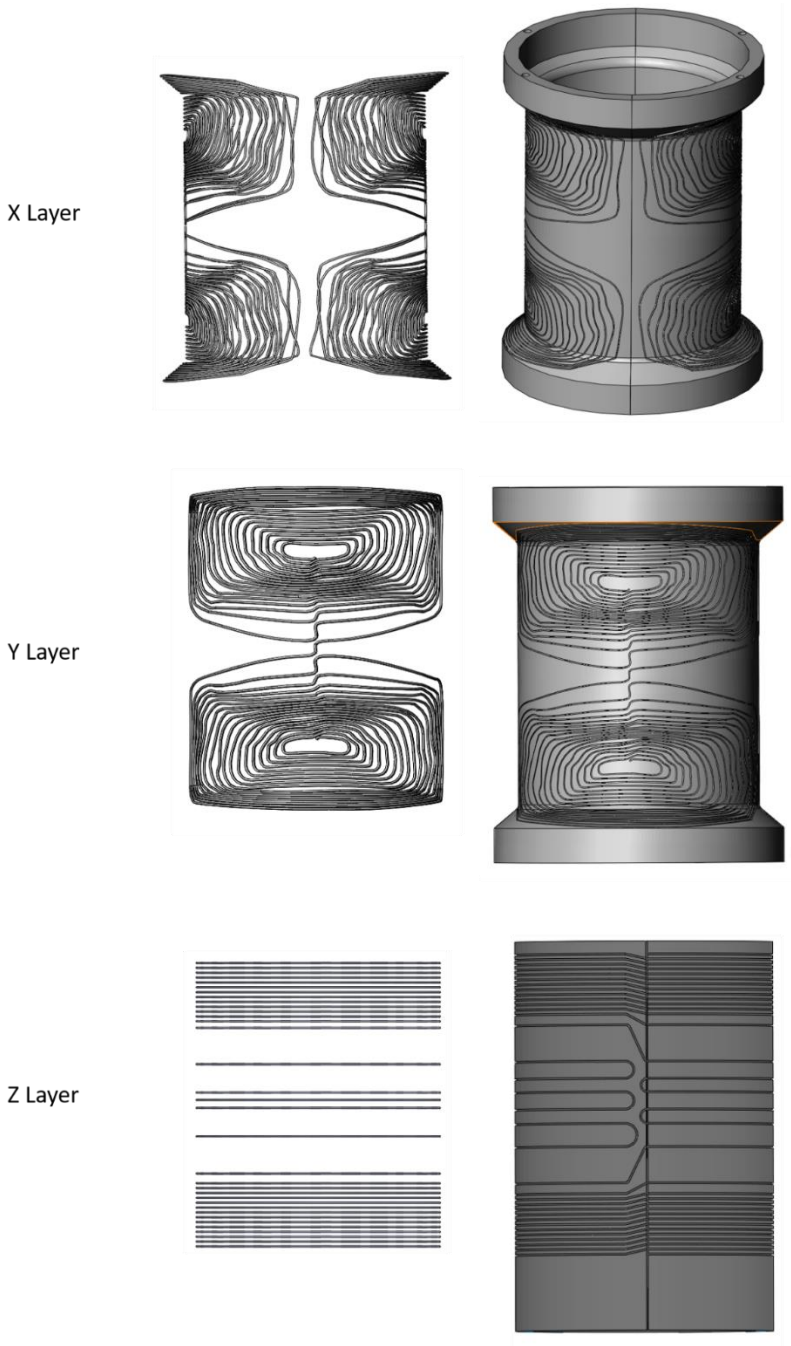

Figure 4-2 X, Y and Z Layer Current-Carrying Pattern and Overall Assembly Model

To manufacture magnetic field housing with such complicated current-carrying element pattern can be extremely challenging for conventional machining techniques for example computer numerical control (CNC), especially for patterns on slanted surface. The sparse availability and long learning curve for such sophisticated machinery operation also poses limitations in its implementation. Fortunately, the emerging innovative additive manufacturing 3D printing offers perfect solution for such complicated geometry. Therefore, 3D printing technique will be applied for magnetic field wire housing construction.

Magnetic Field Distribution Numerical Simulation

Once the current-carrying pattern for X, Y and Z layer is finalized using target field approach, a numerical simulation on magnetic field distribution was performed in ANSYS Electronic Desktop Maxwell V18.1 finite element software. The current-carrying element was set to AWG 12/10 copper alloy to mimic the actual application condition. The excitations, *i.e.* current input values to copper wires, was varied to evaluate the overall magnetic field distribution and strength information. Due to the current-carrying element geometry complexity, one continuous current-carrying element path was simplified to discrete patterns for a closed loop magnetic field simulation. Figure 4-3 shows X, Y and Z Layer magnetic field spatial distribution at 100 Amp Excitation.

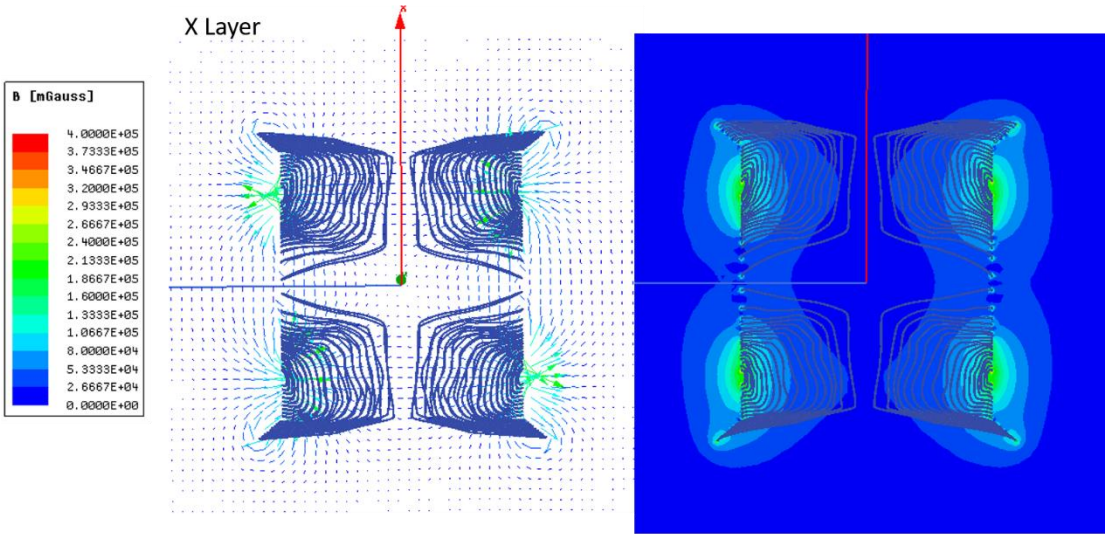
X Layer
B [mGauss]
4.0000E+05
3.7333E+05
3.4667E+05
3.2000E+05
2.9333E+05
2.6667E+05
2.4000E+05
2.1333E+05
1.8667E+05
1.6000E+05
1.3333E+05
1.0667E+05
8.0000E+04
5.3333E+04
2.6667E+04
0.0000E+00

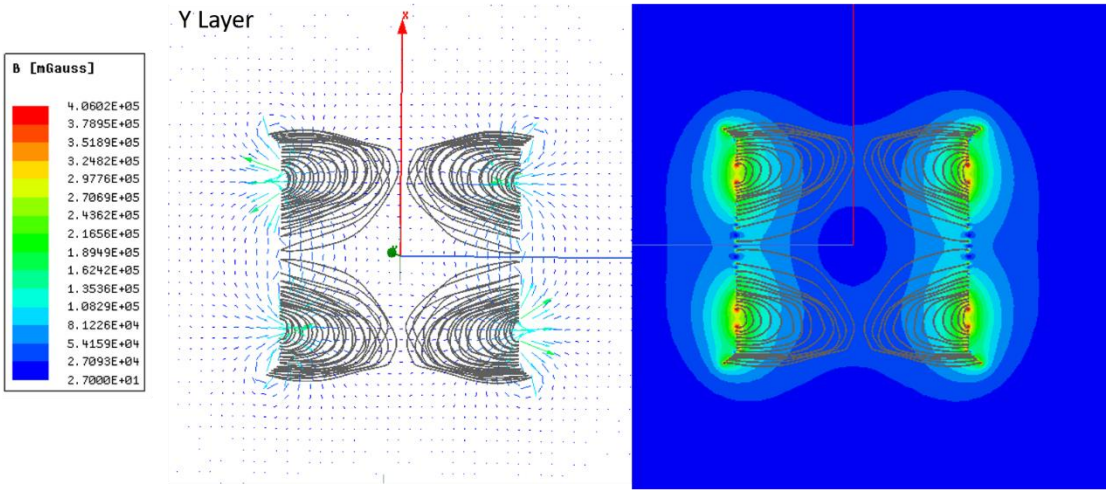
Y Layer
B [mGauss]
4.0602E+05
3.7895E+05
3.5189E+05
3.2482E+05
2.9776E+05
2.7069E+05
2.4362E+05
2.1656E+05
1.8949E+05
1.6242E+05
1.3536E+05
1.0829E+05
8.1226E+04
5.4159E+04
2.7093E+04
2.7000E+01

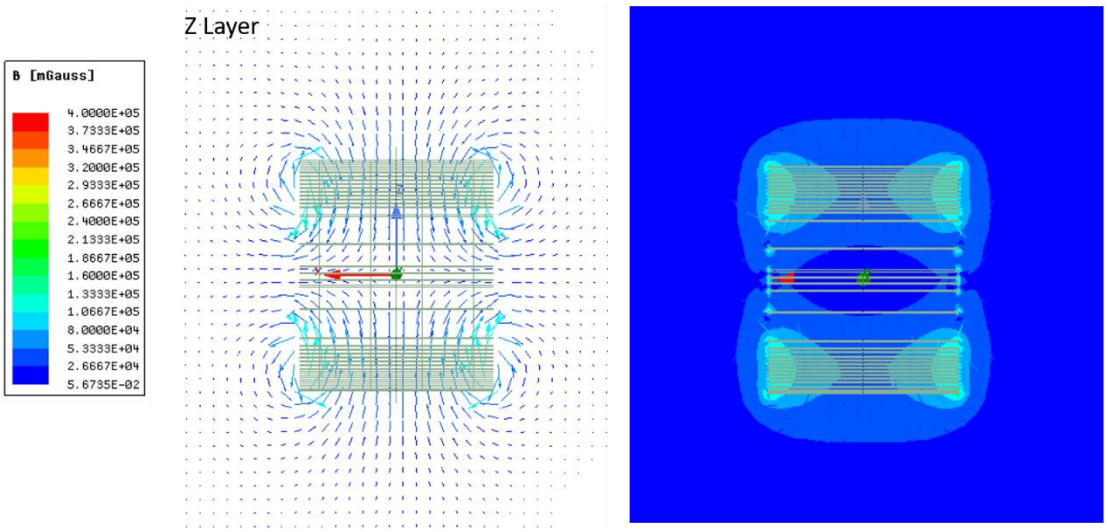
Z Layer
B [mGauss]
4.0000E+05
3.7333E+05
3.4667E+05
3.2000E+05
2.9333E+05
2.6667E+05
2.4000E+05
2.1333E+05
1.8667E+05
1.6000E+05
1.3333E+05
1.0667E+05
8.0000E+04
5.3333E+04
2.6667E+04
5.6735E-02

Figure 4-3 X, Y and Z Layer Magnetic Field Spatial Distribution at 100 Amp Excitation

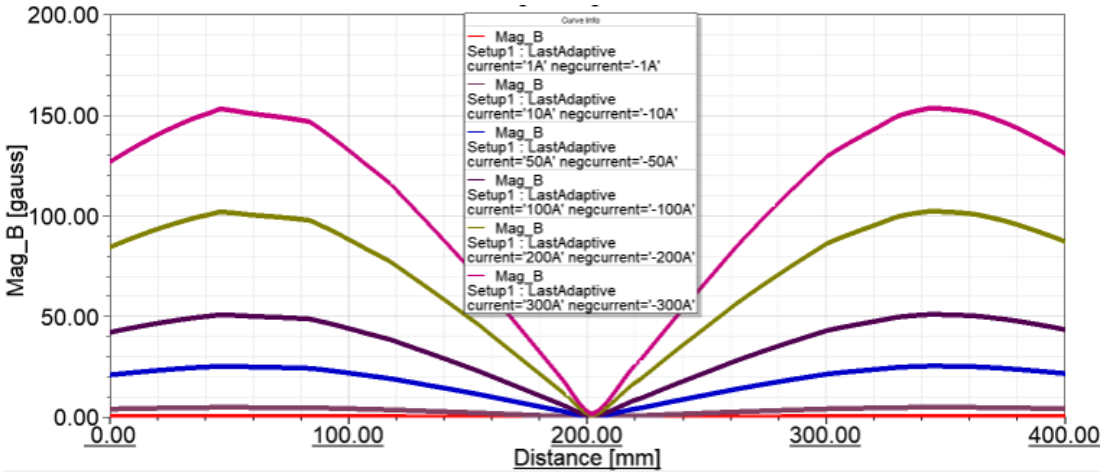

Figure 4-4 Centerline Linearity Evaluation of Z Layer Magnetic Field Distribution at Various Excitation Conditions

From the magnetic field distribution from Figure 4-3, it can be easily seen that a symmetric "butterfly" shape with good homogeneity symmetric distribution has been achieved. With carefully calculated excitation input, the overall magnetic field strength can be modified to satisfy each application requirement. The middle non-magnetic field region offers magnetic field shielding effect. The highest magnetic field strength occurs near the current-carrying element, which agrees well with the Biot-Savart Law. The detailed mathematic explanation can be found in Equation (26). With such magnetic field design for X, Y and Z layer, within the magnetic field domain, each coordinate corresponds to a unique magnetic field vector, which offers ultimate versatility for exploration of the magnetic field.

$$B(r) = \frac{\mu_0}{4\pi} \int_C \frac{I \cdot d\vec{l} \times \vec{r}}{\left|\vec{r}\right|^2} \tag{26}$$

Another important parameter besides linearity along centerline in evaluating the magnetic field is its magnetic field strength. Stronger magnetic field enables more versatile application exploration. Figure 4-4 shows the centerline magnetic field distribution. The maximum magnetic field strength increases proportionally with higher excitation, thus the distribution curve yields steeper slope.

4.3 Magnetic Field Wire Housing Cooling Numerical Simulation

It is well known, for conventional current-carrying element, for example copper wires, the magnetic field B has linear relationship with electrical current, while the Ohmic/Joule heating is proportional to the square of current in the circuit. In the cases where a few hundred amperes are required, insufficient thermal management system can be bottleneck of entire design, compromising system overall performance. In recent studies, many of the researchers are limited to relative low current, for example less than 60 Amp limited by the overheating issue in the system. Handler *et al* proposed a 30 Amp current through the wire patterns with forced water cooling of copper tube next to the magnetic wire housing layer with epoxy as insulation layer in between [68].

To provide uniform cooling performance for the current-carrying element, the number of cooling channels and coolant distribution need to be optimized. Uniform coolant distribution among all the cooling channels is the key to homogeneous cooling

performance. For mal-distributed coolant, the channels without sufficient coolant flow rate may not able to remedy overheating crisis, which compromises the performance of entire system. One practical way to ensure evenly coolant distribution is to increase pressure difference ratio between cooling channel and distribution header. If the pressure drop in distribution header is negligible compared to that in cooling channels, the flow will experience no impedance in the header, leading to a uniform distribution.

4.3.1 Coolant Flow Distribution Optimization

It is important to ensure that the coolant enters each channel is enough flow rate to maintain the maximum temperature below safety threshold. In that case, the flow distribution from the header to each individual channel becomes very important. Without proper design of the coolant distribution header, the coolant will rush into the channel near the header inlet and outlet. While for those cooling channels locating far away from the distribution inlet and outlet, insufficient flow will cause poor cooling performance, which leads to local overheating risk.

Distribution header design for uniform coolant distribution has been optimized. The schematic of flow distribution modeling is shown in Figure 4-5, where the blue domain indicates the coolant flow domain in the header and cooling channels; the blue and red marks the location of inlet and outlet in distribution header. In order to compare the effect of different header dimensions on overall flow distribution, the simulation was performed in ANSYS ICEPAK module with the Duratherm 450 oil as coolant. The

volumetric flow rate, pressure drop and velocity distribution in each individual channel were compared and analyzed by parametrizing flow distribution header thickness.

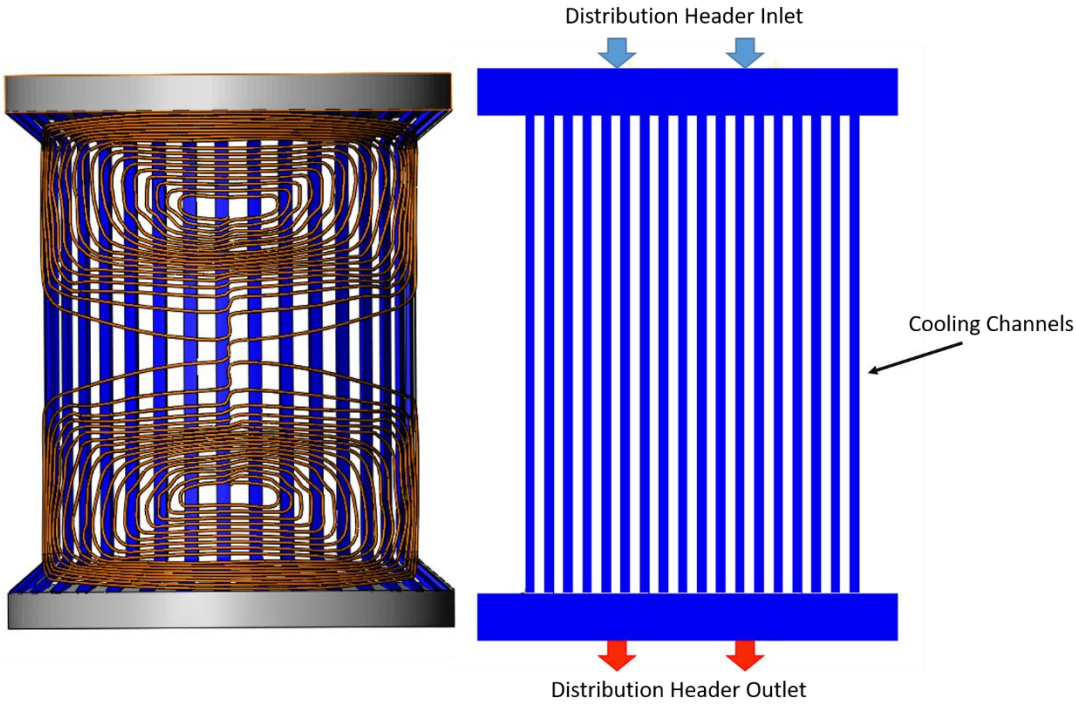

Figure 4-5 Schematic of Flow Distribution Header and Cooling Channels

(Orange color: copper wire, blue color: cooling channel)

The Figure 4-6 shows the pressure contour of coolant distribution with 5 mm and 50 mm header. From the result, it can be seen that the 50 mm header provides enough space for the flow to be well distributed prior to entering each channel. For the 50 mm header, not only overall pressure drop is lower compared to the thinner header, but also the pressure distribution of each channel is more uniform. Figure 4-7 presents the velocity vector plot of flow distribution in coolant channels for different header thickness. For the 5 mm header design, the inlet is close to certain cooling channels,

which results in more coolant flows through those channels. The flow velocity in such channels is obviously higher than that in other channels. However, for 50 mm header case, before the coolant enters the cooling channel, the inlet flow is already well spread in the thick header, it doesn't make a noticeable difference for cooling channel's location respect to the distribution header inlet and outlet. That yields evenly distributed flow in the cooling channels.

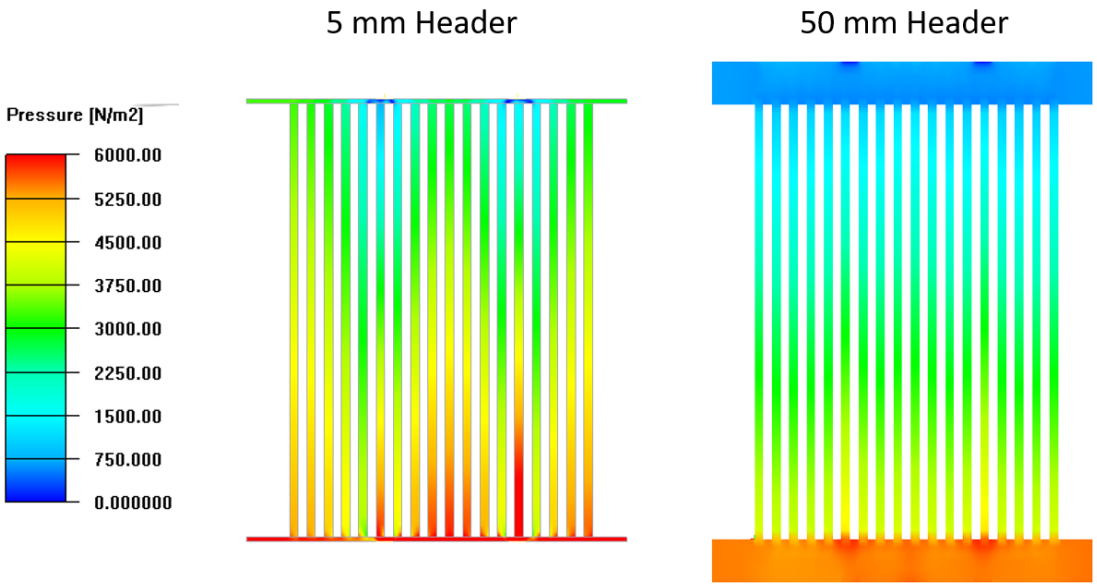

Figure 4-6 Pressure Distribution Contour of the Cooling Channel with Different Header Thickness

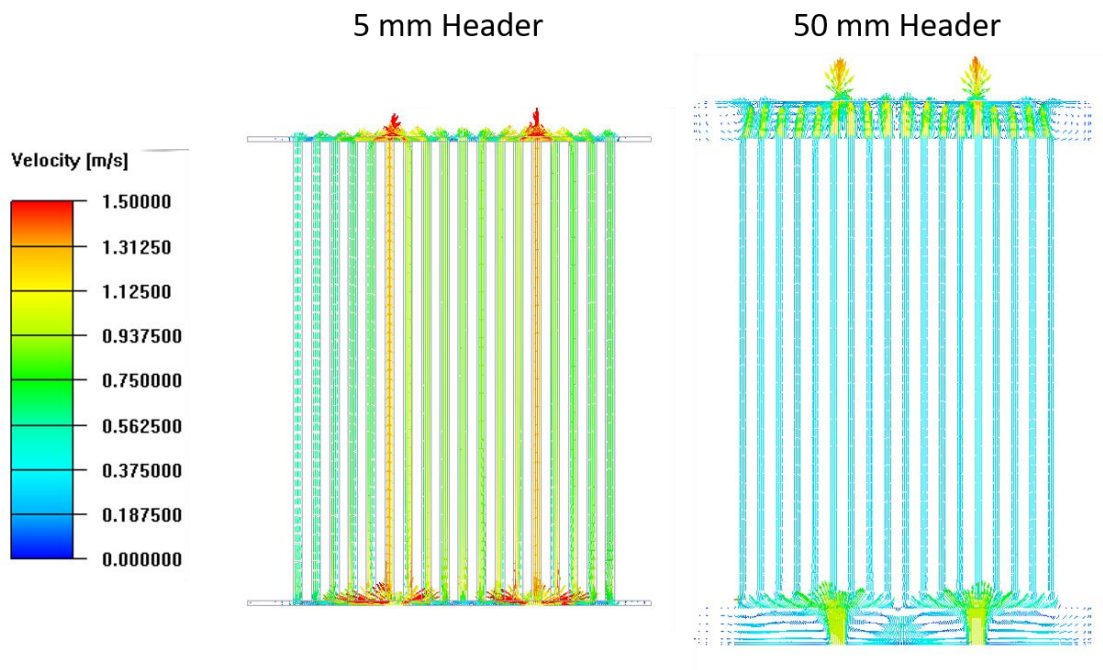

Figure 4-7 Velocity Vector of the Cooling Channel with Different Header Thicknes

From the velocity distribution in Figure 4-7, it is concluded that with thicker channels, not only the overall pressure drop will be decreased, but also the flow is more evenly distributed, which ensures the cooling performance in each cooling channel. However, too thick distribution header will consume more coolant, which is not very economical efficient. Therefore, the thickness of the header needs to be optimized to find out the appropriate minimum thickness for acceptable distribution of coolant. In the Figure 4-8, flow rate in each channels is listed for 3 cases with 5 mm, 30 mm and 50 mm header thickness. The 30 mm thick header is selected as final header thickness for acceptable pressure drop and flow rate distribution.

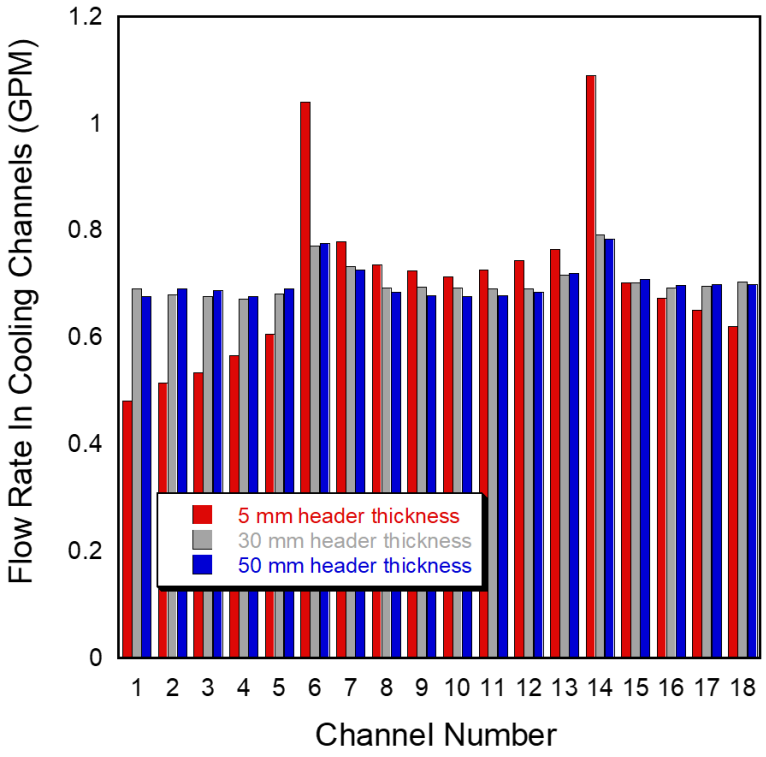

Figure 4-8 Flow Rate in Each Cooling Channel with Different Header Thickness

4.3.2 Detailed Magnetic Field Wire Housing Thermal Management Numerical Simulation

The whole magnetic field wire housing assembly with cooling channels can be split to unit geometry due to the circular symmetric pattern. This gives us the chance to evaluate detailed thermal management capability for each individual channels.

Figure 4-9 shows the schematic of copper wires embedded inside the 3D printed magnetic field wire housing with cooling channels. For copper wires inside cooling channel, the coolant exchanges heat with copper wires. For the regions where copper wire embedded inside the magnetic field wire housing without cooling channels,

portion of joule heat is conducted through the copper wire to the coolant in the cooling channel. The remaining heat is accumulated around copper wires, causing a local temperature rise. Therefore, the detailed thermal evaluation is performed on both cooling channels are non-cooled regions. For simplicity, the copper wire is fully embedded in the grooves in rectangular shape, whereas, in actual test scenario, the copper wire is round shape and a small portion of copper wire surface is inside the fluid domain.

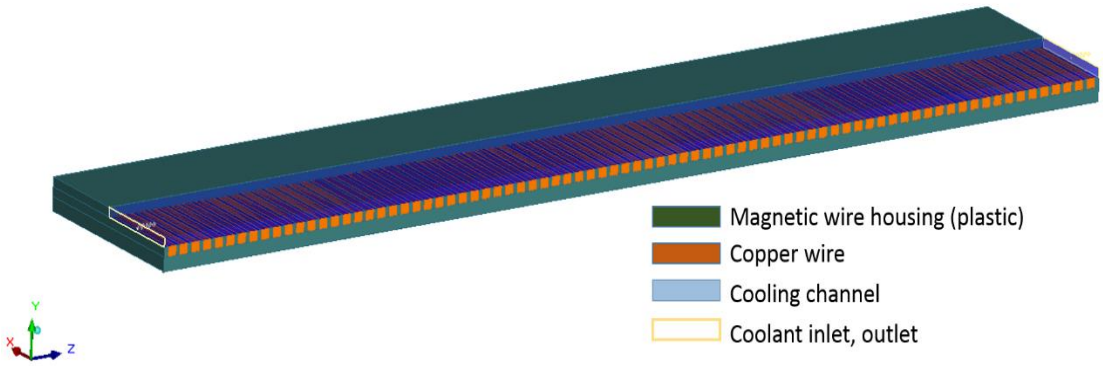

Figure 4-9 Schematic of Unit Geometry Thermal Modeling

(Dark green: plastic magnetic field wire housing by 3D printing, yellow: copper wires embedded inside the magnetic wire housing; blue: cooling channel)

In ANSYS model, for each cooling channel, there are 80 copper tubes, corresponding to 20 loops in each quadrant, embedded inside the plastic magnetic field wire housing. The wetting area ratio, *i.e.* ratio of cooling channel area to entire surface is around 50%. The current input and coolant flow rate are parametrized to evaluate cooling capacity for different cases.

4.4 Experimental Construction of Magnetic Field Wire Housing Assembly

The innovative 3D FDM printing technique has been chosen to construct the magnetic field wire housing with predetermined current-carrying pattern. Due to the versatility of 3D printing technology, slanted surface and complicated pattern are easily incorporated in the main body design for optimal magnetic field distribution. Based on previous numerical simulation result, it is promising to generate a strong magnetic field with excellent linearity distribution and such system can be sufficiently cooled down using external direct cooling approach. The Duratherm 450 Heat Transfer Oil is selected as coolant due to its outstanding properties, such as large dielectric constant, high heat capacity, low viscosity *etc*. Therefore, the experimental exploration of magnetic field wire housing with detailed construction process and data analysis will be discussed.

4.4.1 Magnetic Field Wire Housing Assembly System Overview

The detailed magnetic wire housing digital pictures for X, Y and Z layer are shown in Figure 4-10. The grey region on left side of X layer is JB-Weld epoxy, which serves as binder between copper wire and the groove. JB-Weld epoxy also prevents any possible Line X spray coating to block embedded cooling channel. Prior to final epoxy potting process for the whole assembly, BJB epoxy was applied to all layers as double safe protection measure to prevent potting epoxy penetration to the cooling channels. The AWG 10 copper wire in Z layer was embedded in fiberglass groove, due to the extraordinary temperature resistance and mechanical properties of G10 fiberglass, there is no cooling for ease manufacturability. However a 3D printed slanted surface was

attached to one side of Z layer to ensure the center point of all three layers are overlapping.

The external direct cooling approach benefits from low thermal conduction resistance, large contact area between heat source and coolant, however, it also poses challenges for coolant leakage free construction during assembly process.

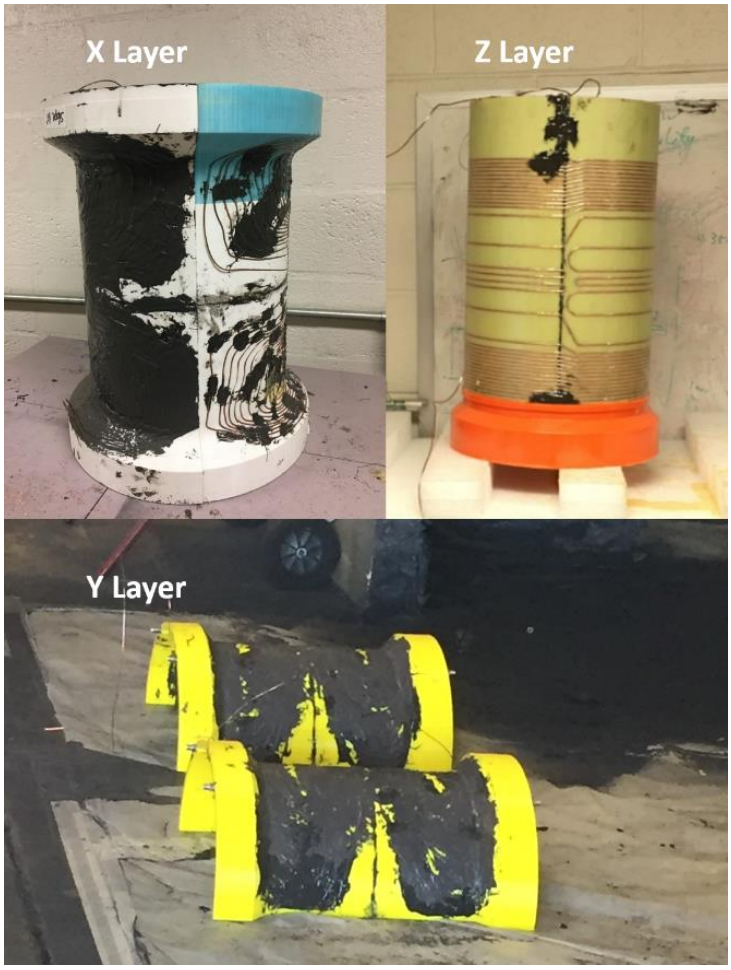

Figure 4-10 Digital Photo of X, Y and Z layer Copper Wire Pattern

(X and Y layer is coated with JB-weld epoxy and Line X coating)

In order to ensure the leakage-free from the cooling channel to outside assembly, multiple generations of sealing trials have been performed and tested until the results were satisfactory. Previous trials includes rolling numerous layers of epoxy or wrapping several layers of fiberglass sheet on the outer surface of the magnetic field wire housing and potting epoxy at both sides of magnetic field wire housing assembly. The nine generations of magnetic wire housing assembly with different sealing approaches are shown in Figure 4-11.

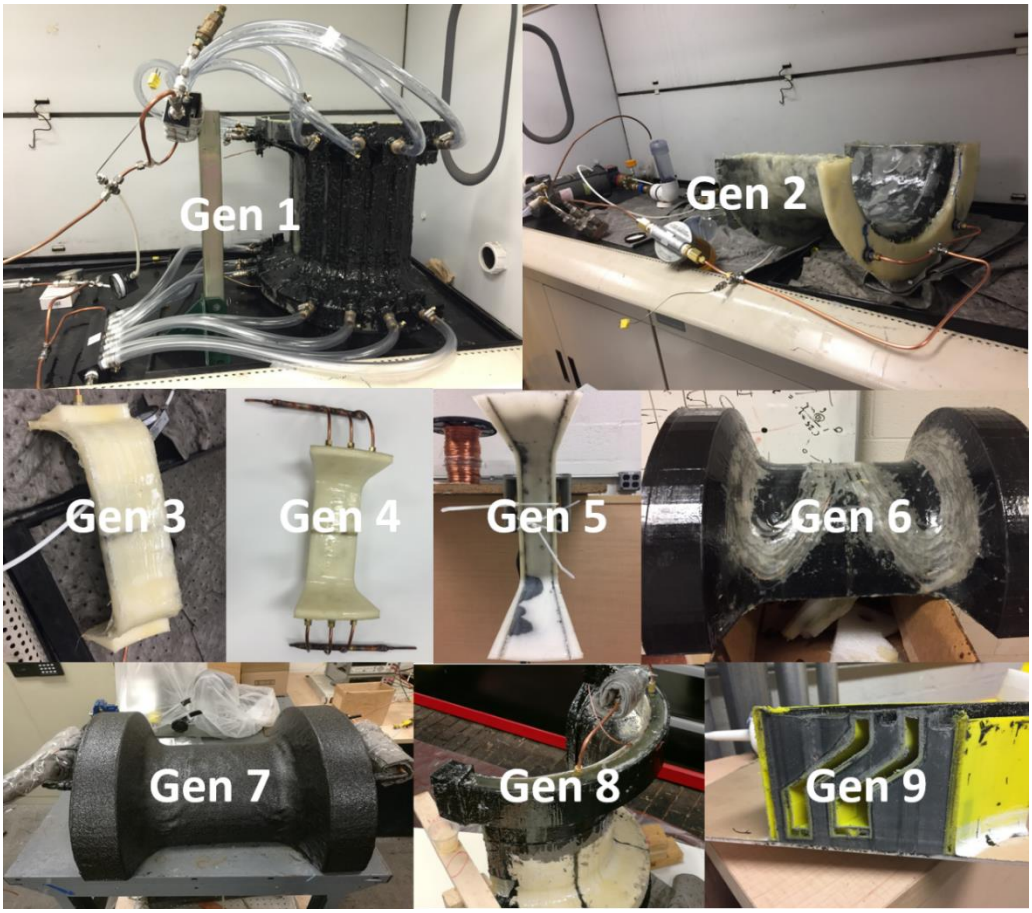

Figure 4-11 Multiple Generations of Magnetic Wire Housing Assembly with Different Sealing Approaches

After 3D printing, copper wire snapping, Line X coating, overall layers assembling and epoxy potting processes, a final overlook of the assembly is presented in Figure 4-12. The large copper tube above and below the assembly act as external flow distribution header. It collects the coolant from the pump, based on the magnetic field layer operation conditions, the coolant can be easily directed into operational layer for cooling purposes with the assist of ball valve. Multiple thermocouples were inserted at different locations between the layers prior to potting process to monitor the temperature inside the assembly for precaution purposes. After ~10 gallon of potting epoxy, the whole X, Y and Z layer were bonded internally with very strong mechanical properties due to the high strength of potting epoxy and G10 fiberglass tube as outer shell. At the same time, the low viscosity potting epoxy covers the entire housing surfaces, which provides great protection against coolant leakage. Then, the whole assembly is perfectly sealed and ready to be connected to the cooling subsystem.

Figure 4-12 Digital Picture of Final Magnetic Field Wire Housing after Epoxy Potting

The entire system is composed of centrifugal gear pump, pressure gauge, relief valve, flow meter, thermocouples, differential pressure gauge, magnetic field wire housing assembly, debris filter, heat exchanger, chilled water, power supply and oil reservoir. The schematic and actual digital picture are shown in Figure 4-13 and Figure 4-14. The debris filter is used as protection to trap any possible small particles to prior entering gear pump. The relief valves bypasses the coolant from system once the overall pressure is above set threshold for safety reasons. The pressure drop across the magnetic field wire housing assembly are accurately measured with differential pressure gauge and one absolute pressure gauge. The pressure difference and temperature readings can be obtained from pressure gauge, differential pressure gauge

and thermocouples before and after the coolant exchange heat with the copper wires inside magnetic field wire housing.

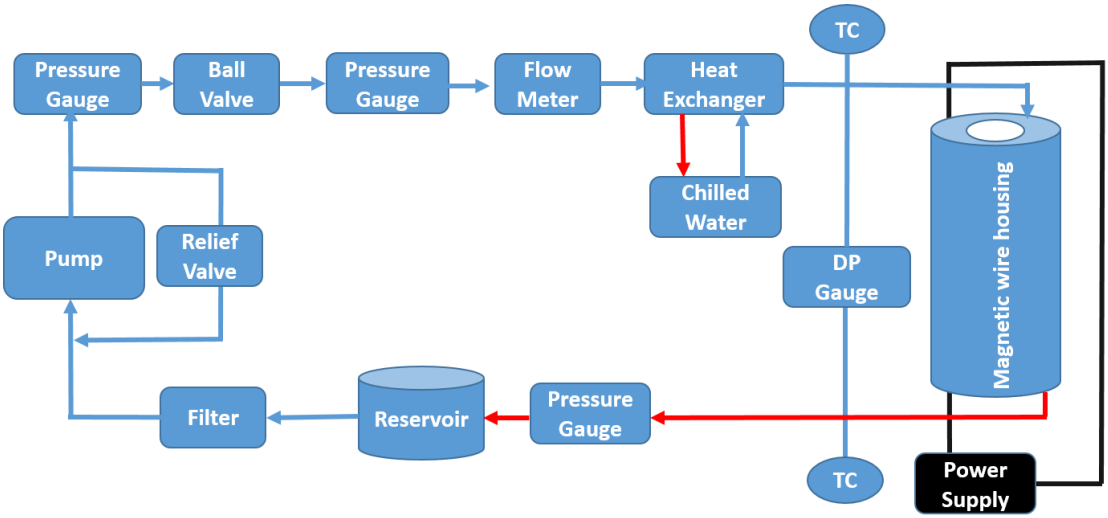

Figure 4-13 Schematic of Final Magnetic Field Wire Housing System Assembly

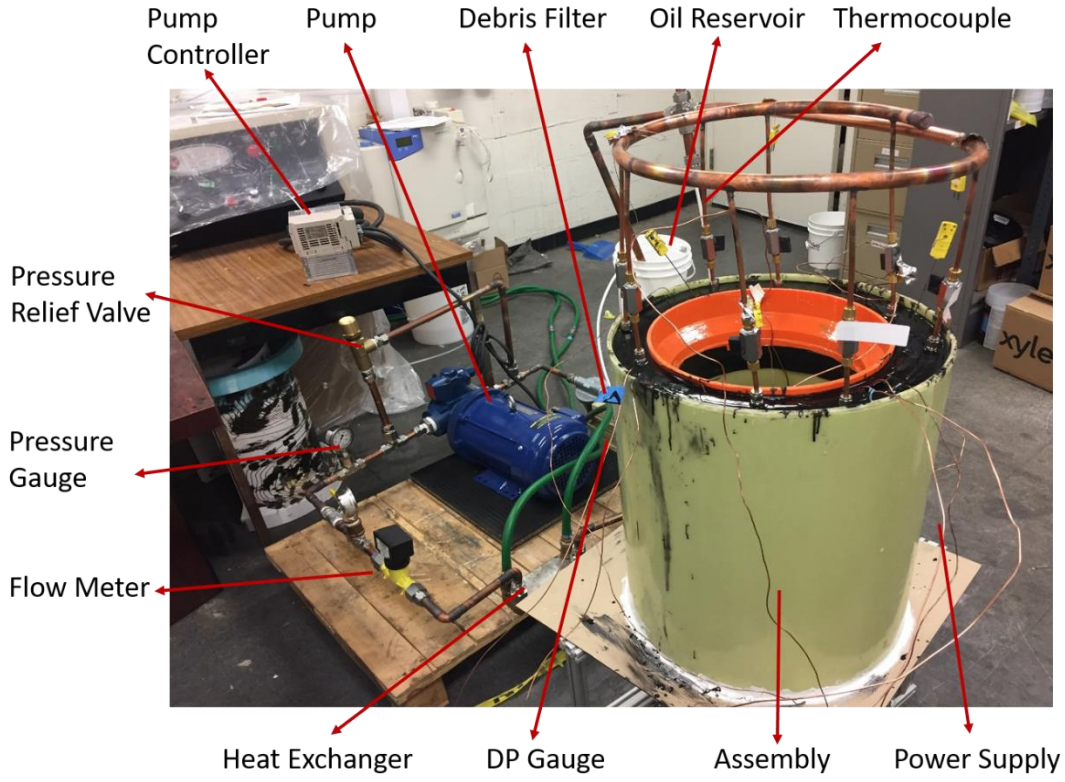

Figure 4-14 Digital Picture of Final Magnetic Field Wire Housing System Assembly

4.4.2 Experimental Result and Data Analysis

Now the magnetic field distribution and thermal management tests have been performed on full scale magnetic wire housing assembly. As mentioned in Figure 4-14, thermocouples were used to monitor the temperature between layers instead of IR camera. The temperature readings for X and Y layer are listed in the Table 5-6. From temperature result, it can be noted that the coolant experiences temperature rise after in contact with heated copper wire, which indicates effective heat transfer between coolant and copper wire. The increment of temperature reading of thermocouple placed between X and Y layer suggests there was some portion of thermal energy propagating from X layer to Y layer. Therefore, the overheating issue can be remedied by both convective cooling by circulating coolant and conduction dissipation through potting epoxy. The numerical simulation model was built to investigate the copper wire surface temperature and temperature distribution within the magnetic field wire housing assembly.

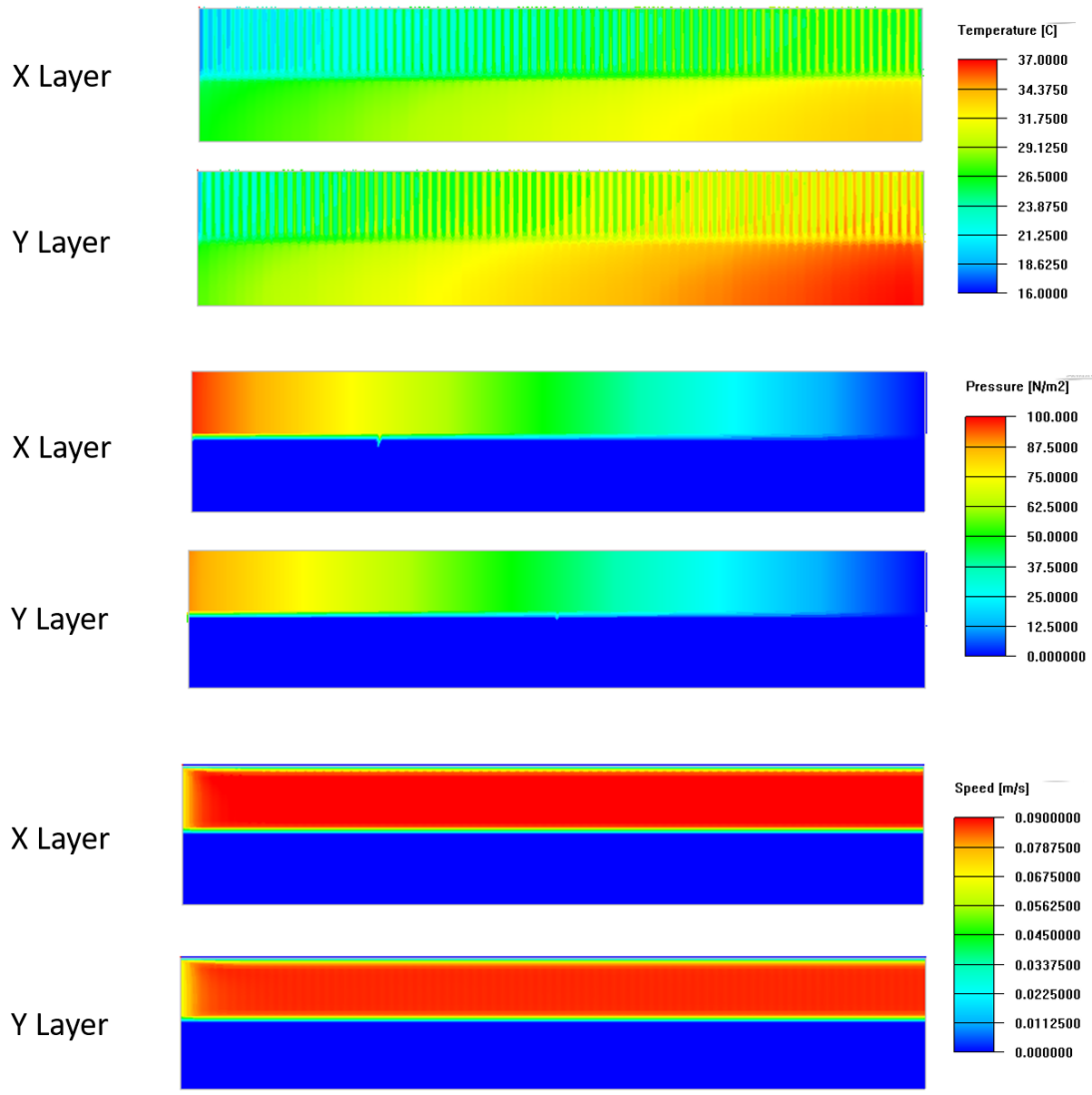

Figure 4-15 Numerical Thermal Simulation of X and Y layer Under Working Conditions

(X: 40 Amp, Y: 43 Amp)

When the copper wire temperature increases, it exhibits typical metal conductor behavior of electrical resistance increment. As a result, at constant voltage settings, the current reading of power supply experienced a slight drop (Table 5-7). In order to

prevent over-pressurize the entire magnetic field wire housing assembly, the pressure relief valve at the exit of the pump outlet was set to 20 PSI. Once the pump outlet pressure exceeds the pressure relief valve threshold, it will automatically bypass the coolant from the assembly. The relative low flow rate inside the cooling channel results in a small pressure difference between assembly inlet and outlet. Due to the relative large range of differential pressure gauge, the data listed below comes from numerical simulation based on experimental flow rate. One thing to note is due to the porous structure of 3D printed housing for X and Y layer, it is very likely to have coolant in the entire magnetic field wire housing main body besides the cooling channels. That feature provides larger heat transfer area between coolant and copper wire. Although the porous structure of 3D printed part poses significant flow resistance to coolant, leading to insufficient flow within the main body compared to cooling channels, the direct contact and heat exchange between cooper wire and coolant still provides some cooling effect.

Table 4-1 Experimental Cooling Result of Magnetic Wire Housing Assembly for X Layer (* pressure drop data is obtained via numerical simulation)

X Layer at 21 V Power Supply Test Condition					
Time (min)	0	3	5	10	15
T_inlet (ºC)	16.5	16.7	16.7	16.6	16.6
T_outlet (ºC)	16.7	17.9	17.9	18	18
T_xz (ºC)	25.3	26.6	26.7	26.9	27.1
T_xz (ºC)	23.9	23.6	23.6	23.7	23.7
T_xy (ºC)	25.2	25.3	25.3	25.3	25.3
Current (Amp)	43.1	42.6	42	41.48	41.44
Pressure Drop * (Pa)	98	98	98	98	98
Flow Rate (GPM)	5.326	5.326	5.322	5.324	5.322

Table 4-2 Experimental Cooling Result of Magnetic Wire Housing Assembly for Y Layer (* pressure drop data is obtained via numerical simulation)

Y Layer at 21 V Power Supply Test Condition					
Time (min)	0	3	5	10	15
T_inlet (ºC)	14.8	15.5	15.7	16.1	16.1
T_outlet (ºC)	14.9	16.7	17.2	17.3	17.3
T_yo (ºC)	24.4	24.3	24	23.9	24
T_yo (ºC)	24.6	24.4	24.3	24	23.7
T_xy (ºC)	25.1	25.1	25	25	24.9
Current (Amp)	48.24	47.61	46.34	46.14	46.08
Pressure Drop * (Pa)	98	98	98	98	98
Flow Rate (GPM)	5.151	5.206	5.222	5.222	5.230

Table 4-3 Experimental Temperature Distribution Data in Z Layer (with cooling in X layer)

Z Layer at 80 A Power Supply Test Condition (with cooling in X layer)					
Time (min)	0	0.5	1	3	6
T_inlet (ºC)	24.5	26	27.2	30.3	32
T_outlet (ºC)	24.6	26.2	27.3	30.5	32.6
T_xz (ºC)	24.5	27.2	29.3	35.0	45.3
T_yo (ºC)	24.2	24.2	24.3	24.3	24.3
T_xy (ºC)	24.4	24.4	24.5	24.6	24.6
Voltage (Volt)	17.48	18.2	18.5	19.1	19.25
Flow Rate (GPM)	5.326	5.326	5.322	5.322	5.322

With the direct cooling approach, maximum temperature in X and Y layer can be well controlled. However, since Z layer used G10 fiberglass for additional mechanical support and high temperature resistant benefits, there is no cooling designed for Z layer. Although both G10 fiberglass and potting epoxy can withstand very high temperature up to 200 ºC, the maximum temperature within Z layer still needs to be investigated to ensure safe operation. During Z layer operation, the coolant was directed to X layer to provide possible cooling for Z layer through potting epoxy and 3D printed part of X layer. A transient thermal model was built in ANSYS Workbench V 18.1 to simulate the temperature propagation behavior within Z layer. When Z layer was in operational

mode, the current through copper wire was 80 A with 19.25 V, which corresponding to a total power input of 1540 W.

Temperature development profile is shown in Figure 4-16. From the numerical result, it can be seen with only natural convection as cooling source, the maximum temperature will approach 212 ºC after 10 minutes. The temperature distribution is not symmetric, which is caused by Z layer copper wire asymmetric spatial distribution. Such asymmetric spatial distribution of Z layer copper wire pattern is specifically designed to ensure the overlap of center magnetic field among X, Y and Z layer within the entire magnetic field domain. Without direct cooling approach for Z layer, it is suggested to operate the system within 6 minutes. Although the circulating coolant in X layer is forced convective cooling, yet the low thermal conductivity of 3D printed plastic and potting epoxy pose extensive thermal resistance, leading to very limited cooling effect on Z layer. The X layer cooling effect was parametrized in Figure 4-17. Higher value of heat transfer coefficient indicates better cooling effect from X layer at higher coolant flow rate. With 20 W/m^2K, the maximum temperature of Z layer is lowered to 168 ºC. Higher convective heat transfer coefficient boundary conditions corresponds to better cooling effect from X layer. From the result, it can be seen that the maximum temperature is strongly dependent on cooling effect on Z layer outer surfaces. The of cooling effect on Z layer outer surface can be maximized by applying different approaches, such as reducing the potting epoxy layer thickness, replace potting epoxy with thermally conductive epoxy, and improve convective cooling performance in X layer.

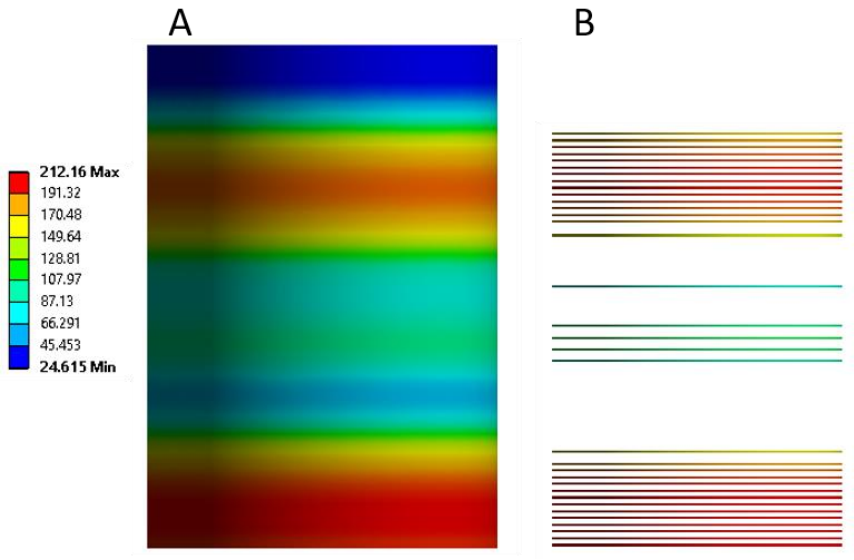

Figure 4-16 Transient Numerical Simulation of Temperature Distribution in Z Layer (a) Overall Temperature Distribution (b) Copper Wire Temperature Distribution (with cooling in X layer)

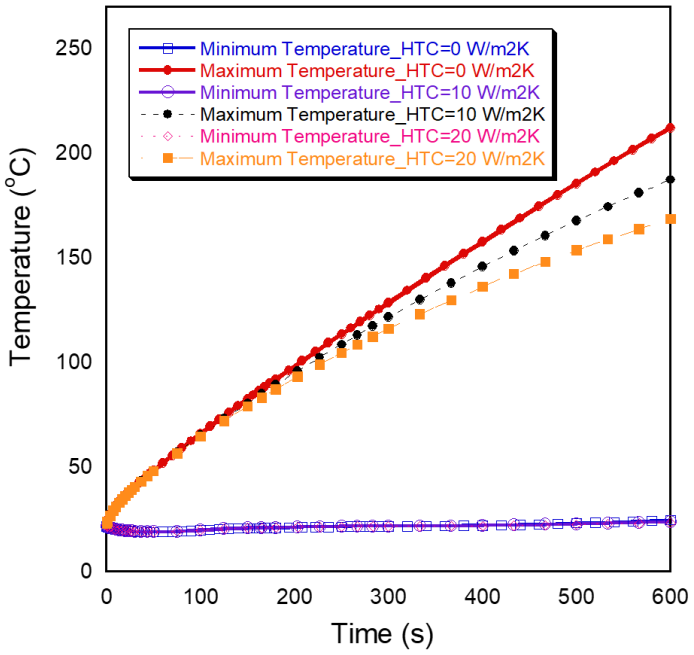

Figure 4-17 Numerical Simulation of Temperature-Time Relationship in Z Layer with Different Convective Heat Transfer Performance in X Layer

Apart from thermal management capability of X, Y and Z layers in magnetic field wire housing assembly, the magnetic field distribution data was mapped with a VGM magnetic field strength sensor. The VGM model magnetic field strength sensor from AlphaLab Inc has a range from 0 to 799 Gauss in three directions. The accuracy and resolution are 1-2% and 0.01 Gauss, respectively. In order to ensure accurate measurement readings from magnetic field sensor, a sensor frame was 3D printed as shown in Figure 4-18. The relative position between each point is pre-determined and the total 63 points provide enough data to 3D construct the magnetic field plane. The frame was placed at the center plane of the assembly for center plane magnetic field distribution mapping.

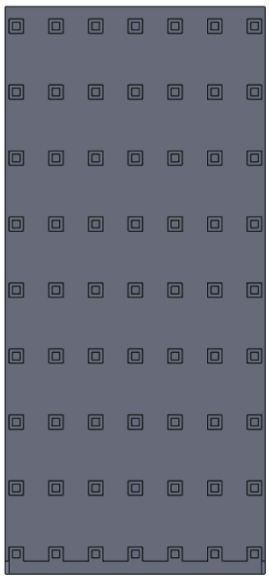

Figure 4-18 Sensor Frame for Magnetic Field Distribution Mapping

From the X, Y and Z magnetic field distribution at highest current input possible for each layer, the magnetic field 3D contour at the center plane were presented in Figure 4-19. Compared to the magnetic field distribution numerical simulation in Maxwell, there is acceptable inconsistency. Figure 4-20-22 shows line to line comparison between numerical and experimental result for each layer, where largest inconsistency occurs near the edge of the magnetic field domain. For numerical simulation result, magnetic field distribution near the edges is symmetrical and experience obvious increment when the edge approaches the copper wires. However for experimental results, the magnetic field distribution near that region is not perfectly symmetrical. Also the magnetic field strength exhibited only moderate increase near the copper wires. The error band is 20-30%, 20-30% and 15-20% for X, Y and Z layer based on linearity comparison between numerical and experimental data. That inconsistency may be attributed to the following reasons. (1) The error from magnetic field sensor. (2) The relative positioning for the sensor. (3) The simplification of geometry model in numerical simulation in Maxwell. (4) Non-perfect circular shape of X and Y layer in experiment testing.

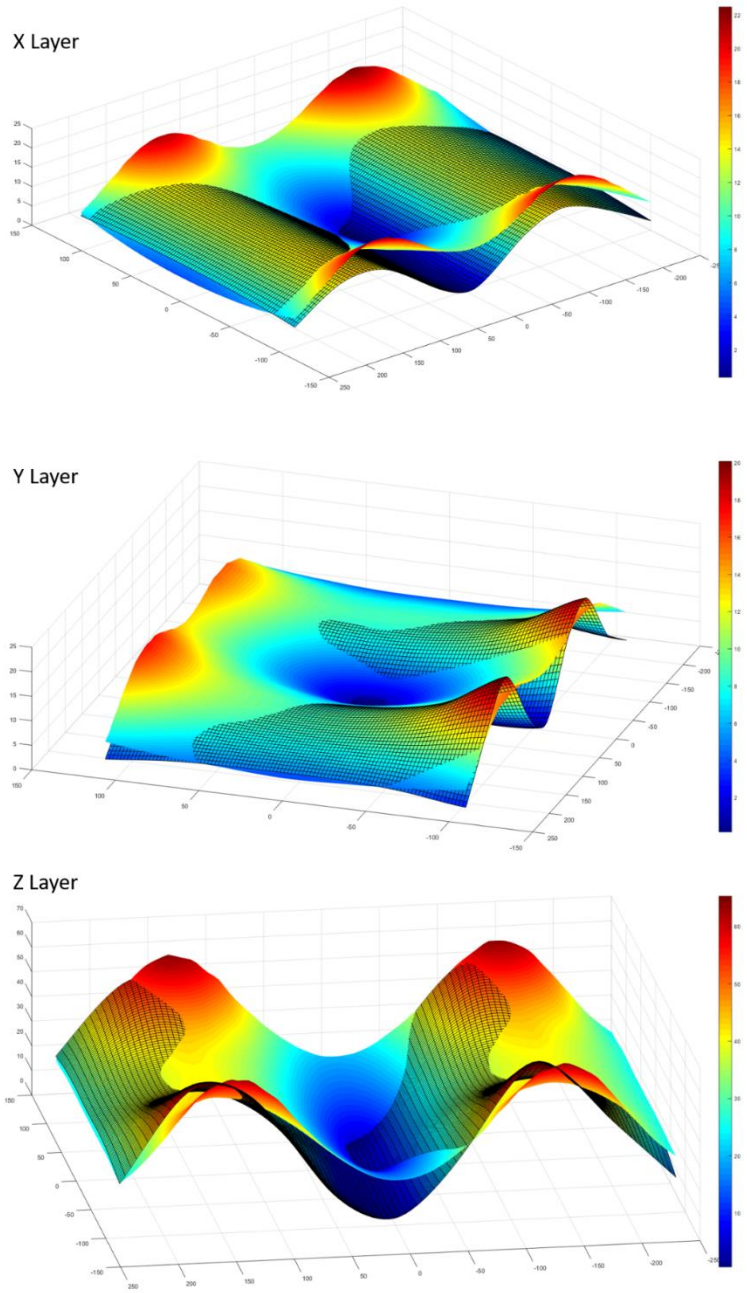

Figure 4-19 X, Y and Z Layer Magnetic Field Distribution

(Smooth contour: numerical simulation result, meshed contour: experimental result)

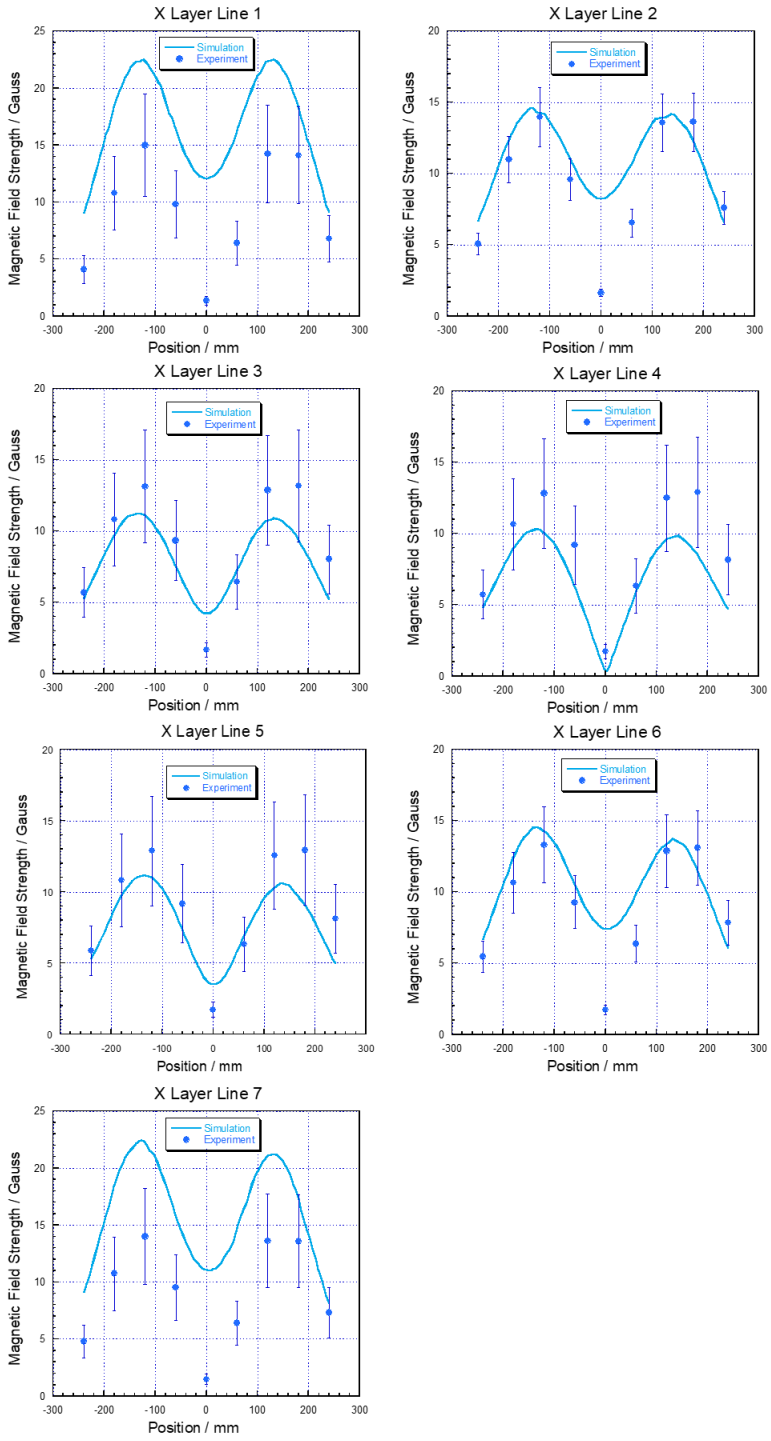

Figure 4-20 X Layer Magnetic Field Line Distribution Comparison between Experimental Data and Numerical Simulation with Error Bar from 20-30%

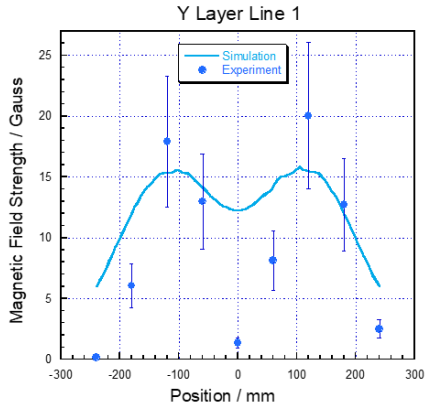
Y Layer Line 1
Simulation
Experiment
Magnetic Field Strength / Gauss
Position / mm

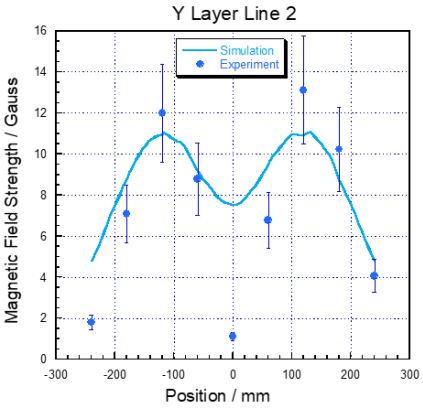
Y Layer Line 2
Simulation
Experiment
Magnetic Field Strength / Gauss
Position / mm

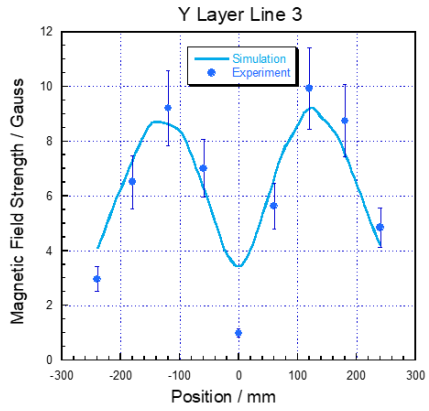
Y Layer Line 3
Simulation
Experiment
Magnetic Field Strength / Gauss
Position / mm

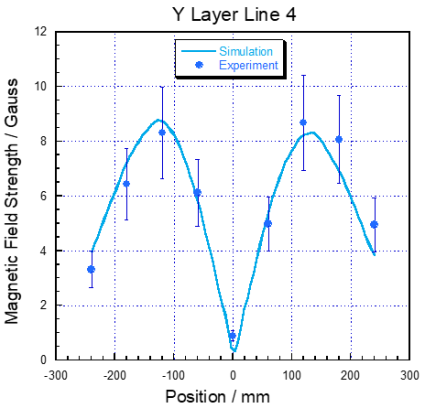
Y Layer Line 4
Simulation
Experiment
Magnetic Field Strength / Gauss
Position / mm

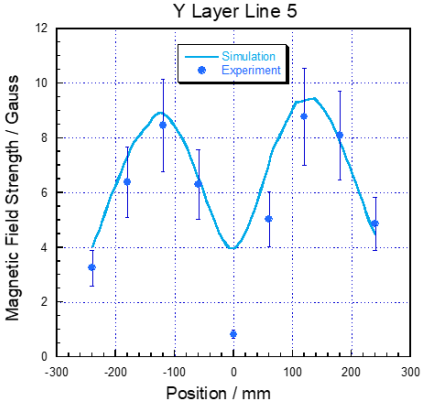
Y Layer Line 5
Simulation
Experiment
Magnetic Field Strength / Gauss
Position / mm

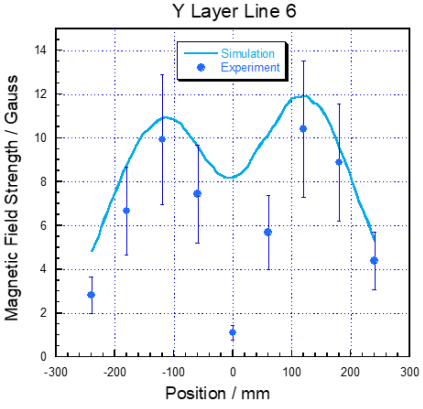
Y Layer Line 6
Simulation
Experiment
Magnetic Field Strength / Gauss
Position / mm

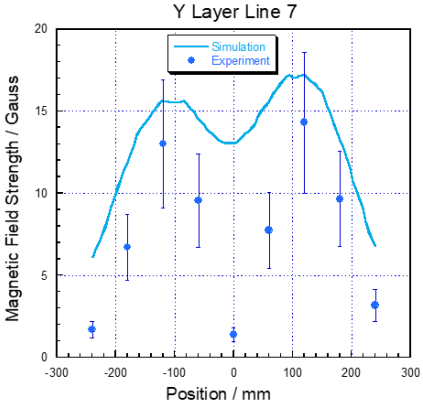
Y Layer Line 7
Simulation
Experiment
Magnetic Field Strength / Gauss
Position / mm

Figure 4-21 Y Layer Magnetic Field Line Distribution Comparison between Experimental Data and Numerical Simulation with Error Bar from 20-30%

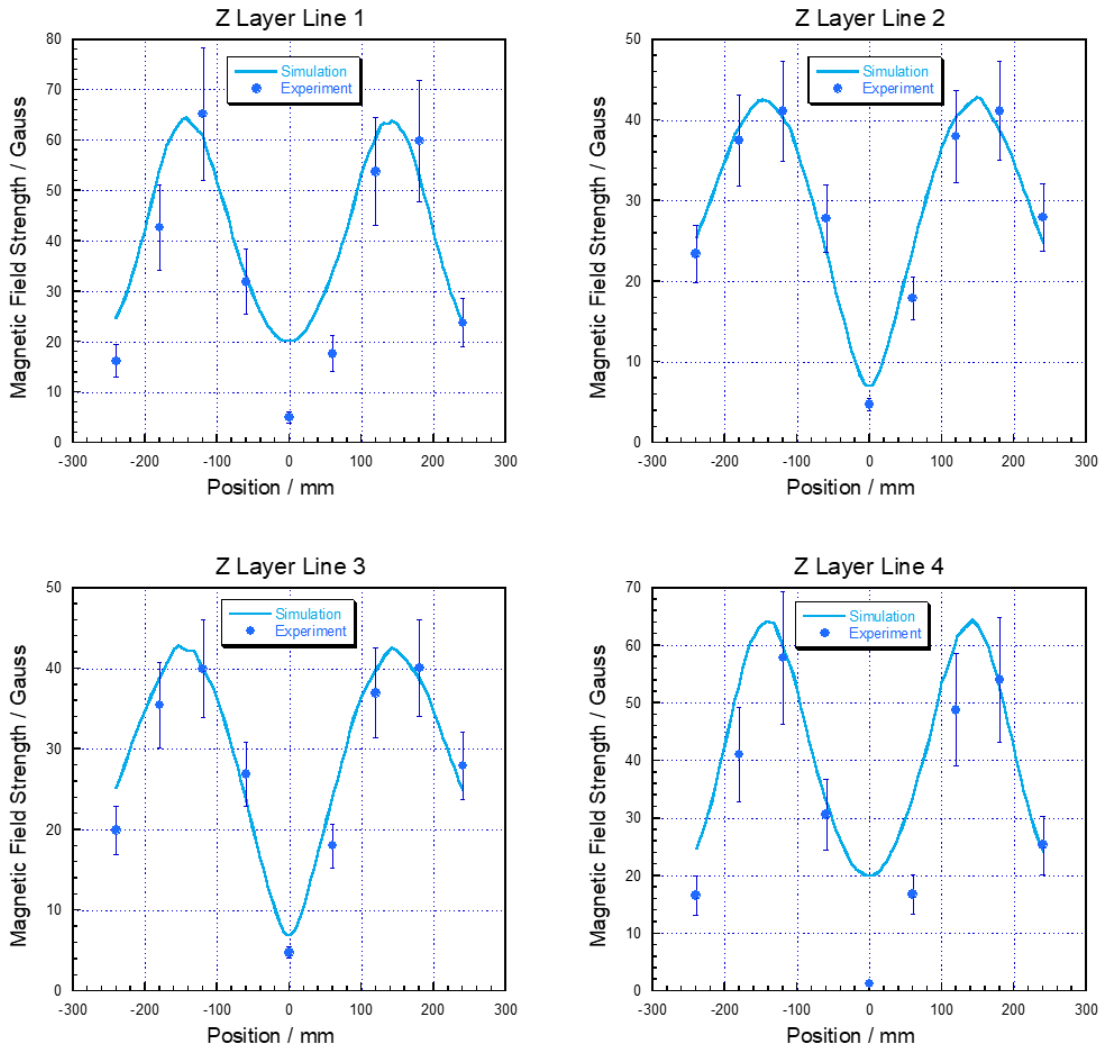

Figure 4-22 Z Layer Magnetic Field Line Distribution Comparison between Experimental Data and Numerical Simulation with Error Bar from 15-20%

4.5 Bi_2Te_3 Properties Modification with Magnetic Field

After characterizing magnetic field distribution of the assembly, investigation the effect of magnetic field on material properties was performed. The material chosen for this

test is bismuth telluride (Bi_2Te_3), which is a very commonly used topological insulator material in semiconductor industry, for example thermoelectric cooler (TEC) module. Bi_2Te_3 material benefits from high electrical conductivity and low thermal conductivity, which is favorable in TEC applications [71-74]. The high electrical conductivity will generate less joule heating inside the TEC module, and low thermal conductivity are mainly used to reduce the thermal short-circuit for performance enhancement purposes. Since the thermal conductivity and electrical conductivity are internally linked via Wiedemann-Franz Law, it is very interesting to investigate the magnetic field's effect on both properties, which may provide new opportunities or guidelines for TEC module design and optimization. Cai *et al.* studied N-type Bi_2Te_3 thermoelectric thin films at different anneal temperatures and found the electrical conductivity ranges from 0.2-0.9 x 10^5 S/m [75]. Zhou *et al.* investigated on Pb-doped Bi_2Te_3 films, which showed an electrical conductivity in the range of 1.2 to 3.1 x 10^5 S/m [76].

4.5.1 Bi_2Te_3 Material Properties Characterization within Magnetic Field and Data Analysis

Electrical conductivity is chosen as material property of interest for this characterization using a classic four probe resistance measurement approach (Figure 4-23). Four probe electrical resistance measurement has been proven to provide precise results as well as diverse specimen dimension from thin film to bulk materials. The probes were mechanically secured to the surface of test specimen with two inner probes measuring voltage, while the outer two probes measuring current passing through the

specimen. In such configuration, the error induced by voltage drop across the leads can be eliminated to achieve more accurate result.

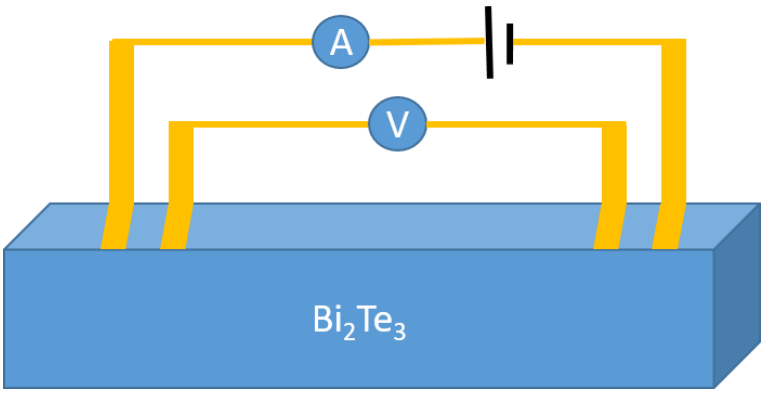

Figure 4-23 Schematic of Four Probe Electrical Resistance Measurement

The four probe electrical resistance system consists of a programmable DC power supply for power input, computer controlled LabVIEW program, Agilent 34410 A multimeter, Agilent 34401 A multimeter for both voltage and current measurement as shown in Figure 4-24. The instrument uncertainty from factory data sheet is listed in the Table 9.

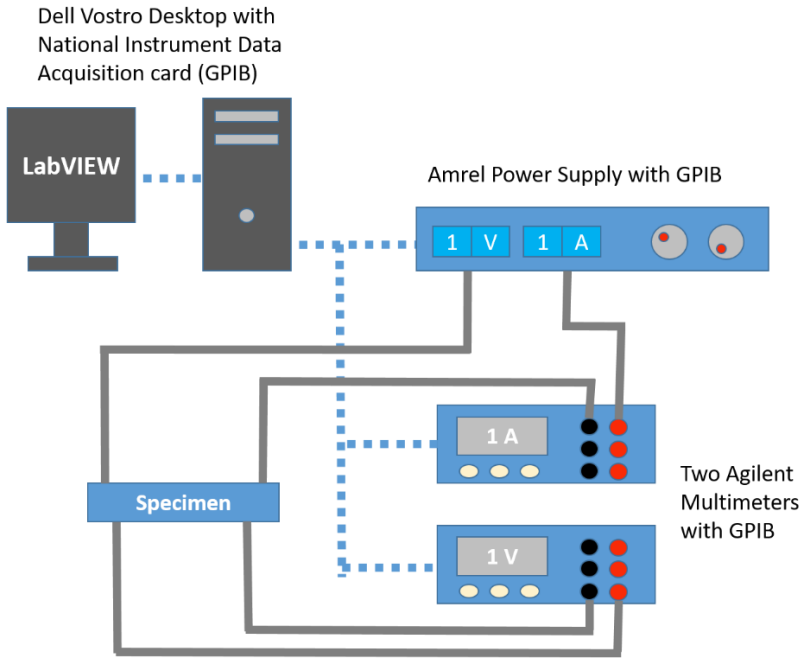

Figure 4-24 Schematic of Four Probe Measurement for Electrical Resistance

Table 4-4 Instrument Measurement Uncertainty

Parameters	Range	Uncertainty
Voltage	0-100 mV	0.003% of range
	0-1 V	0.006% of range
	0-10 V	0.004% of range
Current	0-1 mA	0.006% of range
	0-10 mA	0.02% of range
	0-100 mA	0.004% of range
	0-1 A	0.006% of range

The system uncertainty can be analyzed by applying principle of superposition of errors. The uncertainty is calculated based on following formula.

$$\frac{\Delta R_i}{R_i} = \sqrt{\left(\frac{\partial V}{V}\right)^2 + \left(\frac{\partial I}{I}\right)^2} \tag{27}$$

$$\bar{R} = \frac{\sum R_i}{n} \tag{28}$$

$$\frac{\Delta \bar{R}}{\bar{R}} = \sqrt{\sum \left(\frac{\partial \bar{R}}{R_i} \Delta R_i\right)^2} \tag{29}$$

From the experimental data, Bi_2Te_3 with dimension of 1 cm in length, 6 mm in width and 3 mm in height, shows an electrical resistance of 5257 ± 7.631 μΩ with magnetic field turned on. While a resistance of 5088 ± 7.712 μΩ was measured without magnetic

field. It can be seen that with magnetic field, the electrical resistance experiences an increase up to 3.3% magnetoresistance ratio (MR) at room temperature test condition. MR is dependent on magnetic field strength B and carrier mobility μ. For materials with equal holes and electrons, the MR increases with magnetic field strength. And the change of MR is positive for both magnetic field parallel and transverse to current directions [77].

$$MR = \frac{\Delta\rho}{\rho} = \frac{\rho - \rho_0}{\rho_0} \times 100\% \tag{30}$$

$$\frac{R_B}{R_0} = \frac{\rho_B}{\rho_0}(1 + g\mu^2 B^2) \tag{31}$$

Since the magnetic field direction is transverse to current direction, the existence of magnetic field will distort the electron moving path due to Lorentz force leading to a decreased current density. The prolonged electron path and lower current density exhibits relative higher resistance. In addition, the prolonged electron path also increases the possibility of electron collision, leading to an increase of electrical resistance. At the specimen surface, the magnetic field strength is about 6700 Gauss. Such magnitude of electrical resistance change of similar material agrees with the literature well. White discovered a 5-6% change for magnetic metals for permalloy [78]. Such magnetoresistive effect can be explained with the following formula. Distortion electron transport path is induced by Lorentz force:

$$\vec{F} = \vec{v} \times \vec{B} \tag{32}$$

where, F is the Lorentz force vector, v and B are electron moving speed and magnetic field vector, respectively.

$$R = R_0 + \Delta R \cdot \cos^2 \phi \tag{33}$$

where, R_0 is the isotropic electrical resistance and ΔR is the change in electrical resistance, ϕ is the angle between magnetic field and current direction.

The internal linkage between electrical property and thermal property gives us the chance to evaluate thermal conductivity of Bi_2Te_3 based on electrical properties. For semiconductors, the heat transfer mechanism include both phonon transport, *i.e.* lattice vibrations as well as electron transport. For some semiconductors and most metals, with given temperature, the cross-plane thermal conductivity and electrical conductivity exhibits a linear relationship. This behavior is defined by Wiedemann-Franz Law in Equation 11. Based on electrical resistance and specimen dimension, the electrical conductivity can be obtained at both magnetic and non-magnetic test condition. With Lorentz constant, the thermal conductivity can be calculated as well. The electrical and thermal conductivity data are shown in Figure 4-25.

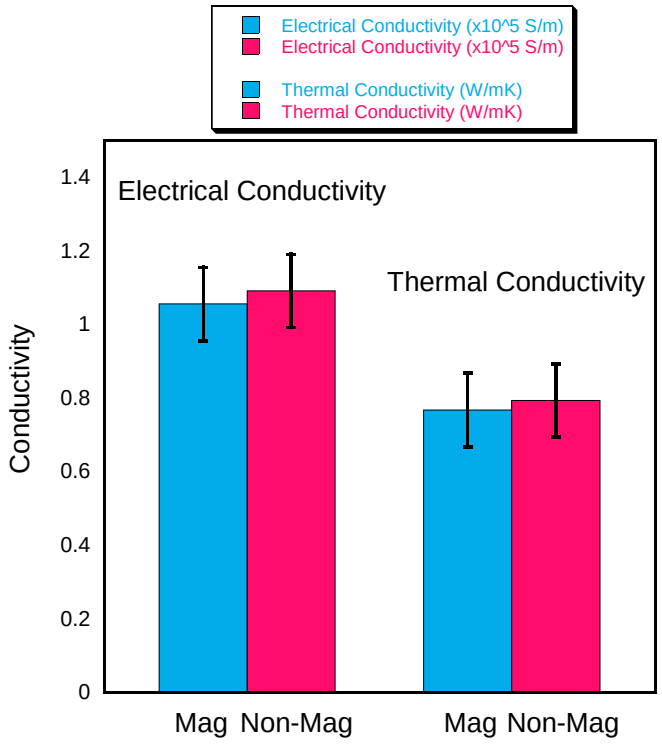

Figure 4-25 Electrical and Thermal Conductivity of Bi_2Te_3 with and without External Magnetic Field

4.5.2 Potential Application of Modified Bi_2Te_3 Material Properties

To further explore potential application of such property change of Bi_2Te_3, a thermoelectric cooler (TEC) module was built in ANSYS Thermoelectric. The TEC model consists of four Bi_2Te_3 thermoelectric legs (Figure 4-26 (a)) and the top sink side is fixed at a temperature of 110 ºC, which accounts for two phase cooling scenario with very high heat transfer coefficient. The bottom source has a heat flux input of 300 W/m^2, a typical value for CPU chips heat dissipation rate. The thermoelectric element was set to 50 µm thick with a current input of 3 Amp. The source side temperature and joule heat generation are compared for different properties of Bi_2Te_3. When the magnetic field is inactive, the Bi_2Te_3 electrical and thermal conductivity are 109195

S/m and 0.81 W/mK, respectively. While the magnetic field is activated, the electrical and thermal conductivity of Bi_2Te_3 exhibit slight decrease, showing the value of 105674 S/m and 0.79 W/mK, respectively.

When the TEC module numerical simulation were performed with different material properties of Bi_2Te_3, the source side temperature contour and joule heating within Bi_2Te_3 element are shown in the Figure 4-26 (b). Due to the decreased thermal conductivity of Bi_2Te_3 element, the thermal short-circuit between thermoelectric element are impeded, which enhances the thermal performance of TEC module. The maximum source side temperature of TEC working within magnetic field shows 19.8 ºC, which is 1.7 ºC lower than that of the non-magnetic field TEC module with a maximum temperature of 21.5 ºC. However, Figure 4-26 (c) shows the simultaneously dropped electrical conductivity generating more severe joule heating inside Bi_2Te_3 element. Therefore, there will be a trade-off when the thermal conductivity and electrical conductivity have the same trend. In order to apply magnetic field to improve TEC performance, the adverse joule heating effect needs to minimized, for example by applying lower operation current for bulk thermoelectric element application.

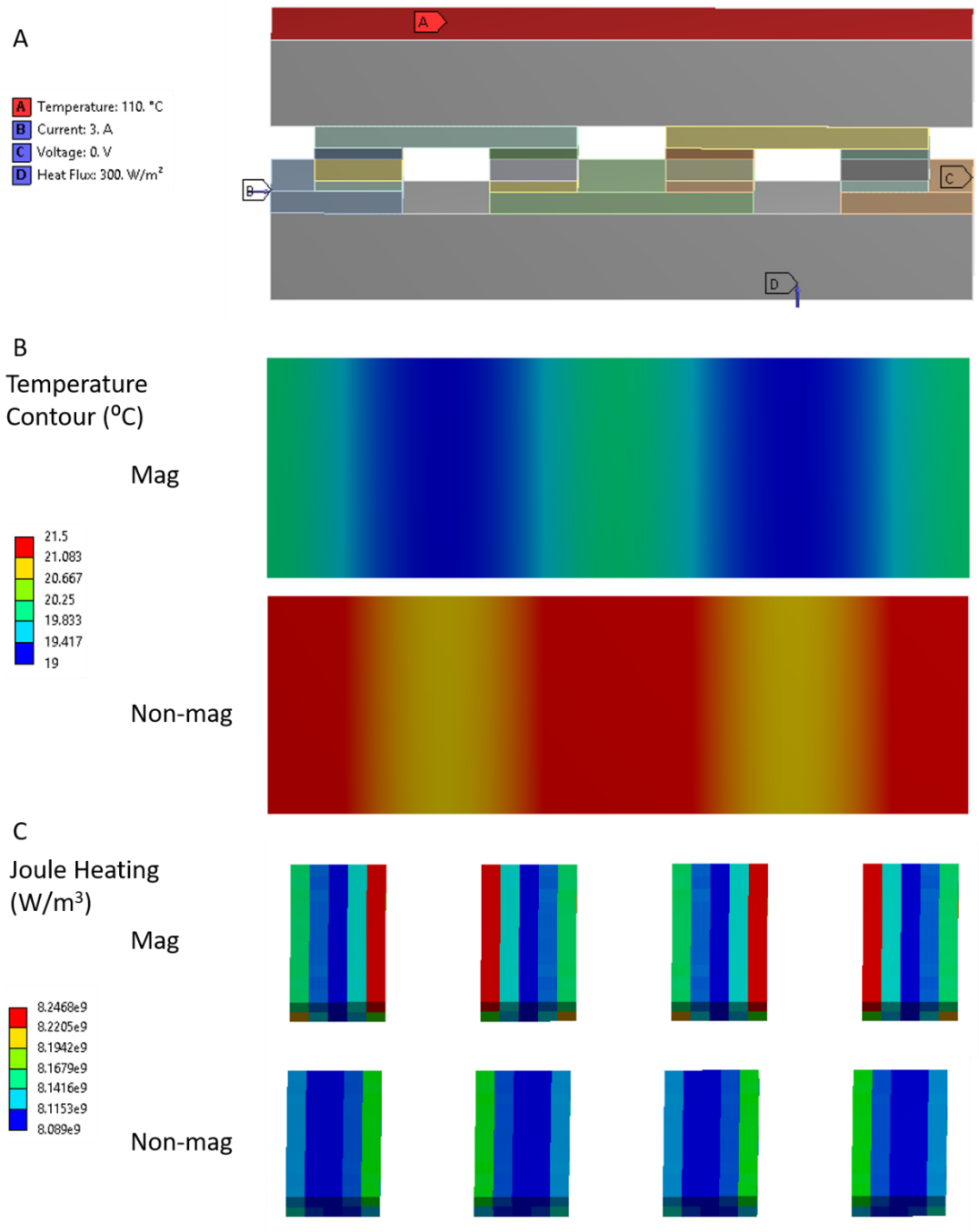

Figure 4-26 Numerical Simulation of TEC with Different Material Properties

(a) Schematic and Boundary Conditions of TEC Module, (b) Temperature Contour of Source Side, (c) Joule Heating of TE Element

4.6 Summary

In this chapter, a detailed numerical simulation of magnetic field distribution was investigated and presented. The magnetic field distribution comparison between experimental data and numerical simulation data shows acceptable uncertainty less than 30% at various locations. The highest uncertainty occurs at the edge of center plane, which may be attributed to location inconsistency caused by manual measurement. In addition, the experimental results for cooling performance and magnetic field distribution for entire assembly are presented. Experimental cooling performance for X and Y layer are in good agreement with numerical simulation. The experimental results show only 2 ºC increment between coolant inlet and outlet with negligible pressure drop at around 5 GPM total flow rate condition. Due to the inconvenience to monitor the copper wire surface temperature directly from experiment, simulation model was performed. For both X and Y layer, the maximum copper wire surface temperatures are less than 40 ºC, which validates the effectiveness of the direct cooling approach.

Experimental investigation of magnetic field's effect on Bi_2Te_3 material properties discussed. The electrical resistance characterization was carried out using a four probe method. Electrical resistance of Bi_2Te_3increases by 3.3% MR compared to non-magnetic field presence condition. Wiedemann-Frantz law states the relationship between electrical and thermal conductivity is proportional to Kelvin temperature and Lorentz constant. The thermal conductivity of $Bi_2Te_3$with and without magnetic field are obtained to be 0.81 and 0.79 W/mK, respectively. With tailored thermal and

electrical properties of Bi_2Te_3, potential application as thermoelectric material in TEC was evaluated using ANSYS Thermoelectric. With same geometry configuration and boundary condition, the lowered thermal conductivity of Bi_2Te_3 within magnetic field hinders the thermal short-circuit between thermoelectric elements, resulting in an overall enhanced performance of TEC module.

Chapter 5 Conclusion, Future Work, Major Contributions and Publications

5.1 Conclusion

Not all the properties of base material are desirable for each application. Therefore the ability to tailor unappealing material properties such as thermal and electrical properties without compromising material primary functional properties has attracted numerous attention for researchers. In this study, two different approaches to tailor material properties have been explored.

In the approach incorporating nanostructured materials with desired properties to base materials, the composite material exhibits both nanostructured material and base material properties. In current study, by incorporating 2D nanostructured boron nitride nanosheet with base materials, such as paraffin wax, cellulose nanofibers (CNF), base lithium ion polymer separator and glass, the thermal conductivity and electrical insulating properties of such composites have been significantly improved, while the primary base material functions are preserved at the same time. For power system, Wax-BNNSs composite exhibits 12 times enhancement in thermal conductivity with 80.15 J/g heat of fusion to provide enough heat dissipation capability in thermal management system. Meanwhile, 11.3-13.3 MV/m breakdown voltage is achieved compared to that of pure base paraffin wax (6.3-7.3 MV/m). When boron nitride nanosheets is added to CNF base material in optoelectronics system, the thermal conductivity value for BN-CNF composite exhibits 0.76 W/mK, which is 19 times

improvement compared to CNF base material, while still maintaining 70% optical transparency. When boron nitride is coated on commercially available polymer separator, the overall improved thermal conductivity assist the system to maintain at 92% Coulombic efficiency at 0.5 mA/cm^2, while the pristine separator suffers from a dramatic Coulombic efficiency decay after 60 cycles. Similarly, by coating the BN on pure glass, the heat dissipation capability of the substrate can be significantly increased, leading to higher reliability at 1000 ºC operation condition, while the pure glass substrate is not reliable near 700 ºC. The extraordinary heat dissipation performance of the BN/Glass is due to the high in-plane 14 ± 5W/mK and the low cross-plane 0.4 ± 0.15 W/mK thermal conductivities of the BN thin film, which leads to better heat dispassion along the BN surface and helps to block the heat transfer to the substrate underneath the device. Such nanostructured material incorporation method can be used to steer the overall effective properties towards better system performance, revealing its remarkable significance in product and system design.

Material properties can be also modified by applying external magnetic field. The electrical resistivity of Bi_2Te_3 characterized within magnetic field showed a 3.3% increment compared to the non-magnetic field condition. Thermal conductivity is linked to electrical conductivity via Wiedemann-Frantz law. With both altered thermal and electrical properties of Bi_2Te_3 material, a thermoelectric model was built to explore its potential application. Within the magnetic field, the thermoelectric model showed a 1.7 ºC better cooling temperature under the same operating condition. The decreased

thermal conductivity contributes to less thermal short-circuit within TEC module, leading to a better overall performance.

5.2 Future Work

This study provides important and comprehensive information in detail for designing magnetic field assembly, numerical optimization of cooling performance and magnetic field distribution with experimental validations, material property characterization inside the magnetic field and potential application evaluation. In order to further investigate the effect of magnetic field on material property, different optimization approaches can be carried out.

5.2.1 Optimization of Magnetic Field Distribution

Optimization of Magnetic Field Wire Pattern

In current effort of mapping magnetic field, many factors have attributed to the magnetic field distribution, such as wire pattern and current density through the copper wire. Based on pre-determined magnetic field distribution using target field approach, the copper wire pattern can to be further optimized for a more uniform and stronger magnetic field. It is well known that thinner copper wire can be winded to a more compact wire pattern, *i.e.* the current density will be improved. Ideally to obtain a stronger magnetic field, thinner wire with more compact wire pattern is recommended. However, the higher electrical resistance of thinner wire poses greater overheating risk resulted from accumulated joule heating. To compensate overwhelming joule heating effect, the current through the copper wire will be limited. At given current input condition, the magnetic wire pattern can be further optimized for both thermal and

magnetic perspectives. With the consideration of both magnetic field strength and overheating issues tradeoff, the copper wire pattern and material selection needs to be carefully evaluated and optimized using boundary element method and thermal modeling approach.

Optimization of Magnetic Field Domain Size

The overall dimension for each magnetic wire housing layer directly determines the magnetic field domain for testing. At same operating condition, the overall magnetic field strength can be improved with smaller size of magnetic wire housing assembly followed by Biot-Savart law. However, on the other side, the magnetic field region should be large enough to fit testing apparatus setup inside. From the discussion in previous chapters, the magnetic field strength decays as the sensor moves away from the surface of magnetic wire housing. To design a magnetic field with three directions, the distance between overall assembly geometry centers to each layer needs to be precisely designed and manufactured.

5.2.2 Optimization of Thermal Management Performance for Magnetic Field Wire Housing

In the current study, the coolant flow was demonstrated to be evenly distributed into thirty six cooling channels for both X and Y layer magnetic field wire housing. The approximately 50% cooling region results in acceptable temperature difference between cooled region and non-cooled region at ~40 Amp working condition, which exhibits tolerable temperature fluctuation on the magnetic field wire housing surface as indicated by ANSYS numerical thermal simulation. As future working condition

may use higher current input for higher magnetic field strength, the temperature fluctuation between cooled and uncooled region is no longer negligible. To solve that problem, the cooling channel distribution needs to be further optimized to yield not only optimized cooling area ratio but also minimize temperature fluctuation of the entire magnetic field wire housing assembly with optimal coolant flow.

Another important factor to design next generation of magnetic field wire housing assembly is the operational mode for each layer. In this dissertation, steady state operation condition is applied in terms of evaluating system thermal management capability. However, in actual test conditions, if the system is not required to be operated continuously, the pulsate operating conditions may allow the system to work with a current input higher than designed condition for a short period of time without experiencing significant overheating issues. Such pulse operation pattern can be further investigated to provide guidance in next magnetic field housing assembly design.

5.2.3 Investigation of Magnetic Field Effect on Super-Lattice Material Thermal Properties

Direct Thermal Conductivity Characterization

In this dissertation, the thermal conductivity values of bulk Bi_2Te_3 are obtained by combining Wiedemann-Franz law with experimental electrical conductivity data. Such empirical correlation is based on the assumption that the Lorentz number for Bi_2Te_3 is constant at room temperature. This thermal conductivity property data can be further validated by performing thermal conductivity characterization directly in the magnetic field. Furthermore, the effect of magnetic field on super-lattice structured Bi_2Te_3 can

be investigated. Different thermal conductivity characterization approaches can be applied.

Depending on the size and configuration of the magnetic field, thermal conductivity test setup can be further evaluated and constructed. For large magnetic field domain, the non-contact laser power as heat source is preferred. After applying laser power on specimen, the temperature distribution of entire specimen can be captured by IR camera for thermal conductivity characterization. However, if the magnetic field domain is limited or if the orientation of the magnetic field wire housing is not suitable for laser-IR camera setup, the electrical heater can be used as heat source and thermocouples can be used for temperature gradient characterization. With consideration of all the conditions mentioned above, the thermal conductivity measurement setup can be constructed to explore the effect of magnetic field on various semiconductor materials.

Investigation of Transient Magnetic Field Effect on Material Properties

In this study, the effect of steady state magnetic field on Bi_2Te_3 thermal and electrical properties has been investigated. While in future potential applications, the transient operational mode of magnetic wire housing assembly may lead to better performance in a short period of time without obvious thermal overheating crisis. Based on the material properties and current operational mode, an optimized cooling approach could be proposed accordingly. Such transient magnetic field strength rapid change may cause interesting phenomena inside the system. Therefore, it is possible to explore the transient effect of magnetic field on material properties as well.

5.3 Contributions

This dissertation provides important and comprehensive information to tailor thermal properties of various nanostructured materials. The additive approach has been successfully demonstrated to tailor material properties with nanostructured material boron nitride (BN) for various electronic systems with experimental validation. The BN-composite all exhibit excellent overall performance for each system. Besides the additive method, the effect of magnetic field on material thermal properties has been investigated. Detailed numerical simulation for magnetic field wire housing cooling strategies have been proposed and thoroughly evaluated. The temperature and magnetic field distribution data are collected and analyzed. Both electrical (from experimental test) and thermal properties (from Wiedermann-Frantz Law correlation) experience around 3.3% change within magnetic field. The major achievements and accomplishments of current work are listed as follows:

5.3.1 Material Thermal Properties Modification with Nanostructured Materials.

a. Thermal conductivity characterization setup was designed and constructed for Wax-BNNSs composite. The thermal conductivity of Wax-BNNSs composite experienced 12 times enhancement for better thermal regulation capacity. Differential scanning calorimetry (DSC) technique was applied to explore heat absorption capacity of Wax-BNNSs composite during endothermic process. Wax-BNNSs composite exhibited 80.17 J/g heat of fusion. In the meantime, the

break down voltage test setup was constructed to characterize Wax-BNNSs composite electrical insulating properties of Wax-BNNSs composite. With the addition of BNNS, the Wax-BNNSs composite breakdown threshold has been improved to 11.3-13.3 MV/m. Dielectric constant characterization was performed on Wax-BNNSs composite.

b. Steady state thermal conductivity characterization setup has been modified to evaluate thermal conductivity of BN-CNF nanopaper for optoelectronic systems. The overall thermal conductivity of BN-CNF nanopaper has been improved to 0.76 W/mK (compared to pure CNF nanopaper of 0.04 W/mK). The Laser-IR camera test has been successfully performed to qualitatively characterize heat dissipation capability of BN-CNF nanopaper. By incorporating BN layer, the heat can be effectively dissipated, which yields more uniform temperature distribution.

c. Laser-IR Camera system was carefully set up to map temperature distribution of BN-coated lithium ion battery separator. Graphite coating was applied to accurately capture the temperature on the surface of BN-coated lithium ion battery separator. BN thin film on separator facilitated heat dissipation leads to a more homogeneous thermal environment, which is critical for stability of Li metal anodes. The concept of using a thermally conductive separator is experimentally validated.

d. Heat source-IR camera system was successfully built to capture maximum operation temperature of RGO-film on BN-coated glass. Maximum temperature of substrate and power relationship was analyzed to evaluate potential applications for BN-coated glass. Numerical thermal simulation was performed to investigate the effect of BN coating thickness on overall performance.

5.3.2 Bi_2Te_3 Material Properties Modification with External Magnetic Field

Numerical Modeling:

a. Created a variety of system level magnetic field distribution model in ANSYS Electronics Desktop Maxwell to optimize the wire pattern to enhance field uniformity and homogeneity.
b. Created complicated 3D CAD model in Solidworks for entire magnetic field wire housing assembly. Cooling channel and slanted surface features were incorporated in CAD model.
c. Coolant flow distribution has been optimized using ANSYS Fluent/ ICEPAK to provide guidelines for flow distribution header design and detailed cooling performance evaluation. Pressure drop and flow rate of each individual cooling channel were successfully calculated.
d. Numerical modeling of thermal management capability of coolant on copper wire as heat source has been investigated in ANSYS ICEPAK for various operating conditions. Detailed modeling of

temperature distribution within each individual cooling channel are provided and analyzed.

e. Based on the experimental data of electrical and thermal properties of Bi_2Te_3, a thermoelectric model has been successfully carried out to explore potential applications.

Experimental Characterization:

a. Designed and constructed nine generations of magnetic field wire housing with different features, such as cooling channel design, coolant distribution header design, copper wire pattern as well as slanted surface optimization using 3D printing technology. 3D printing material selection and comparison were presented.

b. Developed and constructed entire system loop for magnetic field wire housing assembly, including thermal evaluation subsystem, powering subsystem, cooling subsystem and measurement subsystem.

c. Experimentally explored the sealing and potting techniques to construct a leak-free system with different trials of multiple epoxies.

d. Experimentally demonstrated the cooling performance of magnetic field wire housing assembly, which is in good agreement with numerical simulation results.

e. Experimentally mapped the magnetic field distribution for X, Y and Z layer. The comparison with numerical simulation results shows a 20-30%, 20-30% and 15-20% reasonable inconsistency.

f. Performed electrical resistance characterization on Bi_2Te_3 with and without magnetic field using a four probe method.

5.4 Publications

Journal Papers (16):

* marks the co-first author

1. **Zhi Yang**, Lihui Zhou, Wei Luo, Jiayu Wan, Jiaqi Dai, Xiaogang Han, Kun Fu, Doug Henderson, Bao Yang, and Liangbing Hu. "Thermally conductive, dielectric PCM–boron nitride nanosheet composites for efficient electronic system thermal management." Nanoscale 8, no. 46 (2016): 19326-19333.
2. Tingting Gao, **Zhi Yang***, Chaoji Chen, Yiju Li, Kun Fu, Jiaqi Dai, Emily M. Hitz, Hua Xie, Boyang Liu, Jianwei Song, Bao Yang and Liangbing Hu. "Three-Dimensional Printed Thermal Regulation Textiles." ACS nano (2017).
3. Han, Xiaogang, **Zhi Yang***, Bin Zhao, Shuze Zhu, Lihui Zhou, Jiaqi Dai, Jae-Woo Kim, Boyang Liu, John W. Connell, Teng Li, Bao Yang and Liangbing Hu. "Compressible, Dense, Three-Dimensional Holey Graphene Monolithic Architecture." ACS nano 11, no. 3 (2017): 3189-3197.
4. Li, Yiju, Tingting Gao, **Zhi Yang***, Chaoji Chen, Wei Luo, Jianwei Song, Emily Hitz, Chao Jia, Yubing Zhou, Boyang Liu, Bao Yang and Liangbing Hu. "3D‐Printed, All‐in‐One Evaporator for High‐Efficiency Solar Steam Generation under 1 Sun Illumination." Advanced Materials (2017).
5. Wan, Jiayu, Jianwei Song, **Zhi Yang***, Dylan Kirsch, Chao Jia, Rui Xu, Jiaqi Dai, Mingwei Zhu, Lisha Xu, Chaoji Chen, Yanbin Wang, Yilin Wang, Emily

Hitz, Seven D. Lacey, Yongfeng Li, Bao Yang and Liangbing Hu. "Highly Anisotropic Conductors." Advanced Materials 29, no. 41 (2017).

6. Wang, Yilin, Lisha Xu, **Zhi Yang***, Hua Xie, Puqing Jiang, Jiaqi Dai, Wei Luo, Yonggang Yao, Emily Hitz, Ronggui Yang, Bao Yang and Liangbing Hu. "High Temperature Thermal Management with Boron Nitride Nanosheets." Nanoscale (2017).
7. Luo, Wei, Lihui Zhou, **Zhi Yang***, Jiaqi Dai, Emily Hitz, Yudi Kuang, Xiaogang Han, Bao Yang, and Liangbing Hu. "Protection of boron nitride nanosheets by atomic layer deposition toward thermal energy management applications." Nano Energy 40 (2017): 149-154.
8. Zhou, Lihui, **Zhi Yang**, Wei Luo, Xiaogang Han, Soo-Hwan Jang, Jiaqi Dai, Bao Yang, and Liangbing Hu. "Thermally conductive, electrical insulating, optically transparent bi-layer nanopaper." ACS applied materials & interfaces 8, no. 42 (2016): 28838-28843.
9. Li, Tian, Mingwei Zhu, **Zhi Yang**, Jianwei Song, Jiaqi Dai, Yonggang Yao, Wei Luo, Glenn Pastel, Bao Yang, and Liangbing Hu. "Wood composite as an energy efficient building material: guided sunlight transmittance and effective thermal insulation." Advanced Energy Materials 6, no. 22 (2016).
10. Jia, Chao, Yiju Li, **Zhi Yang**, Guang Chen, Yonggang Yao, Feng Jiang, Yudi Kuang, Glenn Pastel, Hua Xie, Bao Yang, Siddhartha Das and Liangbing Hu. "Rich Mesostructures Derived from Natural Woods for Solar Steam Generation." Joule 1, no. 3 (2017): 588-599.

11. Li, Yiju, Tingting Gao, **Zhi Yang**, Chaoji Chen, Yudi Kuang, Jianwei Song, Chao Jia, Emily M. Hitz, Bao Yang, and Liangbing Hu. "Graphene oxide-based evaporator with one-dimensional water transport enabling high-efficiency solar desalination." Nano Energy 41 (2017): 201-209.
12. Luo, Wei, Lihui Zhou, Kun Fu, **Zhi Yang**, Jiayu Wan, Michael Manno, Yonggang Yao, Hongli Zhu, Bao Yang, and Liangbing Hu. "A thermally conductive separator for stable Li metal anodes." Nano letters 15, no. 9 (2015): 6149-6154.
13. Chen, Chaoji, Yiju Li, Jianwei Song, **Zhi Yang**, Yudi Kuang, Emily Hitz, Chao Jia, Amy Gong, Feng Jiang, J.Y. Zhu, Bao Yang, Jia Xie and Liangbing Hu. "Highly Flexible and Efficient Solar Steam Generation Device." Advanced Materials (2017).
14. Wan, Jiayu, Yue Xu, Burak Ozdemir, Lisha Xu, Andrei B. Sushkov, **Zhi Yang**, Bao Yang, Dennis Drew, Veronica Barone, and Liangbing Hu. "Tunable Broadband Nanocarbon Transparent Conductor by Electrochemical Intercalation." ACS nano 11, no. 1 (2017): 788-796.
15. Zhu, Mingwei, Yiju Li, Guang Chen, Feng Jiang, **Zhi Yang**, Xiaoguang Luo, Yanbin Wang, Steven D. Lacey, Jiaqi Dai, Chengwei Wang, Chao Jia, Jiayu Wan, Yonggang Yao, Amy Gong, Bao Yang, Zongfu Yu, Siddhartha Das and Liangbing Hu. "Tree‐Inspired Design for High‐Efficiency Water Extraction." Advanced Materials (2017).
16. Zhu, Mingwei, Yiju Li, Fengjuan Chen, Xueyi Zhu, Jiaqi Dai, Yongfeng Li, **Zhi Yang**, Xuejun Yan, Jianwei Song, Yanbin Wang, Emily Hitz, Wei Luo,

Minhui Lu, Bao Yang and Liangbing Hu. "Plasmonic Wood for High‐Efficiency Solar Steam Generation." Advanced Energy Materials (2017).

17. Liu, Yang, Yun Qiao, Ying Zhang, **Zhi Yang,** Tingting Gao, Dylan Kirsch, Boyang Liu, Jianwei Song, Bao Yang, and Liangbing Hu. "3D Printed Separator for the Thermal Management of High-performance Li Metal Anodes." Energy Storage Materials (2017).

Appendices

Appendix A FLIR Merlin MID Infrared Camera

IR camera is used to capture the radiative thermal energy, which value will be used to evaluate object surface temperature. Thus emissivity of the object surface is the key for accurate temperature readings.

The FLIR Merlin MID IR Camera has a sensor resolution of 320 x 256 pixels, detecting IR radiation at wavelength from 1 to 5.4 um. It is connected to ThermaCAM Research software for control. Cap is needed to cover the lens to prevent possible contamination.

Figure 0-1 Digital Picture of FLIR Merlin MID IR Camera

The following is the computer associated with IR camera with synced communication channels.

Figure 0-2 Digital Picture of Computer Synced With FLIR Merlin MID IR Camera

Once power to the IR camera and computer are connected, go to ThermaCAM software from start menu, choose SR-1 version.

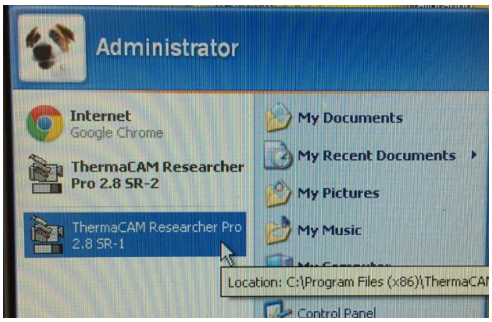

Figure 0-3 Screenshot of ThermaCAM Software Associated With FLIR Merlin MID IR Camera

Open the ThermaCAM software, from the top menu, choose connect. The default camera type is used for connection.

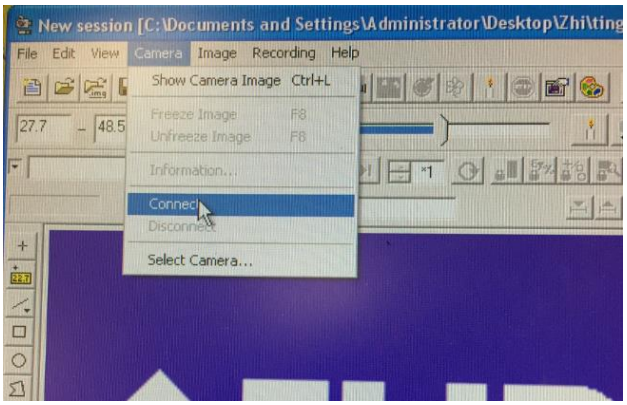

Figure 0-4 Screenshot of ThermaCAM Software Interface

Using the following info during the process without changing IP address. Then IR images should be observed from the computer screen within 5 minutes.

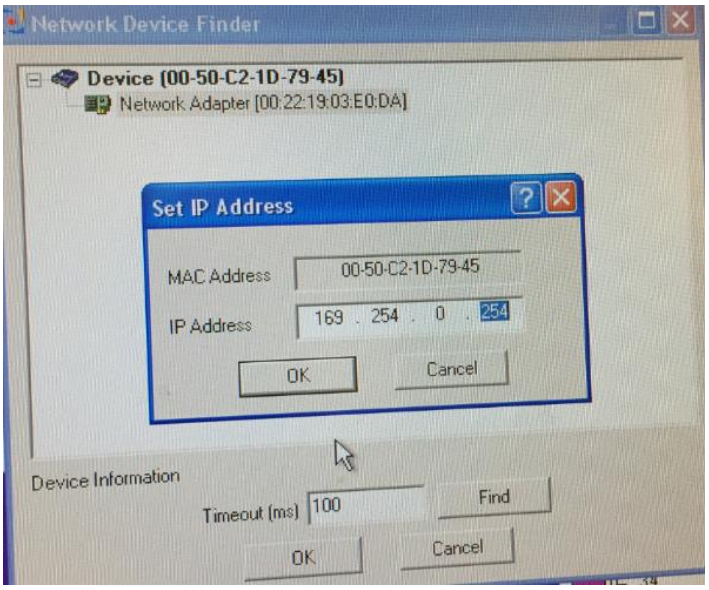

Figure 0-5 Screenshot of ThermaCAM Software IP Address

Once IR camera or post-processing the IR images are controlled using ThermaCAM software, full access will be granted to detect the temp of a point, line and square shape from left tool bar. The detailed info can be accessed from the bottom result tab. Temperature range can be also changed from the top. The candle icon is for

automatically temp ranging. For video recording, simply click start (pistol) and end (flag). And for post-processing, various speed can be applied for replay.

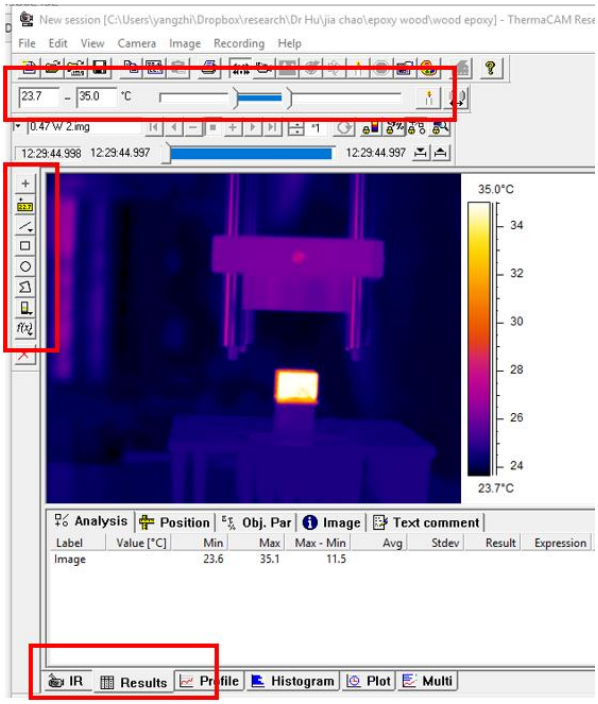

Figure 0-6 Screenshot of ThermaCAM Software Control Interface

The object emissivity value can be adjusted in settings. Also room temp, RH, distance between IR camera and object can be varied according to the actual test condition.

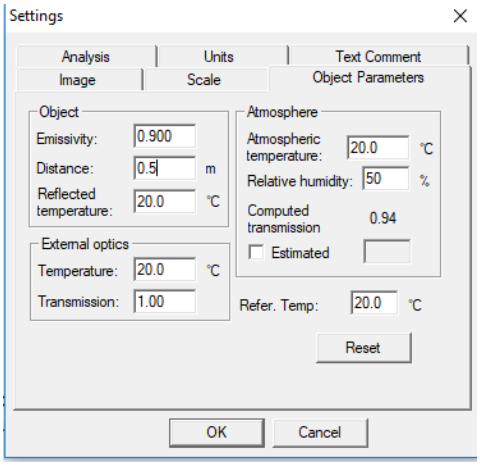

Figure 0-7 Screenshot of ThermaCAM Software Setting Interface

Appendix B Magnetic Field Wire Housing Assembly Design and Construction Process

Design and Construction Process Flow:

1. Specify target magnetic field distribution with desired linearity and homogeneity. Use boundary element method (BEM) to solve wire pattern on cylinder/ slanted-cylinder surface in terms of cylindrical Bessel functions. Generate coordinates for each point of wire pattern.
2. Import wire coordinates into Solidworks and project on target surface, sweep emboss to generate 3D wire pattern. Embedded wire pattern into main body of magnetic field wire housing assembly at desired locations. Subtract the wire pattern using Boolean operation.
3. Design and optimize the cooling channel feature in terms of channel number, channel geometry, channel location and header design. Incorporate optimized cooling channel design to magnetic field housing assembly and subtract the cooling channel bodies.
4. Save the final magnetic wire housing assembly geometry in format of .STL for 3D print process. Choose desired 3D print type, material and print settings. Use relative high fill density for stronger mechanical support.
5. After the 3D print is finished, AWG 12 copper wire can be snapped into the wire pattern grooves. Then a layer of JB weld grey epoxy is applied to secure the position of copper wire. After the epoxy is fully cured, a layer of Line X coating is applied on entire surface of magnetic field wire housing assembly to prevent possible blockage of cooling channels during potting process. A thin

layer of BJB clear epoxy can be applied outside Line X coating as a double safe procedure against potting epoxy penetration to cooling channels.

6. Once X, Y, Z and outer fiberglass are finished, put them together in a "Russian Doll" like pattern. Use perpendicular measurement to ensure the X and Y layer are perpendicular to each other before potting process. Apply silicon paste around the peripheral of inside and outside layer to seal the assembly. Then the entire magnetic field housing assembly is ready for last potting process.
7. 3150-50 FR epoxy from Epoxies.etc is chosen as potting epoxy due to its high temperature resistance, high dielectric constant, low viscosity and high thermal conductivity. The operating temperature range for 3150-50 FR epoxy is from -60 to 200 ºC. During potting process, several sub-steps need to be carried to prevent significant exothermic behavior during epoxy cure process. Potting epoxy needs at least 3 full days to cure.
8. Once the potting epoxy is cured, connect the header to the cooling system.
9. The magnetic field distribution mapping can be performed as well as cooling testing for magnetic field wire housing for each individual layer separately or together at the same time.

Appendix C Thermal Transient Numerical Simulation Steps

In order to perform transient simulation in Thermo-electric module, a command code needs to be inserted in steady state boundary conditions. Geometry, material properties assignment, meshing are exactly the same as steady state simulations (details are not

shown here). The command code window can be inserted by click on C in environment section as shown below.

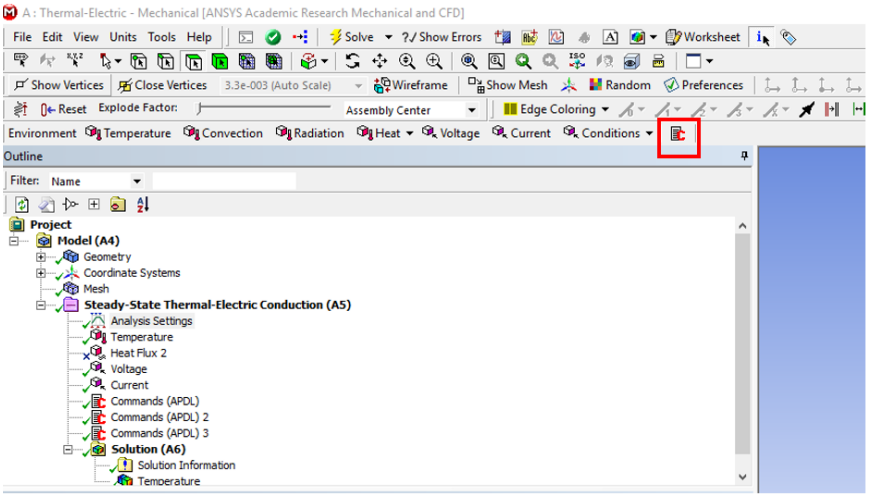

Figure 0-8 Screenshot of APDL Command Window Insertion

Once the command (APDL) is inserted, in commands window, APDL code can be used to activate transient simulations by using the following code:

Antype, 4 (for transient simulation only)

Timint, off (this shuts down any other undesirable time integration)

Timint, on (time integration/ steps is active from this step)

Commands

```
!   Commands inserted into this file will be executed just prior to the ANSYS SOLVE command.
!   These commands may supersede command settings set by Workbench.

!   Active UNIT system in Workbench when this object was created:  Metric (m, kg, N, s, V, A)
!   NOTE:  Any data that requires units (such as mass) is assumed to be in the consistent solver unit system.
!               See Solving Units in the help system for more information.


antype,4
timint, off
timint, on
```

Figure 0-9 Screenshot of APDL Code for Transient Analysis

Note: this inserted APDL in WB varies slightly from the APDL code that can be directly used in APDL module. (Check the ANSYS manual for more details about APDL)

After assign commands code, transient analysis settings can be customized with different number of time steps and each time step end time. For example, if the goal is to have 10 steps covering up to 100s, each step number and its end step time can be set individually. Once that is finished, the time step number and details in the table will show in the graphic window. Try to turn on the auto sub-step. (10 sub-step is recommended, which means for each time step, it will solve at least 10 sub-step for convergence)

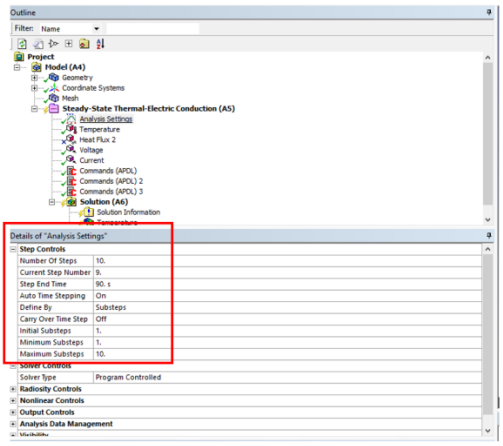

Figure 0-10 Screenshot of Transient Simulation Time Step Setting

Once the time steps are defined, boundary condition to those specifically defined time steps can be assigned with either constant value or varying value. For constant boundary, just put the same value for all time steps. And from the graph, a straight line will be shown for constant boundary condition. Similarly, if the boundary condition are fluctuating or in a cycle, corresponding curve for those conditions can be viewed and checked in the graphic window.

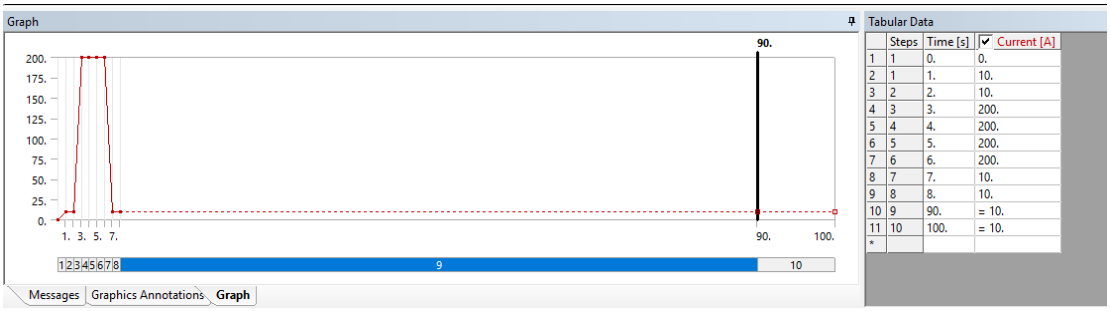

Figure 0-11 Screenshot of Transient Simulation Time-dependent Boundary Conditions

For varying boundary conditions, different parameters for each individual time step can be assigned in table. Again, the graph will be shown next to the table. Any shape of BC can be imported, however, for sharp rectangular BC, the time step needs to be adjusted accordingly.

Figure 0-12 Screenshot of Transient Simulation Time-independent Boundary Conditions

After assign all boundary conditions with desired values for each time step, solve the project and evaluate the result. Based on the input boundary conditions, results will be varied accordingly. Its data will be stored in the table with respect to time.

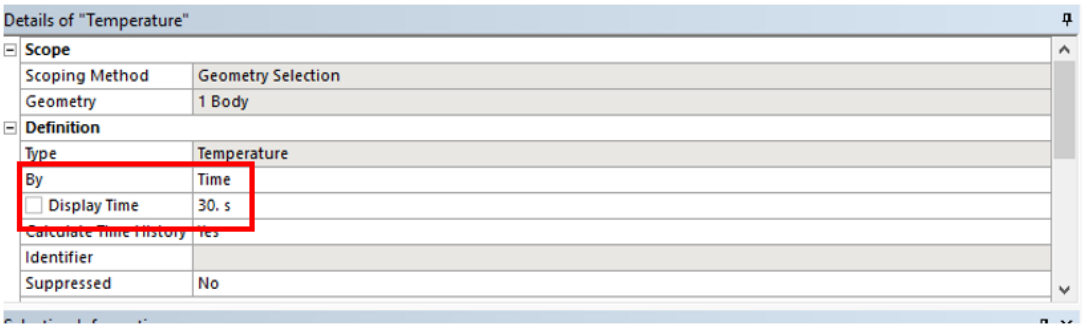

Figure 0-13 Screenshot of Transient Simulation Result at Specific Time Step

To view the result for each individually time step, simply go to the result, change the display time to desired time step and re-evaluate the result. Then the graph will display the result (*e.g.* temperature distribution) at that specific time step.

NOTE: if the final time step is set to a very large number, the final result may be close to steady state results. It can be noticed after certain time, the result becomes almost constant.

Bibliography

[1] E. S. Toberer, L. L. Baranowski, and C. Dames, "Advances in thermal conductivity," *Annual Review of Materials Research*, vol. 42, pp. 179-209, 2012.

[2] A. Bar-Cohen, P. Wang, and E. Rahim, "Thermal management of high heat flux nanoelectronic chips," *Microgravity Science and Technology*, vol. 19, no. 3-4, pp. 48-52, 2007.

[3] "Computerruimte optimaliseren." http://advies-computerruimte.jouwweb.nl/optimaliseren

[4] "Do relaunchable rocket (SpaceX project) has heat shields. If it has, do they use the same materials as space shuttle heat shields?." https://www.quora.com/Do-relaunchable-Rocket-SpaceX-project-has-heat-shields-If-it-has-do-they-use-the-same-materials-as-space-shuttle-heat-shields

[5] D. Chung, "Materials for thermal conduction," *Applied thermal engineering*, vol. 21, no. 16, pp. 1593-1605, 2001.

[6] N. B. Vargaftik, *Handbook of thermal conductivity of liquids and gases*. CRC press, 1993.

[7] A. Sarı and A. Karaipekli, "Preparation, thermal properties and thermal reliability of palmitic acid/expanded graphite composite as form-stable PCM for thermal energy storage," *Solar Energy Materials and Solar Cells*, vol. 93, no. 5, pp. 571-576, 2009.

[8] J. Zeng, L. Sun, F. Xu, Z. Tan, Z. Zhang, J. Zhang, and T. Zhang, "Study of a PCM based energy storage system containing Ag nanoparticles," *Journal of Thermal Analysis and Calorimetry*, vol. 87, no. 2, pp. 371-375, 2006.

[9] M. Biercuk, M. C. Llaguno, M. Radosavljevic, J. Hyun, A. T. Johnson, and J. E. Fischer, "Carbon nanotube composites for thermal management," *Applied physics letters*, vol. 80, no. 15, pp. 2767-2769, 2002.

[10] Y. Cui, C. Liu, S. Hu, and X. Yu, "The experimental exploration of carbon nanofiber and carbon nanotube additives on thermal behavior of phase change materials," *Solar Energy Materials and Solar Cells*, vol. 95, no. 4, pp. 1208-1212, 2011.

[11] F. Yavari, H. R. Fard, K. Pashayi, M. A. Rafiee, A. Zamiri, Z. Yu, R. Ozisik, T. Borca-Tasciuc, and N. Koratkar, "Enhanced thermal conductivity in a nanostructured phase change composite due to low concentration graphene additives," *The Journal of Physical Chemistry C*, vol. 115, no. 17, pp. 8753-8758, 2011.

[12] L. H. Li and Y. Chen, "Atomically Thin Boron Nitride: Unique Properties and Applications," *Advanced Functional Materials*, vol. 26, no. 16, pp. 2594-2608, 2016.

[13] X. Han, Z. Yang, B. Zhao, S. Zhu, L. Zhou, J. Dai, J.-W. Kim, B. Liu, J. W. Connell, T. Li, B. Yang, Y. Lin, and L. Hu, "Compressible, Dense, Three-Dimensional Holey Graphene Monolithic Architecture," *ACS nano*, vol. 11, no. 3, pp. 3189-3197, 2017.

[14] S. K. Das, N. Putra, P. Thiesen, and W. Roetzel, "Temperature dependence of thermal conductivity enhancement for nanofluids," *Journal of heat transfer*, vol. 125, no. 4, pp. 567-574, 2003.
[15] G.-W. Lee, M. Park, J. Kim, J. I. Lee, and H. G. Yoon, "Enhanced thermal conductivity of polymer composites filled with hybrid filler," *Composites Part A: Applied science and manufacturing*, vol. 37, no. 5, pp. 727-734, 2006.
[16] E. S. Lee, S. M. Lee, D. J. Shanefield, and W. R. Cannon, "Enhanced thermal conductivity of polymer matrix composite via high solids loading of aluminum nitride in epoxy resin," *Journal of the American Ceramic Society*, vol. 91, no. 4, pp. 1169-1174, 2008.
[17] A. Yu, P. Ramesh, X. Sun, E. Bekyarova, M. E. Itkis, and R. C. Haddon, "Enhanced thermal conductivity in a hybrid graphite nanoplatelet–carbon nanotube filler for epoxy composites," *Advanced Materials*, vol. 20, no. 24, pp. 4740-4744, 2008.
[18] T.-L. Li and S. L.-C. Hsu, "Enhanced thermal conductivity of polyimide films via a hybrid of micro-and nano-sized boron nitride," *The Journal of Physical Chemistry B*, vol. 114, no. 20, pp. 6825-6829, 2010.
[19] E. Ekimov, N. Suetin, A. Popovich, and V. Ralchenko, "Thermal conductivity of diamond composites sintered under high pressures," *Diamond and related materials*, vol. 17, no. 4, pp. 838-843, 2008.
[20] E. Choi, J. Brooks, D. Eaton, M. Al-Haik, M. Hussaini, H. Garmestani, D. Li, and K. Dahmen, "Enhancement of thermal and electrical properties of carbon nanotube polymer composites by magnetic field processing," *Journal of Applied physics*, vol. 94, no. 9, pp. 6034-6039, 2003.
[21] H. A. Mintsa, G. Roy, C. T. Nguyen, and D. Doucet, "New temperature dependent thermal conductivity data for water-based nanofluids," *International Journal of Thermal Sciences*, vol. 48, no. 2, pp. 363-371, 2009.
[22] M. Yamashita, Y. Senshu, T. Shibauchi, S. Kasahara, K. Hashimoto, D. Watanabe, H. Ikeda, T. Terashima, I. Vekhter, and A. Vorontsov, "Nodal gap structure of superconducting BaFe 2 (As 1− x P x) 2 from angle-resolved thermal conductivity in a magnetic field," *Physical Review B*, vol. 84, no. 6, p. 060507, 2011.
[23] A. Yiannou, "Nanofluid thermal conductivity," University of Pretoria, 2015.
[24] B. Wright, D. Thomas, H. Hong, L. Groven, J. Puszynski, E. Duke, X. Ye, and S. Jin, "Magnetic field enhanced thermal conductivity in heat transfer nanofluids containing Ni coated single wall carbon nanotubes," *Applied Physics Letters*, vol. 91, no. 17, p. 173116, 2007.
[25] A. F. Mills, *Basic heat and mass transfer*. Pearson College Div, 1999.
[26] J. M. Ziman, *Principles of the Theory of Solids*. Cambridge university press, 1972.
[27] R. A. Lemdiasov and R. Ludwig, "A stream function method for gradient coil design," *Concepts in Magnetic Resonance Part B: Magnetic Resonance Engineering*, vol. 26, no. 1, pp. 67-80, 2005.
[28] B. Chronik, A. Alejski, and B. K. Rutt, "Design and fabriacation of a three-axis multilayer gradient coil for magnetic resonance microscopy of mice," *Magnetic*

Resonance Materials in Physics, Biology and Medicine, vol. 10, no. 2, pp. 131-146, 2000.

[29] K. C. Goodrich, J. R. Hadley, S. M. Moon, B. A. Chronik, T. J. Scholl, J. T. Debever, and D. L. Parker, "Design, fabrication, and testing of an insertable double‐imaging‐region gradient coil," *Concepts in Magnetic Resonance Part B: Magnetic Resonance Engineering*, vol. 35, no. 2, pp. 98-105, 2009.

[30] D. Zhao, X. Qian, X. Gu, S. A. Jajja, and R. Yang, "Measurement Techniques for Thermal Conductivity and Interfacial Thermal Conductance of Bulk and Thin Film Materials," *arXiv preprint arXiv:1605.08469*, 2016.

[31] S. Alvarado, E. Marín, A. Juárez, A. Calderón, and R. Ivanov, "A hot-wire method based thermal conductivity measurement apparatus for teaching purposes," *European Journal of Physics*, vol. 33, no. 4, p. 897, 2012.

[32] M. Azadbakht, M. H. Khoshtaghaza, B. Ghobadian, and S. Minaei, "Thermal properties of soybean pod as a function of moisture content and temperature," *American journal of food science and technology*, vol. 1, no. 2, pp. 9-13, 2013.

[33] M. A. Presley and P. R. Christensen, "Thermal conductivity measurements of particulate materials 1. A review," *Journal of Geophysical Research: Planets*, vol. 102, no. E3, pp. 6535-6549, 1997.

[34] X. C. Tong, *Advanced materials for thermal management of electronic packaging*. Springer Science & Business Media, 2011.

[35] D. G. Cahill, "Thermal conductivity measurement from 30 to 750 K: the 3ω method," *Review of scientific instruments*, vol. 61, no. 2, pp. 802-808, 1990.

[36] G. Gesele, J. Linsmeier, V. Drach, J. Fricke, and R. Arens-Fischer, "Temperature-dependent thermal conductivity of porous silicon," *Journal of Physics D: Applied Physics*, vol. 30, no. 21, p. 2911, 1997.

[37] X. J. Hu, A. A. Padilla, J. Xu, T. S. Fisher, and K. E. Goodson, "3-omega measurements of vertically oriented carbon nanotubes on silicon," *Journal of Heat Transfer*, vol. 128, no. 11, pp. 1109-1113, 2006.

[38] D. G. Cahill and R. O. Pohl, "Thermal conductivity of amorphous solids above the plateau," *Physical review B*, vol. 35, no. 8, p. 4067, 1987.

[39] H. Zhu, Y. Li, Z. Fang, J. Xu, F. Cao, J. Wan, C. Preston, B. Yang, and L. Hu, "Highly thermally conductive papers with percolative layered boron nitride nanosheets," *ACS nano*, vol. 8, no. 4, pp. 3606-3613, 2014.

[40] "CaF2 characteristics & transmission curve." http://www.bbotech.com/product.php?cid=149

[41] "KBr protected humidity coating." http://www.ispoptics.com/admuploads/file/prh_kbr_0.5-20.pdf

[42] A. Bar-Cohen and P. Wang, "Thermal management of on-chip hot spot," *Journal of Heat Transfer*, vol. 134, no. 5, p. 051017, 2012.

[43] H. F. Hamann, A. Weger, J. A. Lacey, Z. Hu, P. Bose, E. Cohen, and J. Wakil, "Hotspot-limited microprocessors: Direct temperature and power distribution measurements," *IEEE Journal of Solid-State Circuits*, vol. 42, no. 1, pp. 56-65, 2007.

[44] D. Golberg, Y. Bando, Y. Huang, T. Terao, M. Mitome, C. Tang, and C. Zhi, "Boron nitride nanotubes and nanosheets," *ACS nano*, vol. 4, no. 6, pp. 2979-2993, 2010.
[45] K. Watanabe, T. Taniguchi, and H. Kanda, "Direct-bandgap properties and evidence for ultraviolet lasing of hexagonal boron nitride single crystal," *Nature materials*, vol. 3, no. 6, pp. 404-409, 2004.
[46] L. H. Li, E. J. Santos, T. Xing, E. Cappelluti, R. Roldán, Y. Chen, K. Watanabe, and T. Taniguchi, "Dielectric screening in atomically thin boron nitride nanosheets," *Nano letters*, vol. 15, no. 1, pp. 218-223, 2014.
[47] J. Wu, B. Wang, Y. Wei, R. Yang, and M. Dresselhaus, "Mechanics and Mechanically Tunable Band Gap in Single-Layer Hexagonal Boron-Nitride," *Materials Research Letters*, vol. 1, no. 4, pp. 200-206, 2013.
[48] S. Majety, X. Cao, R. Dahal, B. Pantha, J. Li, J. Lin, and H. Jiang, "Semiconducting hexagonal boron nitride for deep ultraviolet photonics," in *Proc. SPIE*, 2012, vol. 8268, p. 82682R.
[49] Z. Yang, L. Zhou, W. Luo, J. Wan, J. Dai, X. Han, K. Fu, D. Henderson, B. Yang, and L. Hu, "Thermally conductive, dielectric PCM–boron nitride nanosheet composites for efficient electronic system thermal management," *Nanoscale*, vol. 8, no. 46, pp. 19326-19333, 2016.
[50] "Tesla Model S fires under NHTSA investigation." https://www.autoevolution.com/news/tesla-model-s-fires-under-nhtsa-investigation-71375.html
[51] L. Zhou, Z. Yang, W. Luo, X. Han, S.-H. Jang, J. Dai, B. Yang, and L. Hu, "Thermally Conductive, Electrical Insulating, Optically Transparent Bi-Layer Nanopaper," *ACS Applied Materials & Interfaces*, vol. 8, no. 42, pp. 28838-28843, 2016.
[52] W. Lee, H. Koo, J. Sun, J. Noh, K.-S. Kwon, C. Yeom, Y. Choi, K. Chen, A. Javey, and G. Cho, "A fully roll-to-roll gravure-printed carbon nanotube-based active matrix for multi-touch sensors," *Scientific reports*, vol. 5, 2015.
[53] R. P. Patel and C. A. Wolden, "Defect analysis and mechanical performance of plasma-deposited thin films on flexible polycarbonate substrates," *Applied Surface Science*, vol. 268, pp. 416-424, 2013.
[54] S.-K. Kim, T. Liu, and X. Wang, "Flexible, Highly Durable, and Thermally Stable SWCNT/Polyimide Transparent Electrodes," *ACS applied materials & interfaces*, vol. 7, no. 37, pp. 20865-20874, 2015.
[55] J. Huang, H. Zhu, Y. Chen, C. Preston, K. Rohrbach, J. Cumings, and L. Hu, "Highly transparent and flexible nanopaper transistors," *Acs Nano*, vol. 7, no. 3, pp. 2106-2113, 2013.
[56] Y. Zhou, C. Fuentes-Hernandez, T. M. Khan, J.-C. Liu, J. Hsu, J. W. Shim, A. Dindar, J. P. Youngblood, R. J. Moon, and B. Kippelen, "Recyclable organic solar cells on cellulose nanocrystal substrates," *Scientific reports*, vol. 3, p. 1536, 2013.
[57] H. Tetsuka, A. Nagoya, and R. Asahi, "Highly luminescent flexible amino-functionalized graphene quantum dots@ cellulose nanofiber–clay hybrids for

white-light emitting diodes," *Journal of Materials Chemistry C,* vol. 3, no. 15, pp. 3536-3541, 2015.

[58] "The rise of the smartwatch. Ticking clock for Swiss watchmakers." http://techadvisor.lk/2016/03/02/the-rise-of-the-smartwatch-ticking-clock-for-swiss-watchmakers/

[59] X. Han, Y. Chen, H. Zhu, C. Preston, J. Wan, Z. Fang, and L. Hu, "Scalable, printable, surfactant-free graphene ink directly from graphite," *Nanotechnology,* vol. 24, no. 20, p. 205304, 2013.

[60] W. Luo, L. Zhou, K. Fu, Z. Yang, J. Wan, M. Manno, Y. Yao, H. Zhu, B. Yang, and L. Hu, "A thermally conductive separator for stable Li metal anodes," *Nano letters,* vol. 15, no. 9, pp. 6149-6154, 2015.

[61] F. Ding, W. Xu, G. L. Graff, J. Zhang, M. L. Sushko, X. Chen, Y. Shao, M. H. Engelhard, Z. Nie, and J. Xiao, "Dendrite-free lithium deposition via self-healing electrostatic shield mechanism," *Journal of the American Chemical Society,* vol. 135, no. 11, pp. 4450-4456, 2013.

[62] Y. Zhang, J. Qian, W. Xu, S. M. Russell, X. Chen, E. Nasybulin, P. Bhattacharya, M. H. Engelhard, D. Mei, and R. Cao, "Dendrite-free lithium deposition with self-aligned nanorod structure," *Nano letters,* vol. 14, no. 12, pp. 6889-6896, 2014.

[63] Y. Wang, L. Xu, Z. Yang, H. Xie, P. Jiang, J. Dai, W. Luo, Y. Yao, E. Hitz, and R. Yang, "High Temperature Thermal Management with Boron Nitride Nanosheets," *Nanoscale,* 2017.

[64] S. Wolf, D. Awschalom, R. Buhrman, J. Daughton, S. Von Molnar, M. Roukes, A. Y. Chtchelkanova, and D. Treger, "Spintronics: a spin-based electronics vision for the future," *Science,* vol. 294, no. 5546, pp. 1488-1495, 2001.

[65] S. Uji, H. Shinagawa, T. Terashima, T. Yakabe, Y. Terai, M. Tokumoto, A. Kobayashi, H. Tanaka, and H. Kobayashi, "Magnetic-field-induced superconductivity in a two-dimensional organic conductor," *Nature,* vol. 410, no. 6831, pp. 908-910, 2001.

[66] J.-B. Mathieu, G. Beaudoin, and S. Martel, "Method of propulsion of a ferromagnetic core in the cardiovascular system through magnetic gradients generated by an MRI system," *IEEE Transactions on Biomedical Engineering,* vol. 53, no. 2, pp. 292-299, 2006.

[67] T. Campi, S. Cruciani, and M. Feliziani, "Magnetic shielding of wireless power transfer systems," in *Electromagnetic Compatibility, Tokyo (EMC'14/Tokyo), 2014 International Symposium on*, 2014, pp. 422-425: IEEE.

[68] W. B. Handler, C. T. Harris, T. J. Scholl, D. L. Parker, K. C. Goodrich, B. Dalrymple, F. Sass, and B. A. Chronik, "New head gradient coil design and construction techniques," *Journal of Magnetic Resonance Imaging,* vol. 39, no. 5, pp. 1088-1095, 2014.

[69] P. T. While, L. K. Forbes, and S. Crozier, "3D gradient coil design for open MRI systems," *Journal of Magnetic Resonance,* vol. 207, no. 1, pp. 124-133, 2010.

[70] T. Vaughan, L. DelaBarre, C. Snyder, J. Tian, C. Akgun, D. Shrivastava, W. Liu, C. Olson, G. Adriany, and J. Strupp, "9.4 T human MRI: preliminary results," *Magnetic resonance in medicine,* vol. 56, no. 6, pp. 1274-1282, 2006.
[71] K. Kusagaya, H. Hagino, S. Tanaka, K. Miyazaki, and M. Takashiri, "Structural and thermoelectric properties of nanocrystalline bismuth telluride thin films under compressive and tensile strain," *Journal of Electronic Materials,* vol. 44, no. 6, pp. 1632-1636, 2015.
[72] J. Grunlan, C. Yu, C. Cho, and G. Moriarty, "Completely Organic Carbon Nanostructured Thermoelectric Thin Films with Power Factors Exceeding Bismuth Telluride," in *Meeting Abstracts*, 2016, no. 6, pp. 561-561: The Electrochemical Society.
[73] P. H. Le, C.-N. Liao, C. W. Luo, and J. Leu, "Thermoelectric properties of nanostructured bismuth–telluride thin films grown using pulsed laser deposition," *Journal of Alloys and Compounds,* vol. 615, pp. 546-552, 2014.
[74] M. Wu, S. A. Ramírez, E. Shafahian, L. Guo, C. Glorieux, K. Binnemans, and J. Fransaer, "Electrodeposition of bismuth telluride thin films containing silica nanoparticles for thermoelectric applications," *Electrochimica Acta,* vol. 253, pp. 554-562, 2017.
[75] Z.-k. Cai, P. Fan, Z.-h. Zheng, P.-j. Liu, T.-b. Chen, X.-m. Cai, J.-t. Luo, G.-x. Liang, and D.-p. Zhang, "Thermoelectric properties and micro-structure characteristics of annealed N-type bismuth telluride thin film," *Applied Surface Science,* vol. 280, pp. 225-228, 2013.
[76] Y. Zhou, L. Li, Q. Tan, and J.-F. Li, "Thermoelectric properties of Pb-doped bismuth telluride thin films deposited by magnetron sputtering," *Journal of Alloys and Compounds,* vol. 590, pp. 362-367, 2014.
[77] J. Nickel, *Magnetoresistance overview*. Hewlett-Packard Laboratories, Technical Publications Department, 1995.
[78] R. L. White, "Giant magnetoresistance materials and their potential as read head sensors," *IEEE transactions on magnetics,* vol. 30, no. 2, pp. 346-352, 1994.